The Pennsylvania State University

The Graduate School

College of Earth and Mineral Sciences

EXPERIMENTAL CHARACTERIZATION AND MODELING OF MULTIAXIAL PLASTICITY BEHAVIOR OF AUSTENITIC STAINLESS STEEL 304L PRODUCED BY ADDITIVE MANUFACTURING

A Dissertation in

Materials Science and Engineering

by

Zhuqing Wang

Submitted in Partial Fulfillment

of the Requirements

for the Degree of

Doctor of Philosophy

May 2018

The dissertation of Zhuqing Wang was reviewed and approved * by the following:

Allison M. Beese

Assistant Professor of Materials Science and Engineering

Dissertation Advisor

Chair of Committee

Tarasankar DebRoy

Professor of Materials Science and Engineering

Hojong Kim

Assistant Professor of Materials Science and Engineering

Robert C. Voigt

Professor of Industrial and Manufacturing Engineering

Suzanne E. Mohney

Professor of Materials Science and Engineering

Chair of the Intercollege Graduate Degree Program in Materials Science and Engineering

*Signatures are on file in the Graduate School.

Abstract

In additive manufacturing of metallic alloys, near-net shape 3D components are built in a layer-by-layer fashion. Austenitic stainless steels have high strength and ductility, as they tend to undergo a strain-induced martensitic phase transformation with plastic deformation. The thesis focuses on quantifying process-microstructure-multiaxial mechanical property relationships in additively manufactured 304L austenitic stainless steel (SS304L) and developing a physically-based plasticity model for this material that relates microstructural phase transformation to macroscopic mechanical properties.

The effect of processing parameters on microstructure and mechanical properties was studied using pure SS304L walls. A grain growth model was used to describe austenite grain size as a function of processing parameters and location. A Hall-Petch relationship was used to explain the effect of austenite grain size and morphology on yield strength.

The effects of chemistry, stress state, and texture on martensitic phase transformation were investigated using walls made using a mixture of SS304L powder and iron powder. As the concentration of elements that increase the stacking fault energy of austenite decreased, the austenite stability decreased, and the propensity for martensitic transformation increased.

Multiaxial mechanical tests, including uniaxial tension, uniaxial compression, pure shear, and combined tension and shear, were performed on the material. As the primary texture resulted in a higher driving force for martensitic transformation under uniaxial compression than uniaxial tension, the rate of phase transformation was higher under uniaxial compression, which contradicted the trend in texture-free materials.

A macroscopic plasticity model is proposed to describe the multiaxial plasticity behavior for the material. This model makes use of a chemistry-, stress state-, and texture-dependent martensitic transformation kinetics equation to incorporate the effect of martensitic transformation on mechanical properties. The plasticity model was implemented into a finite element code, and calibrated and validated using experimental data. The good agreement between simulation and experimental results under the stress states studied indicates the model is able to describe and predict the multiaxial mechanical behavior of additively manufactured SS304L. The results in this thesis work enable the use of additively manufactured stainless steels in structural applications, as it provides quantitative links among processing, structure, and mechanical behavior.

Table of Contents

List of Figures

List of Tables

Acknowledgments

First, I would like to express my sincere thanks to my advisor, Professor Allison Beese, for her consistent guidance, encouragement, and support for my Ph.D. research and future career. She has taught me how to be a good scientist, advisor, and mentor, and made my graduate school meaningful and rewarding.

Besides my advisor, I would like to thank the rest of my committee, Professors Tarasankar DebRoy, Hojong Kim, and Robert Voigt, for their insightful comments on my research.

My sincere thanks also go to Dr. Dong Ma, Dr. Alexandru Stoica, and Mr. Matthew Frost of Oak Ridge National Lab for technical support and helpful discussions.

I would like to thank my labmates, Lourdes Bobbio, Shipin Qin, and Alexander Wilson-Heid. My research would not have been possibly done without their assistance and encouragement.

I am grateful for the financial support provided by the National Science Foundation that allowed me to pursue my Ph.D.

Most importantly, I would like to thank my family and friends for their invaluable support and love, especially my father Feng Wang, my mother Lingkun Zhang, and my husband Weinan Chen.

Chapter 1

Introduction

In additive manufacturing (AM) of metallic alloys, 3D near-net shape parts are fabricated layer-by-layer through a repetitive process of the delivery of powder or wire feedstock to a 2D layer, the melting of feedstock by a heat source (e.g. a laser, electron beam, or electric arc [1]), the solidification of the molten material, and the fusion of the deposited material to the substrate or previously deposited layers [2]. During AM, each layer experiences rapid heating and cooling thermal cycles, resulting in location- and direction-dependent microstructure and mechanical properties [3–5], which differ from those in conventionally processed counterparts. AM has many advantages over conventional manufacturing, including fabricating custom-designed products, producing complex shaped components, and reducing the waste of raw materials [6,7]. AM has been used to fabricate various metallic alloy systems, including Ti-6Al-4V [8–16], stainless steels [4,17–26], aluminum alloys [27–31], cobalt-chromium alloys [32,33], and nickel-base alloy [34–44].

Transformation Induced Plasticity (TRIP) steels have high strength and ductility, as they may experience a strain-induced austenite-to-martensite phase transformation when they are plastically deformed, or the applied the stress is above the yield strength. The irreversible strain-induced phase transformation contributes to macroscopic strain hardening and microscopic volume expansion [45–55]. The primary material in this work is AISI type 304L austenitic stainless steel (SS304L), which belongs to the family of TRIP steels. Due to the good mechanical properties and corrosion resistance, SS304L has been widely used in petroleum, marine, and chemical industries [22,56].

When additively manufactured SS304L components with complex shapes are used in structural applications, or anything that is load-bearing, the stress level and stress state vary as a function of location. However, to the author's knowledge, only mechanical behavior under uniaxial tension and uniaxial compression of additively manufactured stainless steels have been reported [17,19,57–61], which is insufficient to describe and predict the performance of the components subjected to multiaxial stress states. This work will provide guidance to design and use additively manufactured SS304L under multiaxial loading states in structural applications, and study multiaxial plasticity behavior of additively manufactured steels with retained austenite.

1.1. Additive manufacturing

This thesis focuses on laser-based and powder-based AM techniques, which have two classes: directed energy deposition (DED) and powder bed fusion (PBF), as defined by ISO/ASTM 52900 [62].

1.1.1. Directed energy deposition

In laser-based and powder-based DED, as shown schematically in Figure 1.1, powder feedstock is carried by a shielding gas, such as argon, and fed by nozzles into the melt pool, which is created by a laser beam [2,6,63]. After the completion of one layer, the laser beam moves up to deposit subsequent layers. This process is widely used to fabricate large components and functionally gradient alloys, and repair worn or damaged surfaces [3,64].

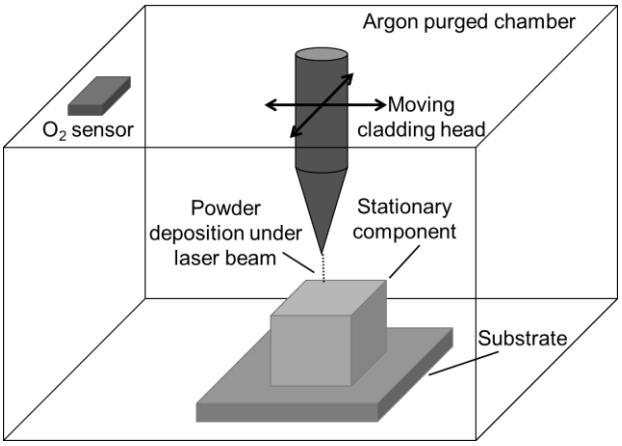

Figure 1.1. Schematic of the directed energy deposition process. Figure from [11].

1.1.2. Powder bed fusion

In laser-based and powder-based PBF, as shown schematically in Figure 1.2, a thin layer of powder is spread on a bed and selectively melted by a laser beam. Once one layer is completed, the bed is lowered and another new layer of powder is added. The process is repeated and the final component, surrounded by the unmelted powder, is thus removed from the bed [3,11]. The components made by PBF have good surface finish and accurate dimensions [3].

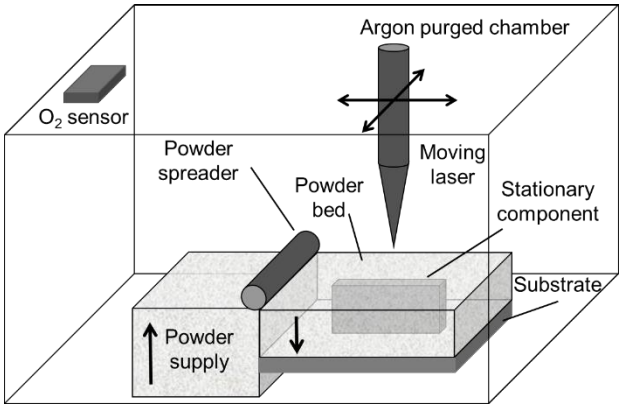

Figure 1.2. Schematic of the powder bed fusion process. Figure from [11].

1.2. Martensitic phase transformation

In additively manufactured SS304L, not all δ-ferrite transforms to austenite during rapid solidification, which leads to residual columnar δ-ferrite dendrites in the austenite matrix [65].

The propensity for strain-induced martensitic transformation is influenced by the stacking fault energy (SFE) of austenite [66]. In face-centered cubic (fcc) austenite, the stacking sequence of {111} planes are changed from ABCABC to ABABAB by a stacking fault, resulting in the formation of a thin layer of hexagonal close-packed (hcp) phase. The hcp ε martensite nucleates at the overlapped stacking faults and serves as nucleation sites for body-centered cubic (bcc) strain-induced α' martensite [47,49,66,67]. Austenite-to-martensite phase transformation also occurs when the applied stress is below the yield strength, which is referred to as stress-assisted martensitic phase transformation. This phase transformation is reversible and responsible for the shape memory effect [47,68].

At a given plastic strain, martensitic transformation rate is affected by several factors, including chemical composition, temperature, strain, strain rate, stress state, texture, and austenite grain size [46,48,49,66]. As the extent of martensitic transformation influences the mechanical properties of the materials, it is important to understand the effect of each factor on martensitic transformation.

1.2.1. Effect of chemical composition

The chemical composition affects the SFE of austenite, which in turn influences the tendency for martensitic transformation. Due to the low SFE of austenitic stainless steels, wide stacking faults are often observed [66]. By adding alloying elements, the SFE of

austenite increases and the width of stacking faults decreases, which results in a decrease in the number of nucleation sites for martensite and an increase in austenite stability. A review on the effect of chemistry on martensitic transformation in conventionally processed and additively manufactured stainless steels is given in Chapter 4.

The effect of chemical composition on martensitic transformation kinetics has been described in terms of chemistry dependent strain-induced martensite start temperature, M_s^σ, and martensite finish temperature, M_d, as schematically shown in Figure 1.3 [47]. When deformed above M_d, austenite is stable and plastically deformed with no subsequent phase transformation to martensite. Only deformed between M_s^σ and M_d, metastable austenite might transform to martensite. As the M_d temperature is difficult to measure experimentally, Angel [46] proposed an M_{d30} temperature, which is the temperature when 50 vol.% of austenite transforms to martensite at a 30% true strain, and is expressed as:

$$M_{d30}(°C) = 413 - 462\,(C + N) - 9.2\,Si - 8.1\,Mn - 13.7\,Cr - 9.5\,Ni - 18.5\,Mo \quad (1.1)$$

where the weight percentage of each element is used for calculation. The M_{d30} temperature is often used as a pseudo-upper bound to determine the presence or absence of martensitic phase transformation.

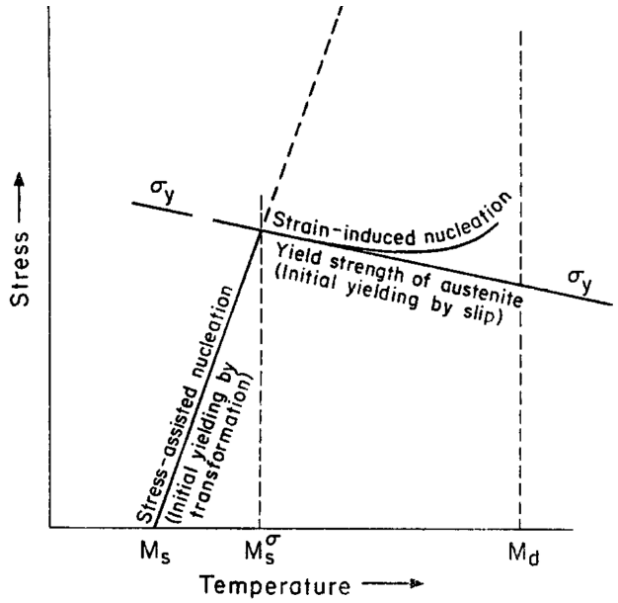

Figure 1.3. Stress as a function of temperature in Fe-Ni-C alloys, schematically showing strain-induced martensitic phase transformation occurs within the range of M_s^σ and M_d temperatures. Figure from [47].

1.2.2. Effect of temperature

Strain-induced martensitic transformation only occurs between M_s^σ and M_d temperatures. As the deformation temperature increases, the chemical driving force for martensitic transformation decreases, and the propensity for phase transformation decreases [46,69,70]. Angel [46] studied martensitic transformation kinetics in 18/8 type austenitic stainless steel under uniaxial tension at various deformation temperatures from -188 ^{o}C to 80 ^{o}C, and found the rate of martensitic transformation with respect to plastic strain and the saturation value of martensite volume fraction increased as the temperature decreased. Powell et al. [69] investigated the effect of temperature ranging from 10 K to 293 K on martensitic transformation in 301 and 304 stainless steels, and found the phase transformation was suppressed as the temperature increased. Iwamoto et al. [70] carried

out uniaxial tension and compression tests on 304 stainless steel from 128 K to 353 K, and their results showed that the rate of martensitic transformation with respect to plastic strain and saturation value of martensite content increased as the temperature decreased under both stress states.

1.2.3. Effect of strain rate

The strain rate affects martensitic phase transformation by affecting the temperature. Most studies have shown that at a high strain rate, adiabatic heating from plastic deformation increases the temperature and austenite stability, and suppresses the phase transformation [71–77].

Staudhammer et al. [75], Hecker et al. [72], and Murr et al. [73] investigated the effect of strain rate on martensitic phase transformation at strain rates from 10^{-3} s^{-1} to 10^{3} s^{-1} in 304 stainless steel subjected to uniaxial tension. They observed that when the true strain was below 0.25, strain-induced α' martensite content was larger in specimens loaded at a higher strain rate than that at a lower strain rate. When the applied strain was above 0.25, α' martensite content was lower at a higher strain rate due to the adiabatic heating.

Talonen et al. [74] performed uniaxial tension tests on 301LN and 304 stainless steels at strain rates between 3×10^{-4} s^{-1} and 200 s^{-1}, and found the martensitic transformation rate and the saturation value of martensitic content decreased as the strain rate increased.

1.2.4. Effect of stress state

The effect of stress state on martensitic transformation kinetics has been studied extensively in conventionally processed steels, but the experimental results are contradictory [50]. In addition, there is a lack of study on investigating martensitic transformation kinetics under multiaxial stress states in additively manufactured steels. A review of current literature on the effect of stress state on martensitic transformation kinetics in conventionally processed steels, and our results in additively manufactured SS304L are described in Chapter 5.

1.2.5. Effect of texture

Additively manufactured components are textured, as columnar austenite grains are preferably oriented along the build direction [44,78]. Texture has a large impact on strain-induced martensitic transformation, as the austenite orientation with respect applied stress state influences the driving force for phase transformation [79–82]. A review of current literature on the effect of texture on martensitic transformation kinetics in conventionally processed steels are discussed in Chapter 5.

1.2.6. Effect of austenite grain size

Many investigations have indicated that as austenite grain size increases, the austenite stability decreases, which promote martensitic phase transformation [83–85]. Nohara et al. [83] investigated the effect of grain size on martensitic transformation in Fe-Ni-Cr stainless steels. Their results showed with a decrease in austenite grain size, the martensite content

decreased, and they modified Eqn. (1.1) by incorporating the effect of grain size, as shown in Eqn. (1.2):

$$M_{d30}\ (^{o}C) = 551 - 462\ (C + N) - 9.2\ Si - 8.1\ Mn - 13.7\ Cr - 29\ (Ni + Cu) - 18.5\ Mo - 68\ Nb - 1.42\ (GS - 8) \quad (1.2)$$

where *GS* is the ASTM grain size number [86]. Varma et al. [84] also found the amount of martensite was higher in 304 and 316 stainless steels with larger grains than that in the same materials with smaller grains when subjected to uniaxial tension and cold rolling. However, Shrinivas et al. [87] found martensite content increased as the grain size decreased in 304 stainless steel, and martensitic transformation was not affected by the grain size in 316 stainless steel.

In this thesis, all the mechanical tests were performed at room temperature at quasi-static strain rates. In addition, the grain size in the materials studied varied from 5.5 to 6.5 in ASTM grain size number [2,86], which had little influence on the M_{d30} temperature and austenite stability. Therefore, the effects of strain rate, temperature, and grain size on martensitic phase transformation are not discussed in this thesis.

1.3. Thesis outline

The objective of this thesis is to quantify process-microstructure-multiaxial mechanical property relationships in 304L stainless steel fabricated by laser-based and powder-based directed energy deposition additive manufacturing. A physically-based plasticity model coupled with martensitic transformation kinetics equation is developed to link microstructural phase evolution to multiaxial plasticity behavior of the material on the macroscale.

The thesis is arranged as the following chapters:

In Chapter 2, the SS304L components made by DED AM is discussed. The processing parameters used during fabrication, and the chemical compositions of the materials are introduced.

In Chapter 3, the effect of processing parameters, described as linear heat input, on microstructure and uniaxial tensile mechanical properties of additively manufactured SS304L is discussed. A grain growth model was applied to describe austenite grain size as a function of linear heat input and location. A Hall-Petch relation was used to quantitatively link austenite grain size and morphology to yield strength. The high nitrogen content in additively manufactured SS304L stabilized austenite and impeded strain-induced martensitic phase transformation

In Chapter 4, the effect of chemistry on strain-induced martensitic transformation in additively manufactured SS304L is investigated. Using a mixture of pre-alloyed SS304L powder with iron powder, austenite stability decreased and martensitic transformation increased, which promoted ultimate tensile strength and ductility. The elements that increase the SFE of austenite were preferentially evaporated from the melt pool, resulting in location-dependent martensitic transformation. A chemistry-dependent transformation kinetics equation was proposed for additively manufactured steels experiencing martensitic transformation.

In Chapter 5, the effect of stress state on strain-induced martensitic transformation kinetics in additively manufactured SS304L with texture is studied. The martensitic phase transformation rate in textured SS304L was higher under uniaxial compression than uniaxial tension, contradictory to the trend in texture-free conventionally processed

stainless steels, as the initial texture in additively manufactured SS304L facilitated phase transformation under uniaxial compression. A stress state- and texture-dependent transformation kinetics equation was presented for additively manufactured SS304L.

In Chapter 6, a physically-based plasticity model is proposed for additively manufactured SS304L, in which microscopic martensitic transformation is linked to macroscopic mechanical behavior. The stress state-, texture-, and chemistry-dependent martensitic transformation kinetics equation was incorporated into the isotropic hardening law to describe the effect of phase evolution on mechanical properties. The predicted stress-strain curves from the model agreed well with the experimental results for all the stress states studied.

In Chapter 7, a summary and conclusions of the thesis are presented, as well as suggestions for the direction of future research.

Chapter 2

Material description

Four SS304L components were fabricated using a custom-designed DED system at the Applied Research Lab at Penn State University, as shown schematically in Figure 1.1. In order to isolate the effect of chemistry on martensitic phase transformation and resulting mechanical properties, three walls were fabricated using similar processing parameters but different initial powder compositions by varying the volume fractions of pre-alloyed SS304L powder and iron power. The pre-alloyed SS304L powder was made using nitrogen gas atomization (Carpenter Powder Products, Corp.) with elemental composition shown in Table 2.1. The iron powder was made using hydrogen reduction (Atlantic Equipment Engineers) with a purity of 99.8%. The SS304L powder and iron powder had a sieve size of +325/-100, corresponding to a powder size distribution in the range of 45 µm to 145 µm. The first wall was deposited from 100 vol.% SS304L powder, the second wall from 90 vol.% SS304L powder and 10 vol.% iron powder, and the third wall from 80% vol.% SS304L powder and 20 vol.% iron powder. The final components are referred to as 100%, 90%, and 80% SS304L walls, respectively. The 100% SS304L wall was 110 mm long x 70 mm tall x 11 mm thick, while the 90% and 80% SS304L walls were 140 mm long x 104 mm tall x 14 mm thick.

In order to isolate the effect of processing parameters, a fourth wall was fabricated from 100 vol.% SS304L powder with the same dimension, but different processing parameters, compared to the first wall. The processing parameters and powder compositions of each wall are given in Table 2.2. The energy input is described by the linear heat input, which is the ratio of laser power to scanning speed. All the walls were deposited on

conventionally processed annealed 304L stainless steel substrates (ASTM A479 standard [88]).

During deposition, the chamber was purged using ultra-high purity argon gas to eliminate oxygen contamination. The oxygen level was kept between 60 ppm to 110 ppm, measured by an oxygen analyzer (General Electric CGA 351 Zirconium Oxide Oxygen Analyzer). An ytterbium fiber laser (IPG Photonics® YLR-12000-L) working at a wavelength from 1070 nm to 1080 nm was delivered by a fiber with 600 μm in diameter from an optics system, which consisted of a 125 mm focal length collimator and a 600 mm focal length focusing optics. The powder was delivered through a feeder (Mark XV Precision Powder Feeder) to a custom-designed system equipped with four nozzles. The nozzles were about 10 mm above the substrates and deposited layers, which was the defocused position of the laser beam with a 4 mm spot diameter. The beam was characterized by a beam monitor (PRIMES® Focus Monitor) and followed a Gaussian energy distribution.

The elemental compositions of deposited components and the substrate were characterized (Element Materials Technology, Newtown, PA) with results given in Table 2.1. Inert gas fusion was used to measure nitrogen content, and combustion testing was used to measure carbon and sulfur contents, adhering to ASTM E1019 [89]. Optical emission spectrometry was used to measure the weight fractions of the remaining elements, adhering to ASTM E1086 [90].

Table 2.1. Elemental composition (wt.%) of different locations from the 100%, 90%, and 80% SS304L walls and the conventionally processed SS304L substrate, as well as the computed M_{d30} temperatures, adopted from [126].

	Distance from the substrate (mm)	**C**	**N**	**Si**	**Mn**	**Cr**	**Ni**	**Mo**	**M_{d30} (°C)**
SS304L powder	-	0.01	0.08	0.5	1.5	19.0	10.3	0.01	-5.3
100% SS304L	70	0.01	0.09	0.56	1.42	18.94	9.90	0.01	-3.6
90% SS304L	50	0.01	0.09	0.63	1.25	16.89	8.75	0.05	35.4
	15	0.01	0.09	0.7	1.31	17.05	9.47	0.05	25.3
80% SS304L	62	0.01	0.09	0.64	1.27	16.73	9.08	0.05	34.2
	40	0.01	0.09	0.63	1.27	16.62	8.92	0.05	36.4
	13	0.01	0.09	0.61	1.23	16.72	8.64	0.05	39.2
SS304L substrate	-	0.02	0.04	0.46	1.26	18.25	8.02	0.07	43.3

Table 2.2. Processing parameters for 100%, 90%, and 80% SS304L walls, adopted from [126].

Number	Wall 1	Wall 2	Wall 3	Wall 4
Name	100% SS304L wall (low power)	90% SS304L wall	80% SS304L wall	100% SS304L wall (high power)
Powder composition	100 vol.% SS304L	90% vol.% SS304L + 10 vol.% iron	80% vol.% SS304L + 20 vol.% iron	100 vol.% SS304L
Laser power (W)	2300	2000	2000	4000
Scanning speed (mm/s)	8.5	10.6	10.6	10.6
Linear heat input (J/mm)	277	189	189	377
Powder flow rate (g/min)	18	15.5	15.5	23
Hatch spacing (mm)	2.5	2.5	2.5	2.5
Layer height (mm)	1.2	1.1	1.1	1.1

Chapter 3

Effect of processing parameters on microstructure and mechanical properties

3.1. Introduction

Previous research on AISI type 316, 316L, and 304 stainless steel components made by DED shows that the uniaxial tensile strength is lower but elongation higher in samples loaded along the transverse direction, or parallel to the vertical build direction, as compared with longitudinal samples, or those whose tensile axis is aligned with subsequent layers [4,17,19,60]. Zhang et al. [19] studied the effect of laser power and scanning speed on microstructure and mechanical properties by building 316 stainless steel components by DED with laser powers ranging from 600 W to 1400 W and scanning speeds ranging from 2 mm/s to 10 mm/s. They showed that yield and tensile strengths decreased with increasing laser power and decreasing scanning speed, as this combination results in slower cooling rates and therefore larger grains.

A summary of mechanical properties of austenitic stainless steel components made by AM, compared with wrought and annealed plate, is given in Table 3.1. The mechanical properties of components made by AM vary in the literature as the process parameters vary component, we compute the linear heat input when available for the studies in Table 3.1 as

---

Reproduced from: Z. Wang, T. A. Palmer, and A. M. Beese, "Effect of processing parameters on microstructure and tensile properties of austenitic stainless steel 304L made by directed energy deposition additive manufacturing," *Acta Mater.*, vol. 110, pp. 226–235, 2016 [2].

a metric for comparison of the thermal history variation between studies. This table shows that in general, components made by AM have higher yield and tensile strengths, than wrought materials of the same stainless steel alloy, with the measured elongations in AM having a wide variation between studies.

In the present work, the effect of processing parameters on the microstructure and tensile mechanical properties of 304L stainless steel fabricated by laser-based DED was investigated through both experimental characterization and the application of grain growth and grain size strengthening models. In particular, as the need arises for large structures to be fabricated by DED, higher deposition rates, corresponding to higher heat inputs and laser powers, will be required. However, little is known about what impact high linear heat inputs have on the microstructure and mechanical properties of these large builds as prior work has focused on small builds of 304, 316, or 316L stainless steel. By examining relatively high heat inputs compared to what has been previously reported, and the influence of varying linear heat input on microstructure and mechanical properties, the role of less severe solidification and cooling rates in AM on the mechanical properties of components was examined. By interpreting the experimental data through the application of existing processing-structure and structure-property models, a quantitative connection among processing, structure, and mechanical properties in AM is demonstrated.

3.2. Experimental procedures

Two walls deposited from 100 vol.% pre-alloyed SS304L powder, as described in Chapter 2, were investigated in this study. The processing parameters of the two walls are given in Table 2.2. Uniaxial tensile test specimens in accordance with ASTM E8 [91],

with a gauge length of 21.5 mm, gauge width of 4 mm, and thickness of 2 mm, were extracted from the two walls and the substrate by wire electrical discharge machining (EDM), as shown in Figure 3.1. From each wall, specimens were cut in two orientations: one set such that the tensile axis of each specimen was perpendicular to the build direction, denoted as longitudinal specimens, and the second set such that the tensile axis of each specimen was parallel to the build direction, denoted as transverse specimens. For comparison, specimens were also extracted from the annealed 304L substrate.

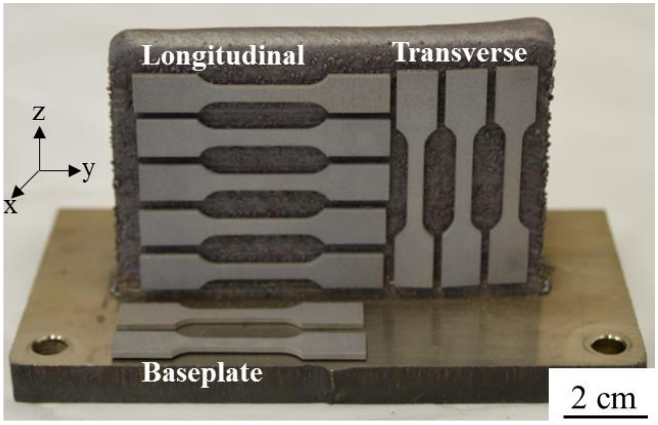

Figure 3.1. Photograph showing the positions from which tensile specimens were extracted in each wall. X is the thickness direction, y is the longitudinal direction, and z is the build, or transverse, direction.

Table 3.1. Summary of mechanical properties of AISI 304, 316 and 316L stainless steel fabricated by additive manufacturing compared with wrought properties reported in the literature.

	Stainless steel alloy	Laser power (W)	Scanning speed (mm/s)	Linear heat input (J/mm)	Density	Orientation	Yield strength (MPa)	Tensile strength (MPa)	Elongation (%)
Directed energy deposition									
Griffith et al., 2000 [60]	304	-	-	-	100%	Longitudinal Transverse	448 324	710 655	59 70
Griffith et al., 1996, 2000 [17,60]	316	-	-	-	100%	Longitudinal Transverse	593 448	807 793	30 66
Xue et al., 2010 [18]	316	-	-	-	93.2-97.4%	Longitudinal	363-487	648-970	20-44
Zhang et al., 2013 [19]	316	600-1400	2-10	75-500	-	Longitudinal Transverse	558 352	639 536	21 46
Milto et al., 2013 [92]	316	200-350	3-8	24-60	91%	Transverse	207-261	414-539	38-45
Yu et al, 2012 [4]	316L	570/750	13/17	45	99.6%	Longitudinal Transverse	490 280	685 580	51 62
Ma et al., 2013 [61]	316L	600-1650	7-23	69-90	96.5-97.5%	-	400-440	430-510	14-20
Wrought									
Guan et al., 2013 [22]	304						≥ 205	≥ 520	≥ 40
Tolosa et al., 2010 [59]	316						220-270	520-680	40-45

- Unspecified

The internal structure, including pores or defects, of the samples was visualized using X-ray computed tomography (CT), which is a nondestructive technique to examine the interior structure of bulk materials. Here, X-ray CT (General Electric phoenix v|tome|x m) was used to quantify the porosity of the samples made by AM and to visualize and quantify internal inclusions in two representative tensile specimens. Scans were performed using a 300 kV microfocus X-ray source with a GE DXR250 flat panel detector with a 200 µm pitch. Two sets of scanning parameters were used in the inspection of the specimens, depending on the desired level of resolution. For higher resolution scans with a voxel size of 25 µm, an accelerating voltage of 250 kV and a tube current of 100 µA were used with 800 projections per scan and a total scan time of 26 minutes. Lower resolution scans with a voxel size of 35 µm allowed for higher powers to be used with the x-ray tube, and accelerating voltages between 250 kV and 270 kV with corresponding tube currents of 150 µA and 130 µA, respectively, were used. For these two cases, 600 projections per scan and a total scan time of 14 minutes were used. These voxel sizes should allow for the identification of pores 50-70 µm in diameter or larger [93,94]. The scans were analyzed using VGStudio Max 2.2 visualization and analysis software.

To study the potential phase transformation from austenite to martensite, nondestructive magnetic permeability measurements were made using a feritescope (Fischer Feritescope FMP 30). The microstructure of as-deposited 304L contains paramagnetic austenite, ferromagnetic ferrite, and potentially ferromagnetic martensite. Thus, the magnetic permeability of the sample will indicate the presence of ferrite and martensite together [95–98]. While austenite has the potential to transform to martensite with plastic deformation [25,48,99], but there is no phase transformation of ferrite [100];

therefore, any increase in magnetic permeability can be attributed to a phase transformation from austenite to martensite.

Uniaxial tension tests were performed on an electromechanical testing frame (Instron 4202, 10 kN load cell) at a strain rate of $1.2x10^{-3}$/s. Digital image correlation (DIC), a non-contact method for measuring surface deformations, was used to compute surface strains using correlation software (Vic2D, Correlated Solutions). In this technique, the surface of each sample was painted white with a black speckle pattern. A digital camera (Point Grey GRAS-50S5M-C) was used to image the gauge region of the sample at 1 Hz during each test, with a pixel size of 90 μm. The surface deformations in the gauge region of each sample were computed based on digital images using a cubic B-spline interpolation algorithm with a subset size of 21 pixels and a step size of 5 pixels, resulting in a virtual strain gauge size of 56 pixels or 1.5 mm in the Vic2D software [101]. The axial strain in the gauge section of each sample was measured using a 21 mm long vertical virtual extensometer in the Vic2D software.

To examine the microstructure of the samples, samples were polished using 0.05 μm colloidal silica and electrolytically etched using 20 wt. % NaOH in DI water at 5 V for 4-10 s. The samples were observed using an optical microscope (Keyence VHX-2000) in which ferrite could be detected, as the NaOH solution preferentially attacks delta-ferrite rendering it dark in micrographs [102]; however, it was not possible to clearly distinguish grains with this method. Therefore, grains were observed using electron backscatter diffraction (EBSD; Oxford Nordlys Max2). For EBSD imaging, the samples were polished using 0.05 μm colloidal silica, and were not etched.

3.3. Results and discussion

3.3.1. Overview

The measured mechanical properties under uniaxial tension for all samples are given in Table 3.2, while representative engineering stress-strain curves of samples extracted from the two walls and annealed substrate are shown in Figure 3.2. As seen by the significant standard deviations in Table 3.2, strength and ductility vary between samples extracted from a single wall made by AM. The samples made by AM have reduced tensile strength and elongation as compared to the annealed substrate. With respect to processing conditions, in the same material direction, samples extracted from the low power wall exhibited higher yield and tensile strengths than samples extracted from the high power wall, while a similar, but weaker trend is seen in elongation.

For additively manufactured samples made using a single set of processing conditions, longitudinal specimens have lower elongation than transverse specimens, but there is no consistent trend in strength versus direction, which we explain in Section 3.3.3. Within the same wall, the yield and tensile strengths increase in longitudinal samples as the distance between the sample and the substrate, which was water cooled to room temperature, decreases (see Figure 3.3).

X-ray CT analysis was performed to visualize and quantify the volume fraction of pores and inclusions in selected samples prior to testing. No lack of fusion defects were found, but at the resolution of the X-ray CT scanning parameters used, a distribution of small spherical pores and inclusions with high contrast were detected, and classified as internal defects. The volume fractions of defects were found to be in the range of 0.048% to 0.191%

across both power levels. These rather low values verify that the mechanical responses measured here are not impacted by defects in the mechanical testing specimens.

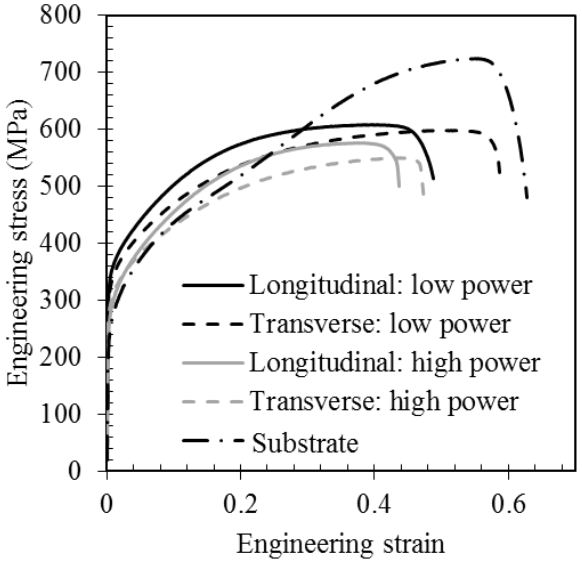

Figure 3.2. Representative engineering stress-strain curves of uniaxial tension samples extracted from the low power (2.3 kW) wall and high power (4 kW) wall in two directions, as well as a sample from the annealed substrate.

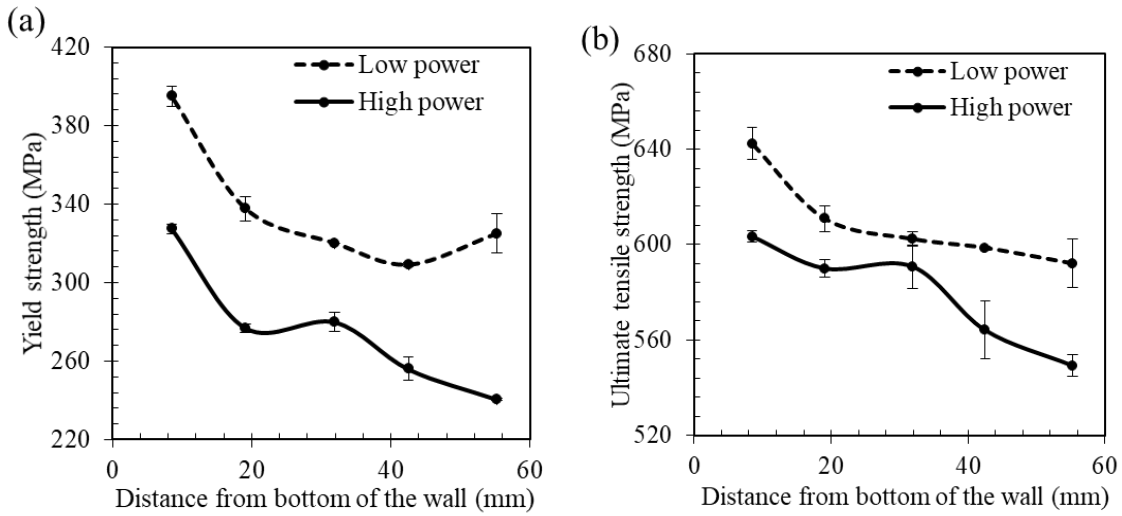

Figure 3.3. Yield (a) and ultimate tensile strength (b) in longitudinal samples as a function of the distance of the sample gauge region from the substrate.

Table 3.2. Summary of mechanical properties and increase in ferrite number after tensile tests. Values in the table are average ± standard deviation, where n indicates the number of samples tested in each condition.

	Low power wall		**High power wall**		**Annealed Substrate n = 4**
	Longitudinal n = 11	**Transverse n = 7**	**Longitudinal n = 10**	**Transverse n = 8**	
Yield strength (MPa)	337 ± 29	314 ± 6	277 ± 27	274 ± 7	265 ± 9
Ultimate tensile strength (MPa)	609 ± 18	606 ± 13	581 ± 20	560 ± 12	722 ± 14
Elongation (%)	48.2 ± 2.5	56.4 ± 5.8	41.8 ± 3.5	50.5 ± 6.7	62.3 ± 2.6
Δ Ferrite number (FN)	0.9 ± 0.3	1.3 ± 0.4	0.9 ± 0.3	1.0 ± 0.3	41.7 ± 4.1

3.3.2 Effect of processing parameters on grain size and morphology

The microstructures of longitudinal samples extracted from the low and high power walls are shown in Figure 3.4, where the relative sizes of grains and layer bands within each wall is seen in Figure 3.4a and Figure 3.4b. In the low power wall (Figure 3.4a), no grains span the approximately 0.8 mm tall layer height. In the high power wall (Figure 3.4b), some grains span the 1.2 mm layer height. Figure 3.4c and Figure 3.4d show the presence of columnar δ-ferrite dendrites inside the austenite matrix, but as shown in Figure 3.4c, upon magnification of the layer boundary in Figure 3.4b, there is no visible sharp transition in microstructural features across the layer boundary. During rapid solidification of austenitic stainless steels, the transformation from δ-ferrite to austenite is seldom fully complete, resulting in residual ferrite dendrites in the austenite matrix upon solidification [65].

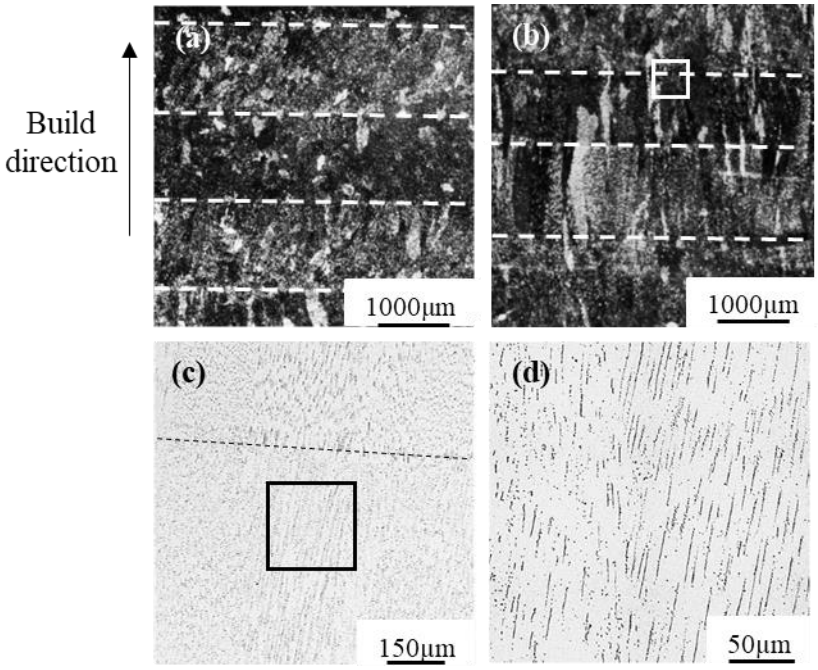

Figure 3.4. Optical micrographs of broken longitudinal samples in which the build direction is vertical and subsequent build layers are horizontal in the images. Dashed lines indicate the transition between subsequent build layers. (a) Image of a sample extracted from the low power wall showing short grains within single layers. (b) Image of a sample extracted from the high power wall showing slightly elongated grains extending the full layers. (c) Zoom in of inset in (b) showing the lack of a sharp transition in microstructural features between subsequent build layers in which the bright phase is austenite and the dark features are skeletal δ-ferrite dendrites. (d) Zoom in of inset in (c) showing δ-ferrite dendrites in the austenite matrix.

EBSD was used to quantitatively describe the size and morphology of the grains in the two additively manufactured walls as a function of position and linear heat input. Figure 3.5 shows representative inverse pole figures of samples extracted 15 mm from the top and 7 mm from the bottom of each of the two walls. Comparison of these images qualitatively

shows how the grain size and morphology change as a function of position within each of the two walls, as well as between the two walls. At the bottom of the walls, the microstructure contains columnar grains that appear to track the predominant heat flow path that results from the deposition of follow on layers. At the top of the walls, the microstructure is more irregular, but largely approaches an equiaxed morphology. The measured grain areas in Table 3.3 are largely skewed toward small grains; thus, a standard deviation is not appropriate to describe the data. These measurements of mean grain size indicate that in a single wall, grains at the top of the wall are larger than those at the bottom due to more rapid cooling at the bottom of the wall; the slower dissipation of heat as the distance from the substrate increases and heat builds up in the wall allows for grain coarsening at the top of the wall [63,103]. When comparing mean grain sizes from different walls, the samples extracted from the low power wall had smaller grains than those from the high power wall at the same position (Table 3.3). This is due to the fact that the higher linear heat input in the high laser power wall results in a larger melt pool, and therefore a smaller thermal gradient and slower cooling with respect to the wall built with the lower linear heat input [3,19,61].

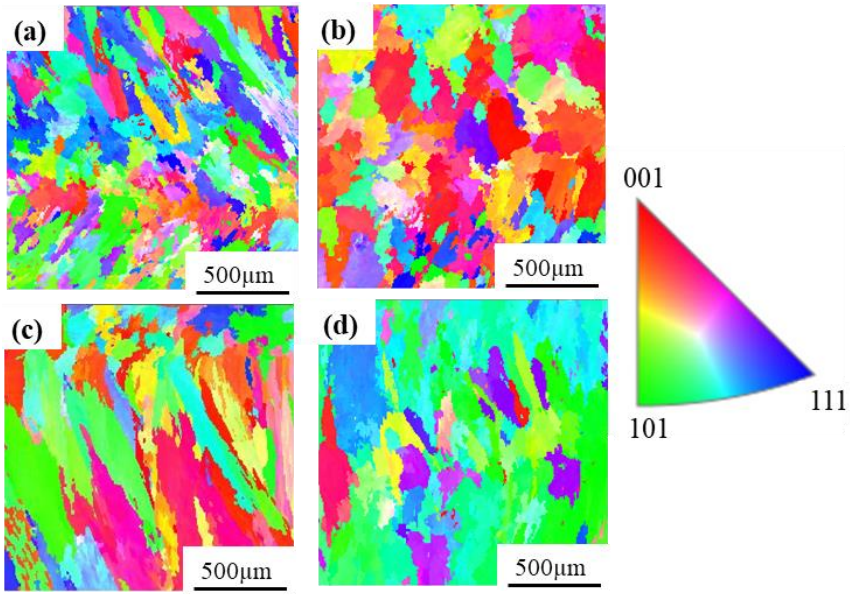

Figure 3.5. EBSD inverse pole maps of the y-z plane in longitudinal samples. Images of samples (a) 7 mm from the bottom of the low power wall, (b) 15 mm from the top of the low power wall, (c) 7 mm from the bottom of the high power wall and (d) 15 mm from the top of the high power wall.

To quantify the effect of processing conditions on grain size, literature on the effect of processing conditions on the solidification cooling rate in welds [104] as well as microstructures in the heat affected zone (HAZ) in welds is examined [105–109]. Relevant to the present study, researchers have developed models to describe the grain growth in the HAZ of a weld as a function of preheat temperature and linear heat input [108,109]. These models assume that grain growth is controlled by diffusion, and that no nucleation is needed, giving the growth rate of grains in the HAZ at a given temperature, T, as:

$$\frac{dg}{dt} = \frac{k_1}{2g} \exp\left(-\frac{Q}{RT}\right) \tag{3.1}$$

where g is the grain size, t is time, k_1 is a kinetic constant, and Q is the activation energy for grain growth. After integration, the grain size is given as:

$$g^2 = k_1 \alpha \tau \exp\left(-\frac{Q}{RT_P}\right) + g_0^2 \quad (3.2)$$

where g_0 is the initial grain size, T_P is the peak temperature, and α and τ are defined as:

$$\alpha = \sqrt{\frac{2\pi R T_P}{Q}}, \text{ and} \quad (3.3)$$

$$\tau = \frac{q/v}{2\pi\tau\lambda e} \frac{1}{(T_P - T_0)} \quad (3.4)$$

where q/v is the linear heat input, λ is the thermal conductivity, T_0 is the preheat temperature, and τ is the time to heat from T_0 to T_P. The material properties for austenitic steels are given in Table 3.4.

Table 3.3. Statistical information on grain size and grain morphology, as well as values used to determine the Hall-Petch relationship in stainless steel 304L produced by AM, in which a and b are the average lengths of major and minor axes, and d is the relevant grain dimension.

	Longitudinal				**Transverse**	
	Low power wall		**High power wall**		**Low power wall**	**High power wall**
	Top	**Bottom**	**Top**	**Bottom**	-	-
Grain size and morphology measurements						
Median of grain area (μm²)	1532	1149	1394	1329	-	-
Mean of grain area (μm²)	5942	3247	7610	6278	-	-
Average aspect ratio	2.0±0.9	2.3±1.0	2.8±1.5	3.2±1.7	-	-
a (μm)	62	49	82	80	-	-
b (μm)	31	21	29	25	-	-
Values used in Hall-Petch relationship						
d (μm)	31	21	29	25	55	81
Average yield strength (MPa)	325±10	395±5	241±1	328±3	314±6	274±7

Table 3.4. Material properties for austenitic stainless steels used for calibration of kinetic grain growth model.

Property	Value	Reference
Peak temperature of SS316 (K), T_p	2035	[110]
Activation energy of SS316 (kJ/mol), Q	197	[111]
Thermal conductivity of SS304L (W/m/K), λ	29	[104]

In general, these models show that at the same starting temperature, the time to heat increases with linear heat input, resulting in the growth of larger grains, and at the same linear heat input, the time to heat increases with preheat temperature, also resulting in the growth of larger grains.

In order to apply these models to additive manufacturing, one must determine if the deposited material may be considered as a HAZ in a weld, with a given initial grain size. Work on keyhole welding of stainless steel 304L has shown that as the linear energy input increases from 40 J/mm to 100 J/mm, the temperature gradient, *G*, cooling rate *GR*, which determines the scale of the solidification structure (where *R* is the solidification rate), and *G*/*R*, which determines the solidification morphology, all approach steady state values by 100 J/mm [104]. Therefore, as linear heat inputs of 271 J/mm and 377 J/mm were used in the present study, the scale and morphology of the solidified microstructure is not expected to differ significant between the conditions studied. Thus, we may assume that the initial solidified grain size is approximately constant as a function of position within these stainless steel 304L walls, as well as between the low and high linear heat input walls. We can therefore approximate the deposited material as a HAZ, and assume that the grain growth in additive manufacturing occurs due to the reheating cycles that the material is

exposed to as additional layers are deposited, analogous to those seen in a HAZ of a multi-pass weld.

We thus extrapolate the welding models to model the grain growth during thermal cycles between a preheat temperature and a peak temperature during deposition. As additional layers are deposited during AM, the temperature of the component increases, leading to an increase in weld pool size and a reduced thermal gradient [112,113]. This temperature increase with additional layers can be considered as a preheat temperature of the base material, or HAZ. Thermocouple measurements indicated that as the walls in the present study were built, the substrate temperature increased to a steady state value of 387°C (660K) throughout the deposition. Therefore, we can assume that during deposition, the preheat temperature of the HAZ is approximately room temperature (298K) near the substrate, while near the top of the build, a lower bound for the preheat temperature is taken to be 660K.

To apply the kinetic grain growth model shown in Eqns. (3.2) - (3.4), we calibrated the model using data from the high linear heat input wall, which results in larger grain growth than the low linear heat input wall. Assuming a preheat temperature of 298K at the bottom of the wall, and 660K at the top of the wall, Figure 3.6 shows the average grain area, g^2, versus τ, which gives calibrated constants of $g_0^2 = 1219\ \mu m^2$ and $k_1 = 1.9 \times 10^9\ \mu m^2/s$. These values are deemed reasonable, as the starting grain size is approximately 40 μm in diameter, and the k_1 value is the same order of magnitude as that found in [108].

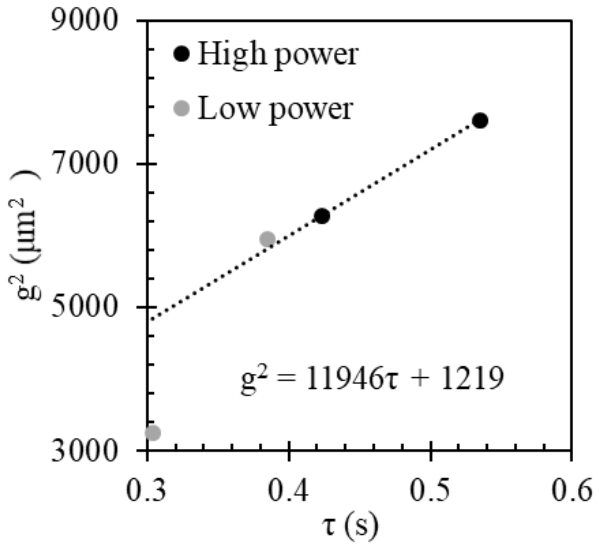

Figure 3.6. Average grain area versus time to heat for samples extracted 7 mm from the bottom and 15 mm from the top of both the low power wall and the high power wall, where average grain size was extracted from EBSD data shown in Figure 3.5 and detailed in Table 3.3. Data from the high power wall (black symbols) were used to fit the kinetic grain growth model, while data from the low power wall are shown in gray. The fitted line was used to calibrate the kinetic grain growth model to find the initial grain size, g_0, and the kinetic constant, k_1. This calibrated model was used to predict grain growth as a function of processing parameters for the low power wall.

With this calibrated grain growth model, the grain areas in the lower linear heat input wall were predicted to be 4856 μm^2 and 5813 μm^2, as shown in Figure 3.6, which are close to the experimentally measured mean grain areas shown in Table 3.3. We note that the prediction of grain growth at the top of the low power wall is more accurate than that at the bottom. Limitations of this model are that it considers the impact of the most severe thermal cycle on grain growth, but not subsequent cycles, nor the effect of the substrate

acting as a heat sink. However, this approach demonstrates that classical welding models of grain growth within the HAZ of a weld can be calibrated and extended to additive manufacturing in order to predict the grain size within a component as a function of processing history. The quantitative connection between processing and structure is critical for AM as the local grain size within components in turn dictates the mechanical properties as described in next section.

3.3.3 Effect of grain size and morphology on mechanical properties

3.3.3.1 Hall-Petch relationship

The Hall-Petch equation describes the relationship between grain size and yield strength in equiaxed metals as [114,115]:

$$\sigma_y = \sigma_0 + \frac{k}{\sqrt{d}} \tag{3.5}$$

where σ_y is the yield strength, d is the average grain diameter, and σ_0 and k are material constants.

In order to define the grain morphology in terms of a quantifiable metric, we approximate the grains in Figure 3.5 as elliptical and define the grain aspect ratio as the ratio of the major axis, a, to the minor axis, b, of each grain such that an aspect ratio of 1 indicates an equiaxed grain. Figure 3.7 is a histogram of the aspect ratios of the grains from the top and bottom of each of the two walls based on EBSD data shown in Figure 3.5. The average aspect ratios for the top and bottom of each wall are shown in Table 3.3. Comparing data for each wall independently, grains at the top of the wall were found to

have smaller aspect ratios, meaning they are more equiaxed than grains at the bottom of each wall. Comparing data between walls, it was found that the wall made by low linear heat input resulted in more equiaxed grains than the wall made using high linear heat input.

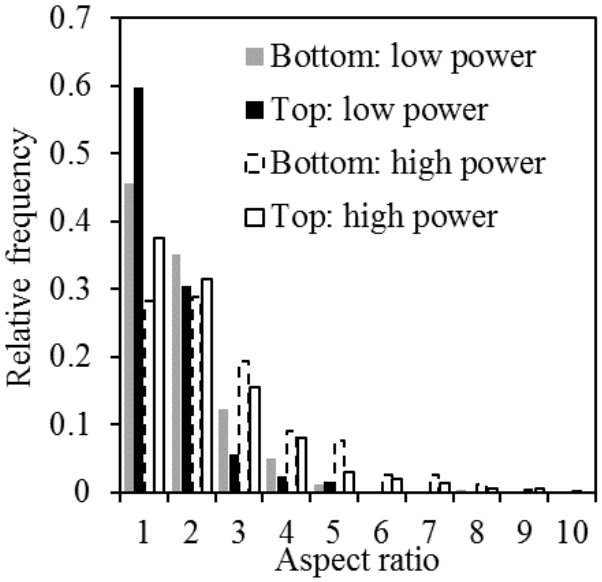

Figure 3.7. Histogram of grain aspect ratios for samples extracted 7 mm from the bottom, and 15 mm from the top, of both low power and high power walls. Data was extracted from EBSD maps, including those shown in Figure 3.5.

To link the grain size to the yield strength as a function of position, orientation, and linear heat input, we use the average grain areas, aspect ratios, and yield strengths presented in Table 3.3. In particular, to incorporate the potential anisotropy, we define a relevant grain dimension as the length of the grain in the direction of the applied tensile stress. Approximating the orientation of the elliptical grains as that in which the major axes are aligned with the build direction, the average lengths of major and minor axes are considered to be the relevant grain dimension, d, in the transverse, and longitudinal samples, respectively. Using the average grain areas and aspect ratios in Table 3.3, the average

lengths of the minor and major axes can be calculated using the following equations:

$$A = \pi ab \tag{3.6}$$

$$r = b/a \tag{3.7}$$

where A is the average grain size, r is the average aspect ratio of the grains at the given location and linear heat input, and a and b are the average lengths of the major and minor grain axes, respectively. The resulting a and b values are given in Table 3.3.

The yield strengths for longitudinal samples extracted from the top and bottom of each wall are plotted versus $d^{-0.5}$ using the minor axis of the relevant grains in Figure 3.8. Regarding samples tested in the transverse direction, the grain sizes and morphologies vary in these samples as a function of position; thus, the average of the major axis values from the top and bottom longitudinal samples is taken as the major axis of transverse sample made by the same laser power as shown in Table 3.3. Thus, in addition to longitudinal data in Figure 3.8, the average yield strengths for the transverse samples for the two walls are plotted versus $d^{-0.5}$ using the corresponding grain major axis values. The data of yield strength and d of each point plotted in Figure 3.8 are explicitly given in Table 3.3.

A linear fit of the yield strength versus relevant grain dimension gives values of σ_0 = 194 MPa and k = 695 MPa $\mu m^{-0.5}$ to describe the Hall-Petch relationship between yield strength and grain size. The values of σ_0 and k are in line with data of stainless steels [116]. While there are some discrepancies in the predicted yield strength versus $d^{-0.5}$, in that not all data lies on the line, likely due to the spread in grain size at a given position in these additively manufactured walls, the general trend of increasing yield strength with decreasing grain size is demonstrated.

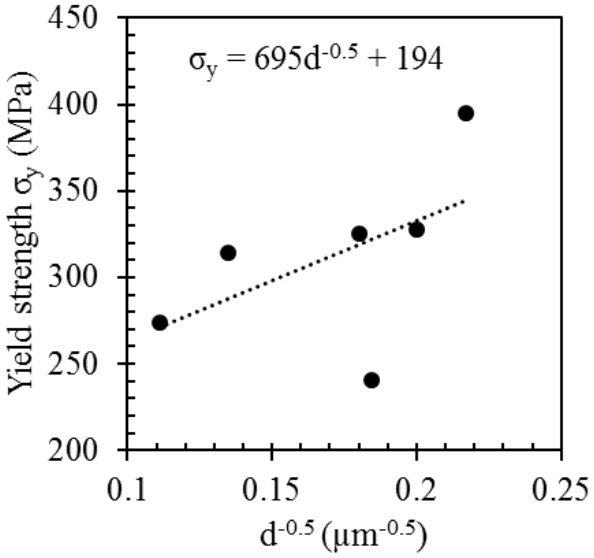

Figure 3.8. Yield strength versus $d^{-0.5}$, where d is the relevant grain diameter in the direction of applied tensile load. The fitted line was used to determine the Hall-Petch parameters, σ_0 and k.

In summary, in the same orientation, specimens from the low power wall have higher yield and tensile strengths than those in the high power wall due to grain boundary strengthening due to smaller grains. In a single wall, the grain size increases with increasing distance from the substrate, resulting in a decrease in yield and tensile strengths with increasing distance from the substrate as shown in Figure 3.3. The link between relevant grain dimension and yield strength is described by a Hall-Petch relationship.

3.3.3.2 Anisotropy

Due to large directional thermal gradients, the microstructures of components made by AM are anisotropic, which generally results in anisotropic mechanical properties. In austenitic stainless steels deposited by AM, microstructural grains and ferrite dendrites are

preferentially orientated along the highest thermal gradient [19]; however, due to the rapid solidification and subsequent remelting of material with the additional material layers, these dendrites are oriented chaotically within the components made by AM (see Figure 3.4c).

When a sample with long and narrow columnar grains orientated along the build direction is plastically deformed under uniaxial tension in the same direction, dislocations are required to cross fewer grain boundaries to elongate the sample, which results in lower yield and tensile strengths than in samples deformed along the longitudinal direction. This anisotropy in microstructure and mechanical properties is evident in other material systems produced by DED or PBF, such as Ti-6Al-4V, in which large columnar grains extend across numerous build layers [8,11,117]; however, the grains in the present study are confined to individual build layers, as shown in Figure 3.4a and Figure 3.4b.

In the low power wall, grains have small aspect ratios and grow within single layers. In the high power wall, grains are elongated with slightly higher aspect ratios, but virtually no grains extend across multiple layers. However, the presence or absence of anisotropy cannot be addressed directly in the present study due to the convolution of both direction and location in the tested samples. As shown in Figure 3.3, the yield and ultimate tensile strengths in longitudinal samples vary with position, while the average yield and ultimate tensile strengths in the transverse samples fall within the ranges of the corresponding longitudinal data. Since the gauge regions of the transverse samples span the gauge regions of approximately the three central longitudinal samples as shown in Figure 3.1, the effects of direction and location cannot be separated in the transverse samples. Thus, due to this

convolution of data from different directions and locations, the possible macroscopic anisotropy of mechanical properties in the walls made by AM cannot be determined.

3.3.4 Phase Transformation

The superior mechanical properties of the substrate compared to the material made by AM are attributed to the deformation-induced martensitic transformation that occurs in the annealed 304L, which results in significant strain hardening and high ductility [48,53,118]. The transformation from austenite to martensite in the annealed substrate material, and absence of this phase transformation in the additively manufactured material, was confirmed with magnetic permeability measurements and optical microscopy, and explained by elemental analysis.

The magnetic permeability of the tensile samples was measured in the gauge region before testing and after plastic deformation of the gauge regions of each sample. An increase in magnetic permeability with plastic strain in the substrate material confirms the phase transformation, while no significant change in magnetic permeability with plastic strain in the additively manufactured material indicates a lack of phase transformation in this material. Here, we report the ferrite number (FN), which is a measure of magnetic permeability of the sample, and which is the standard unit of measurement for reporting ferromagnetic content in welded austenitic stainless steels [119,120]. The feritescope measures the magnetic permeability of a finite volume of material, roughly equivalent to a cylinder of 2 mm in depth and 4 mm in diameter [121]. If the sample thins below 2 mm or the sample's width decreases below 4 mm, the output signal needs to be corrected for the reduced volume being measured. Thus, the corrected FN ($S_{FN,c}$) of a sample is given by:

$$S_{FN,c} = S_{FN,m} a\, b \tag{3.8}$$

where a is a thickness correction factor, b is a width correction factor [96,121], and $S_{FN,\,m}$ is the measured FN.

The magnetic permeability of the gauge region in each tensile specimen was measured before loading and after plastic deformation for some samples, and *in situ* during mechanical tests for others. Table 3.2 shows the increase in corrected FN in deformed specimens compared to their undeformed FN values:

$$\Delta FN = FN_t - FN_0 \tag{3.9}$$

where FN_t is the FN at a given deformation, and FN_0 is the initial FN in the undeformed sample.

The initial magnetic permeability readings in substrate samples and those made by additive manufacturing were found to be 1-3 FN in all cases. The resolution of FN measurements with the feritescope is on the order of 1-2 FN. Therefore, in samples extracted from the walls made by AM, the change in FN after plastic deformation, on the order of 1 FN (Table 3.2), is not significant, indicating little to no phase transformation with plastic deformation in these samples. However, the change in magnetic permeability measurement of 41.7 FN is significant in samples extracted from the annealed substrate, which is indicative of significant phase transformation from austenite to martensite in the annealed material.

The absence or occurrence of martensitic phase transformation can be verified by computing M_{d30}, as shown in Eqn. (1.1) proposed by Angel [46]. If the M_{d30} temperature of the annealed substrate or material made by AM is below room temperature, at which all the tests in this study were performed, it is unlikely that phase transformation will occur in

the specimens with plastic deformation. Based on the chemical analysis results in Table 2.1 and Eqn. (1.1), M_{d30} in the builds made by AM and the annealed substrate were calculated to be -3.6°C and 43.3°C, respectively. The low M_{d30} temperature in the deposited wall is due to the fact that the SS304L powder was manufactured by gas atomization in nitrogen, which is an austenite stabilizer. Gas atomization of the powder in nitrogen resulted in a higher nitrogen content in the powder and walls compared to the substrate. This explains the experimental observation of phase transformation in the substrate, in which the austenite phase was metastable, and the absence of transformation in the additively manufactured material, in which the austenite phase was stable.

The absence of a phase transformation in the 304L deposited by AM is significant as it resulted in a lower ultimate tensile strength than the annealed 304L plate, in which the microstructural phase transformation provided a high rate of macroscopic strain hardening.

3.4. Summary and conclusions

Two 304L stainless steel walls were fabricated using laser-based directed energy deposition additive manufacturing in order to elucidate the effect of processing parameters, namely linear heat input, on the anisotropic and heterogeneous tensile mechanical properties within a component. The primary conclusions from this study are:

- Slightly elongated grains grew along the build direction in the material made by AM, resulting in anisotropic elongation in which longitudinal specimens had lower elongations than transverse specimens. However, no clear anisotropy in macroscopic yield or tensile strength was identified in the present study.

- A kinetic grain growth model, originally formulated to describe the grain growth in the HAZ of welds, was calibrated and used to describe and predict the effect of linear heat input and location within an additively manufactured component on grain size. This provides a quantitative connection between processing parameters and microstructure for AM components.
- The location-dependent yield strength was found to follow a Hall-Petch dependence on location- and direction-dependent grain size, demonstrating a quantitative connection between heterogeneous, anisotropic microstructure and mechanical properties in AM.
- The wall fabricated using lower linear heat input had a finer microstructure, and therefore, higher yield and tensile strengths, than the wall fabricated with the higher linear heat input. The coarser microstructure at the top of the walls compared to the bottom of the walls was predicted to be due to a decreased cooling rate with increased distance from the substrate, which results in a lower yield and tensile strengths. The trend in grain size as a function of linear heat input and position corresponded to the predictions of the kinetic grain growth model. In addition, the yield strength as a function of grain size and morphology followed a Hall-Petch relationship.
- The ultimate tensile strength and elongation of samples extracted from the 304L stainless steel walls made by DED AM were found to be lower than those in the annealed substrate. This is due to the fact that strain-induced martensitic transformation, which provides high strain hardening and facilitates significant ductility, occurred in the annealed 304L plate, but not the 304L made by AM as the higher nitrogen content in the pre-alloyed powder stabilized the austenite phase in the deposited walls.

Acknowledgements

The financial support provided by the National Science Foundation through award number CMMI-1402978 is gratefully acknowledged. Any opinions, findings, and conclusions or recommendations expressed in this material are those of the authors and do not necessarily reflect the views of the National Science Foundation. We acknowledge Mr. Jay Tressler for the fabrication of the walls and Mr. Griffin Jones for performing the X-ray CT scans.

Chapter 4

Effect of chemistry on martensitic phase transformation kinetics and mechanical properties

4.1. Introduction

The ability for an austenitic stainless steel to undergo strain-induced phase transformation depends on the material's chemical composition, as this affects the stacking fault energy (SFE) of austenite [66]. Talonen and Hänninen [122] studied strain-induced martensitic phase transformation in 304 stainless steel and 301LN stainless steel, showing that the rate of phase transformation with respect to plastic strain depends on composition and temperature. Angel [46] investigated the effect of chemistry on strain-induced martensitic phase transformation in austenitic stainless steels and showed that carbon, nitrogen, chromium, nickel, silicon, manganese, and molybdenum increased the SFE of austenite, and therefore, increased austenite stability and decreased the strain-induced martensite finish temperature. Tomimura et al. [123] found that the amount of strain-induced martensite increased with the increase in the weight fraction of chromium and nickel in cold rolled austenitic stainless steels.

The elemental composition of additively manufactured components depends on the chemistry of the initial powder, any absorption of oxygen, nitrogen, or argon from the chamber environment during fabrication, or elemental vaporization during deposition,

---

Reproduced from: Z. Wang and A. M. Beese, "Effect of chemistry on martensitic phase transformation kinetics and resulting properties of additively manufactured stainelss steel," *Acta Mater.*, vol. 131, pp. 410–422, 2017 [124].

and can vary with location within components [2,8,125,126]. As discussed in Chapter 3, SS304L components produced by DED showed that when using pre-alloyed SS304L powder gas atomized in nitrogen, the 4 wt.% increase in nitrogen with respect to traditionally annealed SS304L, stabilized the austenite, resulting in no phase transformation in the additively manufactured materials, while phase transformation was apparent in the annealed SS304L with plastic deformation. Rafi et al. [126] studied the influence of build environment on microstructure and mechanical properties of additively manufactured 17-4 PH stainless steel. They found that the components contained a mixture of retained austenite (50-75 vol.%) and thermally-induced martensite (25-50 vol.%) when built in nitrogen, and mostly thermally-induced martensite (92 vol.%) when built in argon. The component built in nitrogen had a higher fracture toughness than the component built in argon due to the strain-induced austenite-to-martensite phase transformation present in the former.

In addition to depending on the powder composition and build environment, the chemical composition of components made by AM can vary from the initial powder composition, and as a function of position, if volatile elements vaporize from the molten pool during deposition [41]. The amount of elemental depletion is affected by the temperature of the molten pool, which is dependent on the temperature of the layer onto which new material is being added, as well as the energy input [113]. The most volatile elements in SS304 are chromium, nickel, and manganese [127], all of which increase austenite stability; therefore, depletion of these elements should impact the propensity for strain-induced martensitic phase transformation.

The strain-induced martensitic phase transformation in traditionally annealed or rolled austenitic stainless steels has been well studied [45–53], but little is known about the martensitic phase transformation kinetics in additively manufactured stainless steels. The aim of this work was to investigate the effect of initial powder chemistry, and spatial chemical composition changes due to vaporization, on the strain-induced martensitic phase transformation in SS304L made by DED. The chemistry as a function of location and starting composition was quantified, and the resulting phase transformation was characterized during uniaxial tension tests using *in situ* magnetic permeability measurements confirmed with time of flight neutron diffraction. A phase transformation kinetics equation that describes the amount of strain-induced martensite as a function of plastic strain, and in which the parameters depend on chemistry through the martensite finish temperature, is proposed and calibrated for the additively manufactured 304L stainless steel.

4.2. Experimental procedures

Two walls deposited from a mixture of pre-alloyed SS304L powder and iron powder, referred as the 80% and 90% SS304L walls as described in Chapter 2, were studied. During the deposition of each wall, the substrate was clamped with 4 bolts to an aluminum fixture, and a thermocouple was attached to the bottom of the stainless steel substrate to measure the temperature during the build process. To mix the powders, the pre-alloyed SS304L powder and pure Fe powder were combined in a sealed container filled with argon and put in a Type T2C Turbula mixer (Willy A. Bachofen AG Maschinenfabrik, Switzerland), which moved in three dimensions for 1 hour to ensure random mixing of the two powder

types. EDS mapping of different regions from the 80% and 90% SS304L walls showed no elemental segregation (Figure 4.1), which was indicative of sufficient mixing of the powders.

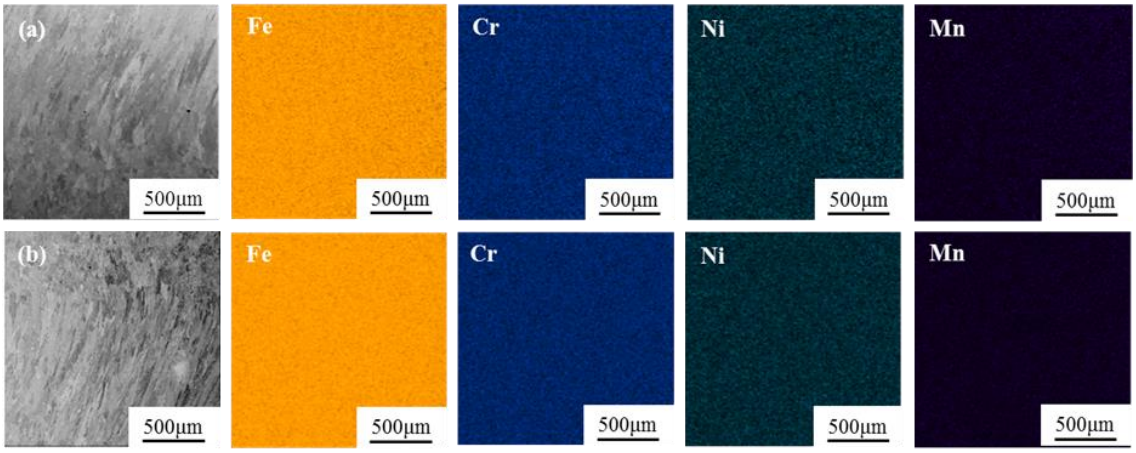

Figure 4.1. EDS maps of a representative region from the (a) bottom grip and (b) top grip of a transverse specimen from the 90% SS304L wall showing uniform distribution of major elements.

Uniaxial tension specimens were extracted from longitudinal and transverse orientations and different locations from the 80% and 90% SS304L walls by wire EDM with gauge dimensions of 21.5 mm long x 4 mm wide x 1.5 mm thick, adhering to ASTM E8 [91].

The X-ray CT was used to detect the size, shape, and location of internal defects in two representative uniaxial tension specimens from the 80% SS304L wall before mechanical testing. The scans were performed using a beam power of 200 kV, a current of 87 μA, a voxel size of 17.5 μm, a scan time of 20 minutes per sample, and a total of 1200 projections per scan. The voxel size used allows for the detection of pores 35 μm or larger in diameter

[2,93]. The acquired scans were analyzed using VGStudio Max 2.2 visualization and analysis software.

The amount of strain-induced austenite-to-martensite phase transformation in the SS304L samples was determined through magnetic permeability measurements using a feritescope (Fisher Feritescope FMP 30). Due to negative magnetostriction, or the Villari effect, the magnetic permeability of ferromagnetic materials decreases when subjected to tension as a result of rotation and re-orientation of magnetic domains in ferromagnetic materials with applied force [96,128]. In order to reduce the impact of the Villari effect on magnetic permeability measurements, specimens must be unloaded during the measurements so that they are macroscopically stress-free. In this study, the specimens were loaded to 7% engineering strain, unloaded to measure the magnetic permeability in macroscopically stress-free samples, and then loaded to another increment of 7% engineering strain before unloading and taking the next set of measurements.

Both monotonic and periodic loading/unloading uniaxial tensile tests were conducted using an electromechanical testing frame (Instron 4202, 10 kN load cell) at a strain rate of $1.2 \times 10^{-3}\ s^{-1}$. A subset size of 21 pixels with a step size of 5 pixels was used in DIC analysis, resulting in a virtual strain gauge size of 56 pixels or 1.5 mm [101]. A 21 mm-long virtual extensometer was used to calculate axial strain in the gauge region of each specimen. For periodic loading/unloading tensile tests, a feritescope probe was placed perpendicular to the gauge of each specimen, and kept in direct contact with the specimen throughout the tensile test to record the evolution of martensite content. The martensite volume fraction, c, can be estimated from the feritescope output, S_{Fe}, using the following equation:

$$c = k\, S_{Fe} \tag{4.1}$$

where k is the conversion factor from vol.% ferrite to vol.% martensite.

The conversion factor, k, was determined by measuring the martensite content in deformed regions of annealed 304L stainless steel after plastic deformation. Time of flight neutron diffraction was performed at three points with different amounts of plastic deformation using the VULCAN instrument at the Spallation Neutron Source at Oak Ridge National Laboratory [129]. A detailed description of VULCAN can be found in [130,131]. The martensite volume fractions at the three points with different plastic strain levels were determined from the diffraction patterns and compared with the feritescope readings to compute the conversion factor, k. A schematic of the neutron diffraction experimental setup is given in Figure 4.2. The two detector banks recorded diffraction patterns from grains that had *hkl*-specific lattice planes normal to the length and thickness directions. The peak positions and integrated peak intensities of the diffraction peaks from austenite (γ, fcc) and martensite (α', bcc) were computed using VDRIVE software in order to calculate the phase fractions of austenite and martensite [132].

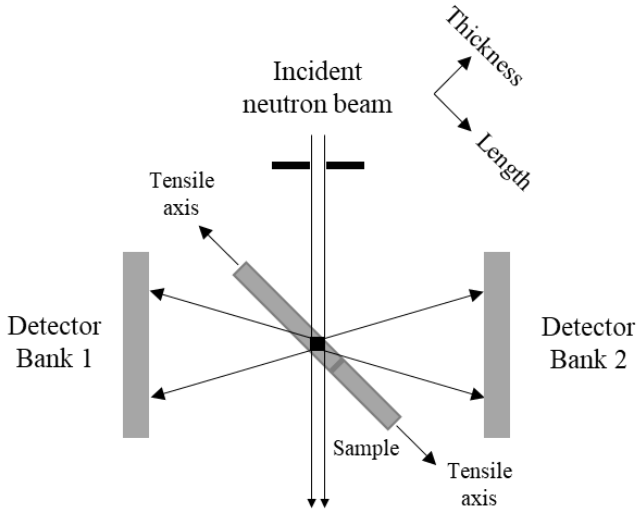

Figure 4.2. Schematic of neutron diffraction experimental setup, in which diffraction signals from length and thickness directions were collected.

The internal standard method, described below, was used to determine the volume fraction of austenite and martensite in SS304L. The intensity of an *hkl* peak in austenite ($I_{hkl,\gamma}$) is expressed as [133]:

$$I_{hkl,\gamma} = \frac{K_e \, K_{hkl,\gamma} V_\gamma}{(\mu/\rho)_m} \tag{4.2}$$

where K_e is an experimental system constant determined by the incident beam intensity and wavelength, diffractometer radius, and diffraction angle, V_γ is the vol.% of austenite, $(\mu/\rho)_m$ is the mass absorption coefficient in SS304L, and $K_{hkl,\gamma}$ is a constant for an *hkl* peak in austenite, given as:

$$K_{hkl,\gamma} = \frac{M_{hkl,\gamma}}{v_\gamma^2} \left|F_{hkl,\gamma}\right|^2 (d_{hkl,\gamma}{}^4 sin\theta) \tag{4.3}$$

where $M_{hkl,\gamma}$ is the multiplicity of an *hkl* peak of austenite, v_γ is the volume of a unit cell of austenite, $F_{hkl,\gamma}$ is the structure factor of an *hkl* peak of austenite, $d_{hkl,\gamma}$ is an *hkl*-specific

lattice spacing in austenite, θ is the diffraction angle (45° here), and $d_{hkl,\gamma}{}^4 sin\theta$ is the Lorentz factor in neutron diffraction.

Therefore, we have:

$$\frac{V_\gamma}{V_{\alpha'}} = \frac{I_{hkl,\gamma} K_{hkl,\alpha'}}{I_{hkl,\alpha'} K_{hkl,\gamma}} \tag{4.4}$$

where $V_{\alpha'}$ is the vol.% of martensite, $K_{hkl,\alpha'}$ is a constant for an *hkl* peak in martensite, $I_{hkl,\alpha'}$ is an *hkl* peak intensity in martensite. The peak intensity and d-spacing are determined from neutron diffraction data.

The uncertainty in martensite content measured by neutron diffraction ($u_{V\alpha'}$) is due to the uncertainty in the peak intensity measurement. Using a propagation of uncertainty approach, this uncertainty is given by:

$$u_{V\alpha'} = \frac{[(100 K_{hkl,\gamma} \delta I_{hkl,\alpha'})^2 + (K_{hkl,\gamma} \delta I_{hkl,\alpha'})^2 + (K_{hkl,\alpha'} \delta I_{hkl,\gamma})^2]^{\frac{1}{2}}}{I_{hkl,\alpha'} K_{hkl,\gamma} + I_{hkl,\gamma} K_{hkl,\alpha'}} \tag{4.5}$$

where $\delta I_{hkl,\alpha'}$ is the uncertainty in the $I_{hkl,\alpha'}$ measurement, and $\delta I_{hkl,\gamma}$ is the uncertainty in the $I_{hkl,\gamma}$ measurement.

The Vickers microhardness was measured along the height of the 80% and 90% SS304L walls using a load of 200 g and a dwell time of 15 s (Leco MHT Series 200). In each wall, the indentations were conducted at 10 heights, which started at 10 mm from the top of the wall, and were spaced 7 mm apart down the wall. A minimum of five measurements were taken at each height.

The microstructures of specimens were characterized using an optical microscope (OM; Keyence VHX-2000) and electron backscatter diffraction (EBSD; Oxford Nordlys Max2). The specimens were polished using 0.05 μm colloidal silica for observation of lack-of-fusion pores in OM and identification of phases by EBSD.

4.3. Results and discussion

4.3.1 Overview

Representative engineering stress-strain curves of longitudinal and transverse specimens from the 80% and 90% walls are given in Figure 4.3, as well as representative curves from the 100% SS304L walls and annealed SS304L substrate (as detailed in Chapter 3) as a comparison, while uniaxial mechanical properties for samples from the three walls and substrate are given in Table 4.1. Specimens from the 100% SS304L wall had a lower ultimate tensile strength and elongation to failure compared to the annealed SS304L, while the ultimate tensile strengths and elongations to failure of specimens from the 90% and 80% SS304L were comparable to those of the annealed SS304L.

Among the three additively manufactured walls, for specimens cut from the same orientation, there was no clear trend in yield strength, but the ultimate tensile strength increased with increasing iron powder. The elongations to failure in the 80% and 90% SS304L walls were higher than those in the 100% SS304L wall. For specimens cut from the 100% and 90% SS304L walls, there was no clear trend in yield strength and ultimate tensile strength with respect to direction, which agrees with the results in Chapter 3. However, the transverse specimens from the 80% SS304L wall had significantly lower elongations to failure, ultimate tensile strengths, and ΔFN than the longitudinal specimens in the same wall. This is because these samples had lack-of-fusion pores (e.g., [11], about 0.2 vol.%) as verified by X-ray CT analysis. These pores were oriented with their long axes perpendicular to the build direction. The build direction corresponds to the tensile axes in transverse samples as shown in Figure 4.4. The sharp corners of these lack-of-fusion pores serve as stress concentration sites when tension is applied in the build direction.

The reduction in ductility that results from the presence of these internal defects reduces the span of the test, and correspondingly, the ultimate tensile strength and amount of strain-induced martensite were limited in the build direction when lack-of-fusion porosity was present.

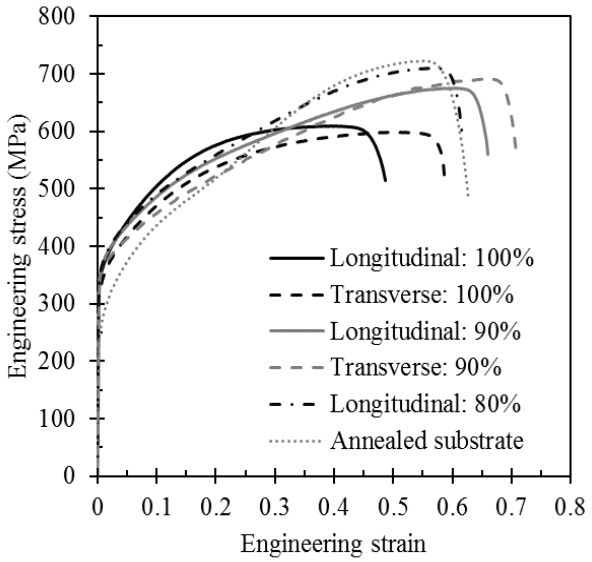

Figure 4.3. Representative engineering stress-strain curves of uniaxial tension samples extracted from 100%, 90%, and 80% SS304L walls in two directions, compared with the annealed SS304L substrate.

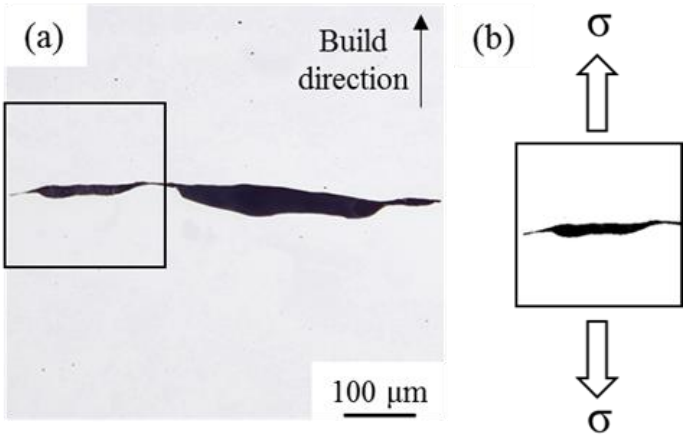

Figure 4.4. (a) Optical micrograph showing a lack-of-fusion pore in the 80% SS304L wall. (b) Inset in (a) showing that tension applied in the transverse direction (denoted by the vertical arrows) will open the lack-of-fusion pore.

Table 4.1. Summary of mechanical properties of samples from 100%, 90%, and 80% SS304L walls compared to the annealed SS304L substrate. Values are given as average ± standard deviation, and here n indicates the number of tested samples in each condition, "L" denotes "Longitudinal" and "T" denotes "Transverse".

	100% SS304L		**90% SS304L**		**80% SS304L**		**Annealed SS304L**
	L n = 11	**T n = 7**	**L n = 17**	**T n = 2**	**L n = 15**	**T* n = 6**	**n = 4**
Yield strength (MPa)	337 ± 29	314 ± 6	339 ± 25	342, 320	342 ± 12	333 ± 8	265 ± 9
Ultimate tensile strength (MPa)	609 ± 18	606 ± 13	683 ± 26	700, 693	722 ± 16	472 ± 69	722 ± 14
Elongation to failure (%)	48.2 ± 2.5	56.4 ± 5.8	64.3 ± 3.4	70.7, 67.4	60.3 ± 3.6	14.3 ± 9.0	63.3 ± 3.6
Δ Ferrite number (FN)	0.9 ± 0.3	1.3 ± 0.4	33.3 ± 5.1	26.6, 26.3	41.7 ± 3.7	3.5 ± 5.3	41.7 ± 4.1

*The transverse samples from the 80% SS304L wall had lack-of-fusion pores, which reduced all reported properties in transverse specimens.

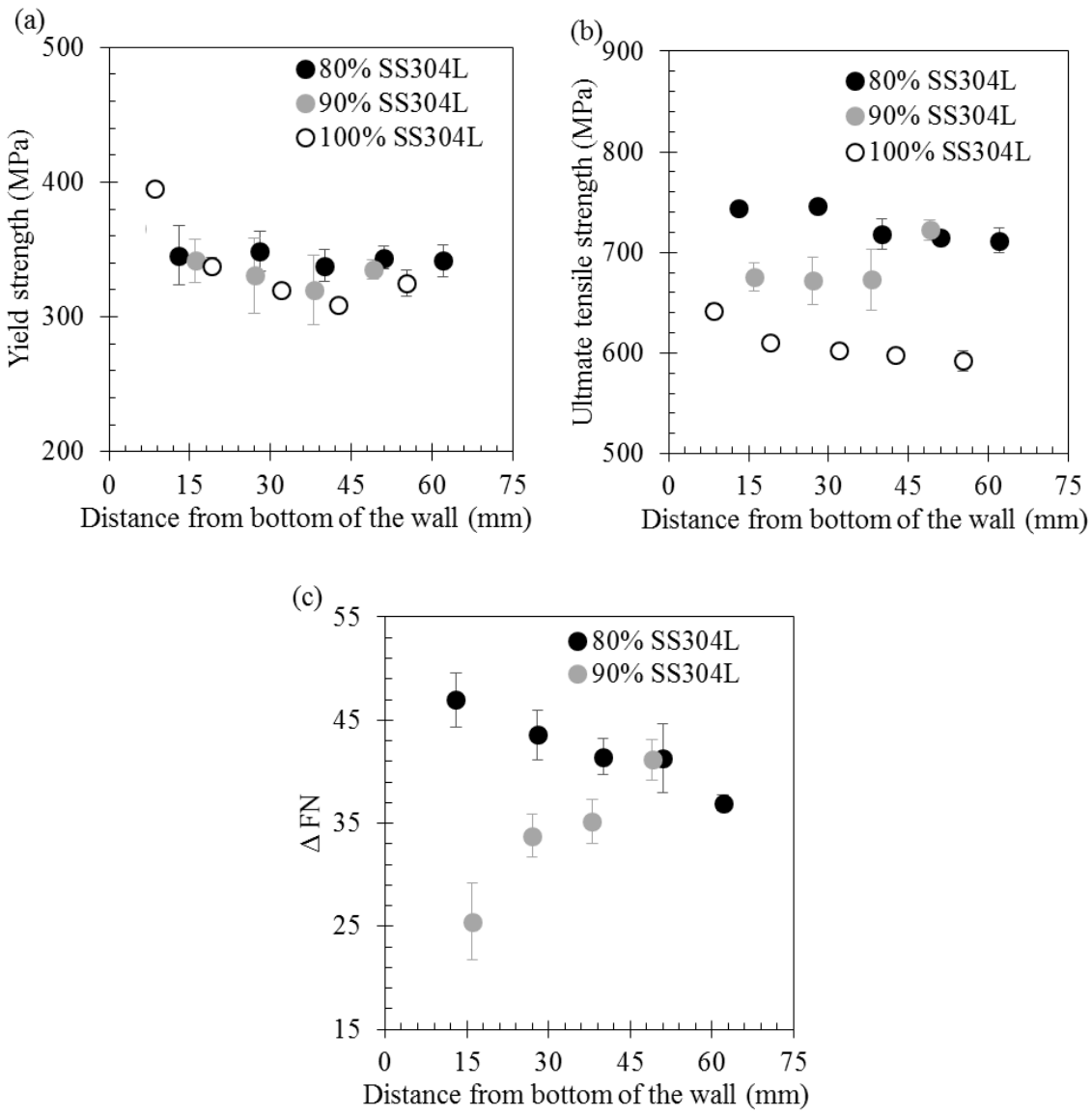

Figure 4.5. (a) Yield strength, (b) ultimate tensile strength, and (c) Δ FN as a function of distance of the sample gauge region from the substrate in the 80%, 90%, and 100% SS304L walls.

Regarding heterogeneity of properties, in longitudinal specimens from the 100% SS304L wall, the yield and ultimate tensile strengths decreased as the distance from the substrate increased, as shown in Figure 4.5a and Figure 4.5b. During additive manufacturing, with the deposition of new layers, the dissipation of heat through the wall

and substrate decreases due to the added energy and increased temperature of the wall. Therefore, the temperature of the top layer onto which a new layer will be deposited, as well as the molten pool in that layer, increases with height [19,63,113].

The evolution of the temperature of the top layer as a function of height during deposition was approximated using a simplified finite element simulation (ABAQUS/Standard 6.14 [134]). Here, we considered heat conduction in the additively manufactured SS304L wall, SS304L substrate, and aluminum fixture to which the substrate was clamped. The bottom of the 101 mm tall aluminum fixture was approximated to be at room temperature (25 ^{o}C) and the entire top surface of the build was assumed to be at a uniform to-be-determined temperature. The thermal contact conductance between the SS304L substrate and aluminum depends on the contact pressure [135]. Assuming that each of the 4 clamping bolts applied approximately 2 kN (corresponding to hand tightening of the bolts [136]) of force results in a thermal contact conductance between the substrate and fixture of 1000 W/m^2/K [137]. The other thermal properties used in the simulations are given in Table 4.2. The computed temperature of the top layer of the build, as a function of build height, that results in the temperature measured experimentally by the thermocouple at the bottom of the substrate is given in Figure 4.6. This analysis shows that the temperature of the top layer, and therefore, that of the molten pool, increases with build height.

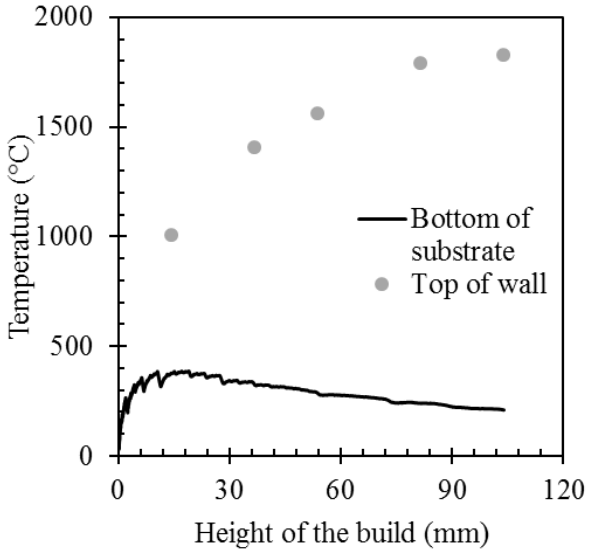

Figure 4.6. Measured temperature at the bottom of the substrate, and computationally predicted temperature of the top layer of the build, as a function of the height of the build.

Table 4.2. Material properties for steel and aluminum used for finite element simulation, where T represents temperature in K.

Property	**Value**	**Reference**
Thermal conductivity of SS316L (W/m/K)	11.82 + 0.0106 T	[113]
Thermal conductivity of Al (W/m/K)	247	[135]
Thermal contact conductance between low carbon steel and Al ($W/m^2/K$)	1000	[137,138]

The increase in temperature and decrease in cooling rate with height allow for grain coarsening and result in a decrease in yield and ultimate tensile strengths with height in the 100% SS304L wall. In longitudinal specimens from the 80% and 90% SS304L walls, the yield strength was almost constant as a function of position (Figure 4.5a) due to notable scatter. The ultimate tensile strength decreased with height in the 80% SS304L wall and increased with height in the 90% SS304L walls, as shown in Figure 4.5b, which is likely

due to the effect of local chemistry on martensitic transformation as will be discussed in Sections 4.3.2 and 4.3.3.

The microhardness was measured as a function of height in the 80% and 90% SS304L walls. In both walls, there was no clear trend in hardness with respect to location. The average hardness in the 80% SS304L wall was 198 ± 14 HV, which is comparable to the average hardness in the 90% SS304L wall of 203 ± 13 HV.

4.3.2. Effect of powder chemistry on microstructure and mechanical properties

The higher ultimate tensile strength and ductility of specimens from the 80% and 90% SS304L walls compared to the 100% wall resulted from the microstructural phase transformation from austenite to martensite during deformation, which was verified by magnetic permeability measurements. The increase in FN from the initial measurements to the final measurement of FN in the plastically deformed gauge section of each sample is given in Table 4.1. There was a significant increase in FN in specimens from the 80% and 90% SS304L walls and the annealed SS304L substrate, indicating the presence of strain-induced martensitic phase transformation. The increase in FN after deforming specimens from the 100% SS304L wall was on the same order of the feritescope resolution (about 1-2 FN), indicating that there was no detectable phase transformation in specimens from this wall.

The martensitic phase transformation in the 80% and 90% SS304L walls was also confirmed by EBSD analysis. Both ferrite and strain-induced martensite have body-centered cubic crystal structures, while austenite is face-centered cubic. Therefore, during

plastic deformation, any increase in the volume fraction of the bcc phase is indicative of martensitic phase transformation. Figure 4.7 shows EBSD phase maps in a specimen from the 90% SS304L wall. There was a 46 area % increase in the bcc phase content in the deformed gauge region compared with the undeformed grip region. This corresponds to an increase of 26 FN when assuming that area % is approximately equal to vol.% and this volume fraction is converted to ΔFN using the conversion factor that will be discussed in Section 4.3.4. The computed ΔFN from EBSD analysis agreed with the feritescope ΔFN reading of 25 for this sample. Together, these results confirm the strain-induced martensitic phase transformation in the 90% SS304L wall.

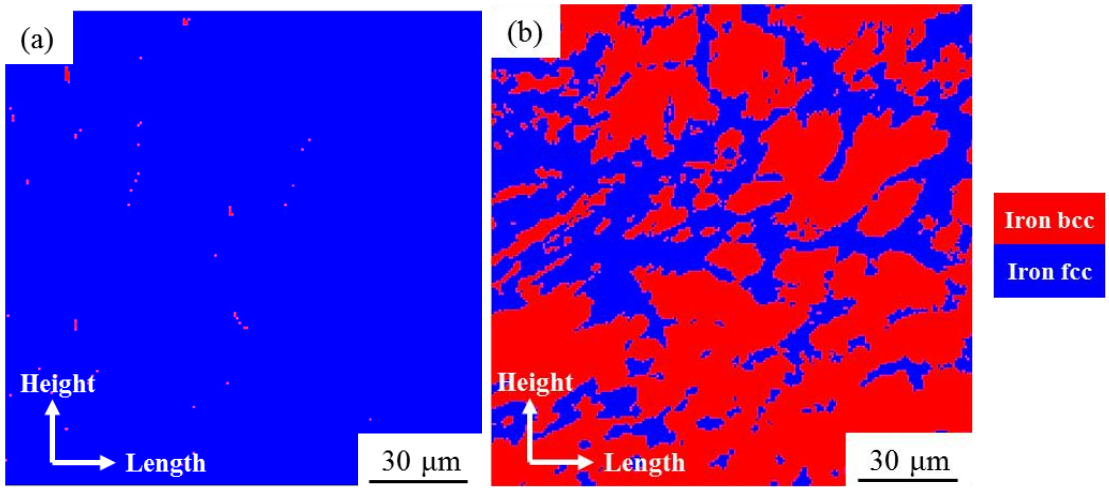

Figure 4.7. EBSD phase maps from a longitudinal specimen extracted from the 90% SS304L wall (a) before plastic deformation, and (b) after plastic deformation under uniaxial tension to a total engineering strain of 66%.

The presence or absence of strain-induced martensitic transformation can be explained by the computed M_{d30}. If the M_{d30} of an austenitic stainless steel is below room temperature, which is the temperature that all mechanical tests were performed in this study, it is unlikely

that strain-induced phase transformation will occur. However, if the M_{d30} is above room temperature, it is possible that the strain-induced phase transformation will occur. Based on the chemical analysis results in Table 2.1 and Eqn. (1.1), the M_{d30} temperatures computed of specimens from different locations from the 80% and 90% SS304L walls were above 25 ^{o}C. Thus, strain-induced martensitic phase transformation was anticipated in those walls at room temperature. The M_{d30} temperature computed for the 100% SS304L wall was -3.6 ^{o}C, indicating that strain-induced phase transformation was unlikely to occur in the 100% SS304L material. Mixing the pre-alloyed SS304L powder with iron powder reduced the relative weight fraction of elements that increase the SFE of austenite (silicon, manganese, chromium, and nickel), which resulted in higher M_{d30} temperatures in the 80% and 90% SS304L walls compared to the 100% SS304L wall. Therefore, the austenite was metastable and transformed to martensite with plastic deformation in the 80% and 90% SS304L walls. Since martensite has a higher flow stress than austenite [139], this evolution of microstructure, with increasing martensite and decreasing austenite with plastic strain in the 80% and 90% SS304L walls increased the strain hardening rate, therefore stabilizing the neck and increasing elongation to failure, and also increasing the ultimate tensile strength over the 100% SS304L wall as shown in Table 4.1.

The propensity for strain-induced martensitic transformation can also be estimated by computing the stacking fault energy (SFE) of the material. Decreasing SFE in austenitic stainless steels results in wider stacking faults, which are nucleation sites for hcp ε martensite, and which transform to α' martensite with plastic deformation. It is reported that austenite has the potential to transform to strain-induced martensite when the SFE is

less than approximately 20 mJ/m^2 [140,141]. Olson and Cohen proposed a thermodynamic model to calculate the SFE for austenitic stainless steels, which is given as [142]:

$$\gamma_{SFE} = 2\rho\Delta G^{\gamma\rightarrow\varepsilon} + 2\sigma \tag{4.6}$$

where γ_{SFE} is the stacking fault energy, σ is the surface energy, $\Delta G^{\gamma\rightarrow\varepsilon}$ is the Gibbs energy difference between γ austenite and ε martensite, and ρ is the molar surface density of {111} planes of austenite, defined as:

$$\rho = \frac{4}{\sqrt{3}a^2 N_A} \tag{4.7}$$

where a is the lattice parameter of austenite, and N_A is Avogadro's constant. The values of the constants used in the SFE calculation here are given in Table 4.3.

The change in Gibbs energy for the phase transformation from γ-austenite to ε-martensite, $\Delta G^{\gamma\rightarrow\varepsilon}$, is expressed as [141,143,144]:

$$\Delta G^{\gamma\rightarrow\varepsilon} = \sum_i x_i \Delta G_i^{\gamma\rightarrow\varepsilon} + \sum_{ij} x_i x_j \Omega_{ij}^{\gamma\rightarrow\varepsilon} + \Delta G_{mg}^{\gamma\rightarrow\varepsilon} + \Delta G_{int}^{\gamma\rightarrow\varepsilon} \tag{4.8}$$

where $x_{i,\,j}$ is the molar fraction of pure elements, $\Omega_{ij}^{\gamma\rightarrow\varepsilon}$is the excess free energy, $\Delta G_i^{\gamma\rightarrow\varepsilon}$ is the chemical contributions of each element to the change in Gibbs energy, $\Delta G_{mg}^{\gamma\rightarrow\varepsilon}$ is the magnetic contribution, and $\Delta G_{int}^{\gamma\rightarrow\varepsilon}$ is the contribution of nitrogen segregation

The parameters $\Delta G_i^{\gamma\rightarrow\varepsilon}$, $\Omega_{ij}^{\gamma\rightarrow\varepsilon}$, $\Delta G_{mg}^{\gamma\rightarrow\varepsilon}$, and $\Delta G_{int}^{\gamma\rightarrow\varepsilon}$ in Eqn. (4.8) are given in [141,143,144] and the molar fraction of each element is calculated based on Table 2.1. The SFE of the 100%, 90%, and 80% SS304L walls at room temperature can be calculated using Eqns. (4.6) - (4.8), with the resulting values given in Table 4.3. A decrease in SFE results in a decrease in austenite stability and an increase in the potential for strain-induced martensitic phase transformation. As shown in Table 4.3, the SFE from high to low, or the potential for strain-induced martensitic phase transformation from low to high in the

additively manufactured walls is: 100%, 90%, then 80% SS304L. This trend matches that of the computed M_{d30} temperatures in Table 2.1. Note that the computed SFEs of all SS304L walls are higher than 20 mJ/m^2, which is likely due to the fact that this model describes the idealized SFE of an infinite stacking fault without defects, while the SFE of actual materials is affected by grain size, dislocations, and point defects [143]. Studies by Moallemi et al. [140] and Curtze et al. [143] investigated SFE of austenitic stainless steels using the thermodynamic model in Eqns. (4.6) - (4.8) and found that the thermodynamic model overestimated SFEs compared to experimental results.

Table 4.3. Material properties of austenitic stainless steels used for stacking fault energy calculation and calculated Gibbs and stacking fault energies of the 100%, 90%, and 80% SS304L walls.

	100% SS304L	**90% SS304L**	**80% SS304L**	**Reference**
σ (J/m^2)	0.007			[145,146]
ρ (mol/m^2)	2.9x10^{-5}			[143,146]
$\Delta G^{\gamma\rightarrow\varepsilon}$(J/mol)	331.8	216.4	205.8	NA
γ_{SFE} (mJ/m^2)	33.6	26.8-28.8	26.2-27.2	NA

4.3.3. Effect of location on microstructure and mechanical properties

In the 80% and 90% SS304L walls, the ultimate tensile strength and ΔFN were found to be location-dependent, as shown in Figure 4.5b and Figure 4.5c, respectively. In the 90% SS304L wall, the amount of transformed martensite increased as the distance between the tested specimen and substrate increased, resulting in an increase in ultimate tensile strength

with height. The location-dependent martensitic phase transformation and mechanical properties are due to elemental composition heterogeneities during DED component fabrication. Table 2.1 shows the elemental composition of specimens from top and bottom of the 90% SS304L wall, in which the weight fraction of silicon, manganese, chromium, and nickel decreased as the sample height increased. In AM, the temperature of the molten pool increases with the distance from the substrate as heat accumulates with the addition of new layers [19,41,63,113]. Since volatile elements vaporize with increased temperature, these elements are depleted with increasing height. In SS304, the most volatile elements are manganese, chromium, and nickel [127]; thus, these elements were found to be depleted at the top compared to the bottom of the 90% SS304L wall, as shown in Table 2.1. As manganese, chromium, and nickel increase the SFE of austenite, the decrease in weight fraction of these elements reduces austenite stability and results in an increase in the volume fraction of transformed martensite and ultimate tensile strength with height.

In the 80% SS304L wall, the elemental composition also varied with height. There was a slight increase in weight fraction of silicon, manganese, chromium, and nickel from the bottom to the top of the wall, leading to a small decrease in transformed martensite content and ultimate tensile strength as the height increases (Figure 4.5c and Figure 4.5b). This trend, which is opposite of that seen in the 90% SS304L wall, is possibly due to insufficient melting of iron and SS304L powder during deposition. The trend of chemistry with height due to insufficient melting is beyond the scope of the present study, which aims to connect the chemistry to phase transformation kinetics and mechanical properties.

4.3.4. Martensitic phase transformation kinetics under uniaxial tension

In Figure 4.8, the ferrite number and true stress are plotted as a function of true strain for representative samples from all three walls and the annealed SS304L for loading/unloading uniaxial tension tests used in *in situ* measurement of martensite evolution. Due to Villari effect, the feritescope output increases during elastic unloading and decreases during elastic loading, as shown in Figure 4.8 [96,128]. The feritescope signal measured from the unloaded samples is taken to be the actual FN, as the Villari effect is minimized in the stress-free samples. The FN increased with plastic strain in the specimens from the 80% and 90% SS304L walls and the annealed SS304L substrate (Figure 4.8b-d), but remained almost constant in the specimens extracted from the 100% SS304L wall (Figure 4.8a). A significant amount of austenite transformed to martensite in the specimens from the 80% and 90% SS304L walls and the annealed SS304L substrate, while little to no martensite developed in samples extracted from the 100% SS304L wall, which agrees with results shown in Table 4.1.

The feritescope output, FN, can be converted to martensite volume fraction using Eqn. (4.1). The conversion factor, *k*, in Eqn. (4.1) was determined from neutron diffraction measurements on annealed SS304L. Figure 4.9 shows neutron diffraction patterns in an undeformed grip and a plastically deformed region of SS304L, in which the intensity of the (111), (200), (220), (311), and (222) fcc peaks (austenite) decreased and the intensity of the (211) and (111) bcc peaks (which include ferrite and martensite) increased with plastic deformation. The feritescope readings for all undeformed annealed SS304L specimens were below 3 FN, indicating the ferrite and any pre-exist martensite were below

5 vol.% in this material using the conversion factor described below. Therefore, the newly formed peaks from bcc phase in Figure 4.9 are due to strain-induced martensitic phase transformation. Here, we used the (311) peak from austenite and the (211) peak from martensite, which were better defined and less affected by texture compared to other peaks, to compute volume fractions of the two phases as a function of strain using Eqns. (4.2) - (4.4) and the parameters in Table 4.4. The average calculated martensite volume fraction, *c*, from patterns in the length and thickness directions were plotted as a function of the corrected feritescope reading, $S_{Fe,c}$, as shown in Figure 4.10, to find the conversion factor. Here, the unit of the feritescope reading is presented as vol.% ferrite, which represents the volume fraction of the ferromagnetic phases and can be converted to/from FN using a calibration curve [121]. From Figure 4.10, the conversion factor was found to be 1.8, which is in line with the literature on annealed and rolled austenitic stainless steels [96,98].

The strain-induced martensite content increases with plastic strain. In an early study of strain-induced martensitic transformation performed by Cottrell [147], phase transformation was observed in carbon steel in between 250 ^{o}C and 425 ^{o}C, and the volume fraction of martensite was found to be linearly proportional to plastic strain. However, in the present materials, the evolution martensite volume fraction with respect to plastic strain was found to have a sigmoidal shape, which is similar to the behavior seen in other austenitic stainless steels reported in the literature [45,48,49,96,122,148]. Santacreu et al. [148] proposed a phase transformation kinetics equation to describe the sigmoidal shape of strain-induced martensite content evolution as a function of plastic strain in austenitic stainless steels:

$$\frac{c}{c_{max}} = 1\text{-}\exp\{\text{-}[D(\bar{\varepsilon}_P)]^n\} \tag{4.9}$$

where c_{max} is the saturation value of the strain-induced martensite volume fraction, n and D are material parameters, and $\bar{\varepsilon}_P$ is the equivalent plastic strain.

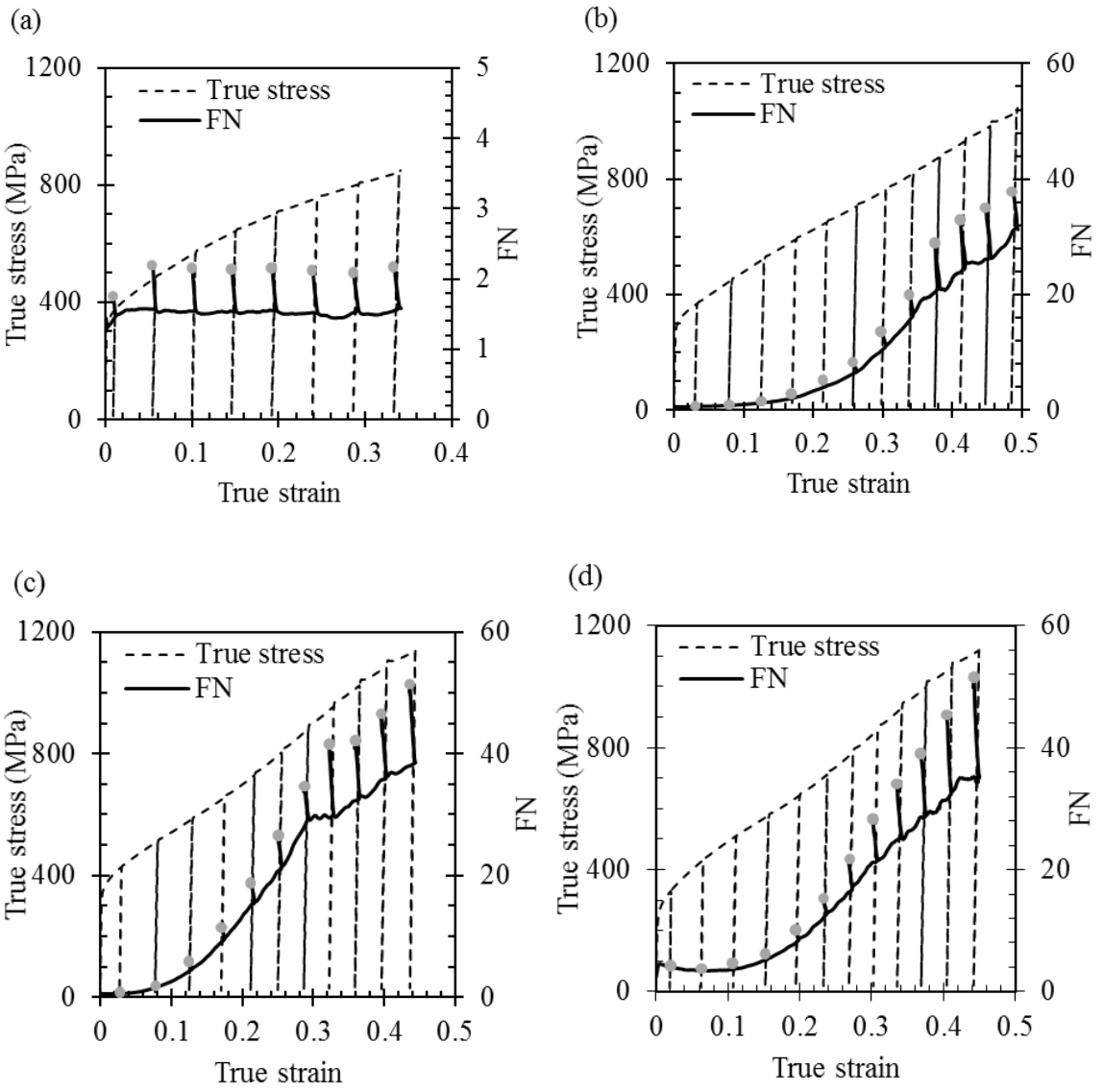

Figure 4.8. True stress and FN as a function of true strain in representative samples from (a) the top of the 100% SS304L wall, (b) the top of the 90% SS304L wall, (c) the top of the 80% SS304L wall, and (d) the annealed SS304L substrate. Gray symbols represent actual FN measured in stress-free conditions.

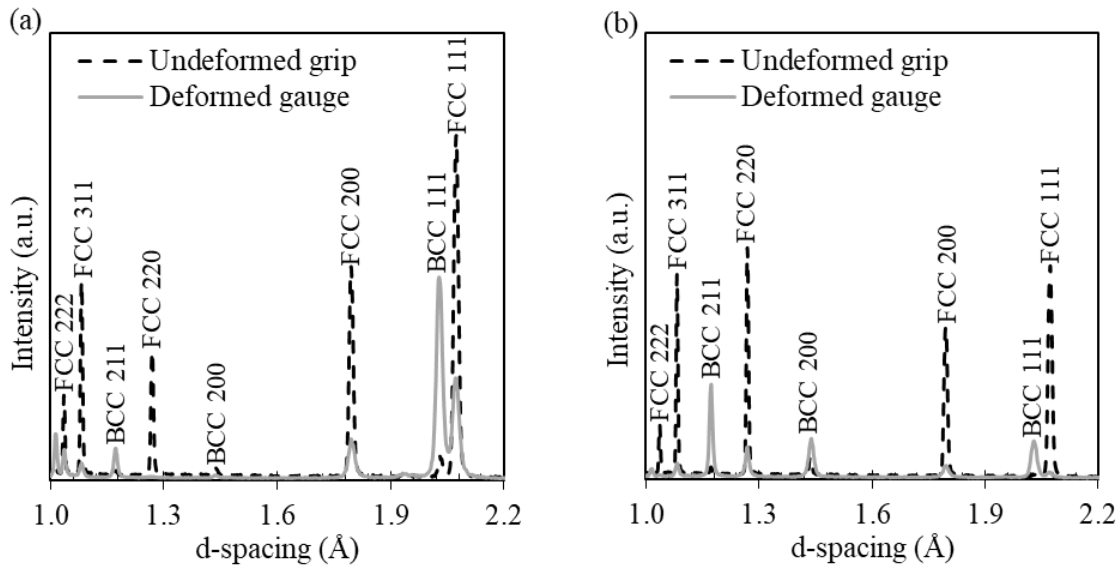

Figure 4.9. Neutron diffraction patterns for a specimen from the annealed SS304L substrate in the (a) length direction (Bank 1), and (b) thickness direction (Bank 2), showing the contrast between signals in undeformed and deformed (66% engineering strain under uniaxial tension) regions.

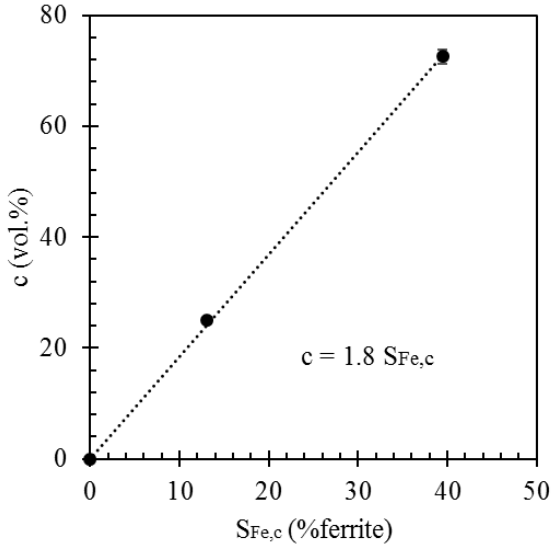

Figure 4.10. Martensite content, *c*, measured by neutron diffraction as a function of the corrected feritescope reading, $S_{Fe,c}$, showing a conversion factor, *k*, from volume fraction of ferrite to volume fraction of martensite of 1.8.

As there is no clear anisotropy in yield strength, ultimate tensile strength, or ductility in the walls from Table 4.1, the properties are assumed be isotropic under uniaxial tension and $\bar{\varepsilon}_P$ is taken to be $\bar{\varepsilon}_{vM}^P$, the isotropic von Mises equivalent plastic strain. If *D* is assumed to be a variable that depends only on stress state [50], then it is a constant in our study as all specimens from the 80% and 90% SS304L walls were loaded under uniaxial tension. The material parameters, c_{max}, *n*, and *D* can be determined by fitting the experimental data on the martensite content as a function of $\bar{\varepsilon}_{vM}^P$ as shown in Figure 4.11 for the 80% and 90% SS304L walls. Table 4.5 gives the calibrated values for c_{max}, *n*, and *D*, and the resulting transformation kinetics plots are shown as lines in Figure 4.11.

Table 4.4. Parameters for martensite content calculation using the internal standard method, where f is the atomic scattering factor of an iron atom.

	M	$\|\mathbf{F}\|^2$
(311), fcc	24	$16f^2$
(211), bcc	12	$4f^2$

Table 4.5. Calibrated parameters for the martensitic transformation kinetics equation.

	Distance from the bottom of the wall (mm)	$\mathbf{c_{max}}$ **(vol.%)**	**D**	**n**
90% SS304L	15	46	3.4	3.9
	50	77	3.4	2.5
80% SS304L	13	92	3.4	2.2
	40	79	3.4	2.6
	62	60	3.4	3.6

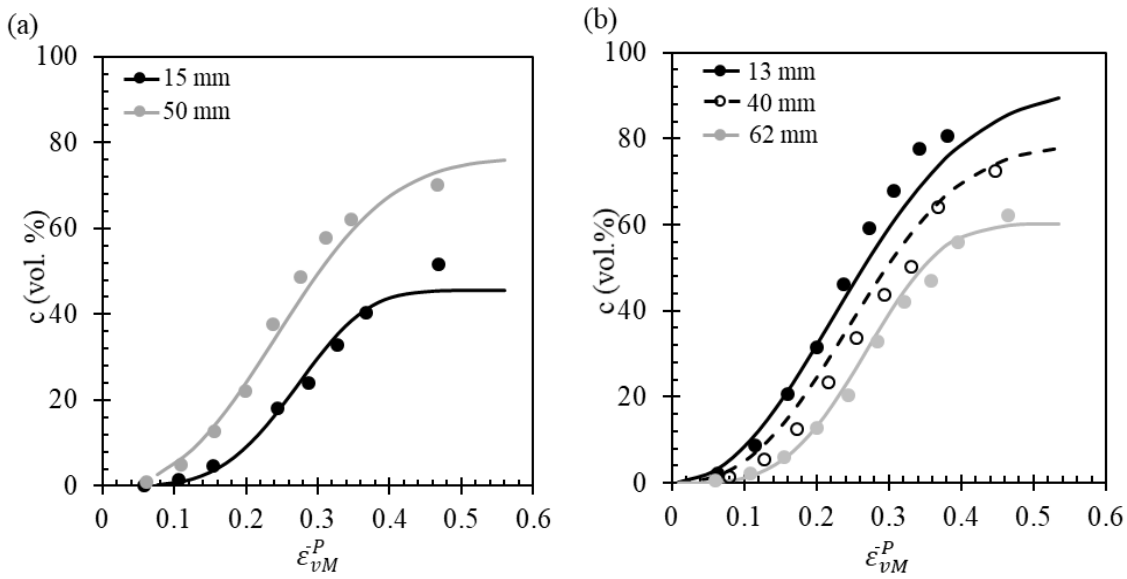

Figure 4.11. Martensite volume fraction, *c*, as a function of von Mises equivalent plastic strain, $\bar{\varepsilon}^P_{vM}$, in longitudinal samples at different locations from the (a) 90%, and (b) 80% SS304L walls. Symbols correspond to experimental data and lines correspond to calibrated transformation kinetics equations.

As shown in Figure 4.11, in the 90% SS304L wall, the transformation kinetics curve has a higher slope, which represents a higher rate of martensitic phase transformation with respect to plastic strain, in the specimen from the top of the wall than the specimen from the bottom, which agrees with the increase in M_{d30} temperature, or decrease in austenite stability, with height shown in Table 2.1. In addition, the saturation value of the transformation kinetics curve increases with the height. In the 80% SS304L wall, the transformation kinetics equation curve has a higher slope for the specimen from the bottom of the wall compared to specimens from the top, which agrees with the decrease in M_{d30} temperature, or increase in austenite stability, with height shown in Table 2.1. The saturation value of the transformation kinetic curve also decreases with the height.

The data were further analyzed to link the chemistry, in terms of the M_{d30} temperature, to the transformation kinetics equation. The parameter n is related to the rate of increase in martensite for a given increment in plastic strain; namely, a small n is indicative of a high rate of phase transformation with plastic strain (Eqn. 4.9). The parameter c_{max} describes the saturation value of martensite in the given material, or how much martensite can be formed with an unlimited amount of plastic strain. Figure 4.12 shows n and c_{max} versus M_{d30}, using data in Table 2.1 and Table 4.5 from longitudinal samples at different locations in the 80% and 90% SS304L walls. There appears to be linear relationships between n and M_{d30} temperature, and c_{max} and M_{d30} temperature. Therefore, we can describe the parameters for the austenite-to-martensite phase transformation kinetics in additively manufactured stainless steel as a function of chemistry using the below two empirical equations:

$$n = -0.12M_{d30} + 7.2 \tag{4.10}$$

$$c_{max} = 3.2M_{d30} - 38.8 \tag{4.11}$$

where M_{d30} is given in ^{o}C.

These relationships show that n decreases and c_{max} increases with increasing M_{d30} temperature, or decreasing austenite stability. The decrease in n with increasing M_{d30} is indicative of a higher rate of phase transformation with decreasing austenite stability, meaning for the same plastic strain, more austenite will transform to martensite for a material with a lower austenite stability. The increase in c_{max} with increase in M_{d30} indicates that the lower the austenite stability, the higher the potential for phase transformation. Both of these trends are physically consistent with the fact that more austenite transforms to martensite when the austenite is metastable versus stable.

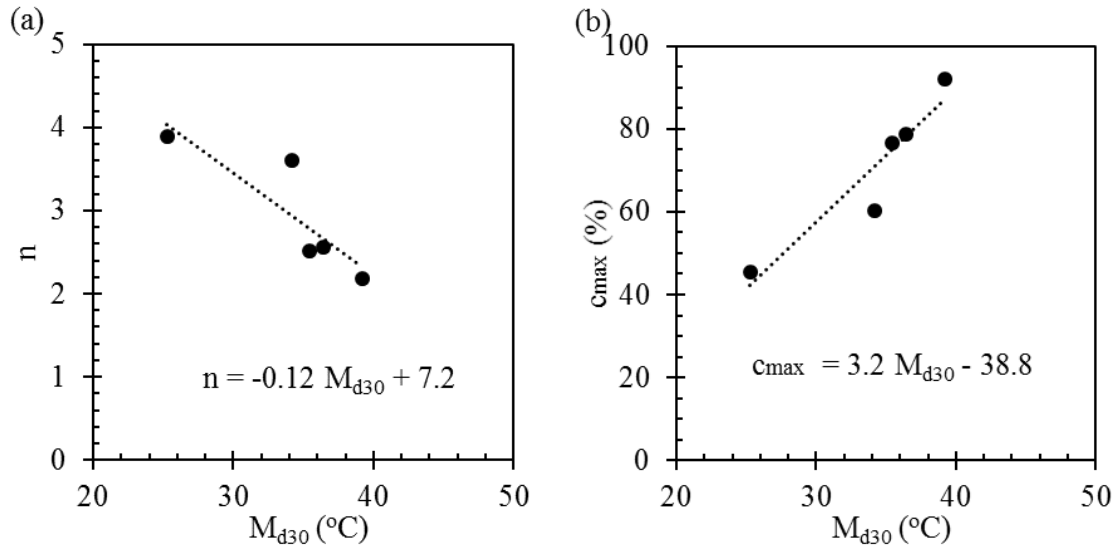

Figure 4.12. Transformation kinetics parameters (a) *n*, and (b) c_{max} as a function of M_{d30} temperature in longitudinal samples from different locations in the 80% and 90% SS304L walls. The fitted lines were used to quantitatively link *n* and c_{max} to the M_{d30} temperature.

4.4. Summary and conclusions

The 304L stainless steel walls with different initial powder chemistry were built by DED to study the effect of chemistry, namely powder chemistry and local elemental variations due to vaporization during processing, on the heterogeneous strain-induced martensitic phase transformation kinetics and tensile mechanical properties. The primary findings of this work are as follows:

- By mixing pre-alloyed SS304L powder (atomized in nitrogen) with Fe powder, the weight fraction of elements that increase the stacking fault energy of austenite was successfully decreased, which activated strain-induced austenite-to-martensite phase transformation. The occurrence of phase transformation in specimens from 80% and 90% SS304L walls improved their ultimate tensile strengths and elongations to failure

over those in the 100% SS304L wall. The microstructural phase transformation results in an increased strain-hardening rate and stabilization of the neck, resulting in increased ductility over samples with no phase transformation.

- The chemical composition in components made by AM depends on thermal history, and therefore, location. During AM, as the distance from the substrate increases, and heat builds up in the build as layers are added, the temperature of the molten pool increases; thus, the concentration of volatile elements in the molten pool decreases as those elements are preferentially vaporized. In SS304L, the concentrations of elements that increase the stacking fault energy of austenite, chromium, manganese, and nickel decreased with height in the 90% SS304L wall. This resulted in a decrease in austenite stability and an increase in martensitic phase transformation with height, which resulted in an increase in ultimate tensile strength with height.
- The martensitic phase transformation kinetics depend strongly on chemical composition. As the weight fraction of elements that increase the stacking fault energy of austenite decreased, the stability of austenite decreased and the rate of martensite formation with respect to plastic strain increased. The saturation value of the strain-induced martensite volume fraction also increased as the weight fraction of elements that increase the stacking fault energy of austenite, decreased. We present a chemistry-dependent phase transformation kinetics equation that describe the rate, with respect to plastic strain, and saturation value of phase transformation in austenitic stainless steels fabricated via AM.
- In additive manufacturing, it is necessary to understand the initial powder chemistry as well as spatial chemical composition variations due to preferential vaporization during

deposition. While chemical variation is well-known in welding, it is particularly important to recognize chemical heterogeneity in additive manufacturing as the number of passes in AM is orders of magnitude higher than that encountered in welding; therefore, chemistry may change significantly within a single build, impacting the microstructure and properties of deposited materials. As shown here, in austenitic stainless steels, the elemental composition influences the stability of austenite, which affects the deformation mechanics, namely the strain-induced martensitic phase transformation, which in turn dictates the macroscopic mechanical properties of the material.

Acknowledgments

The authors gratefully acknowledge the financial support provided by the National Science Foundation through award number CMMI-1402978. Any opinions, findings, and conclusions or recommendations in the materials are those of the authors and do not necessarily reflect the views of the Nation Science Foundation. We acknowledge Dr. Todd Palmer and Mr. Jay Tressler for component fabrication and Mr. Griffin Jones for the X-ray CT scans at the Center for Innovation Materials Processing through Direct Digital Deposition (CIMP-3D). We acknowledge Dr. Dong Ma and Mr. Matthew Frost of ORNL for neutron diffraction data collection and technical support at the VULCAN beamline. In addition, AMB acknowledges funding from the Oak Ridge Associated Universities Ralph E. Powe Junior Faculty Enhancement Award.

Chapter 5

Effect of stress state and texture on martensitic phase transformation kinetics

5.1. Introduction

The volume fraction of strain-induced martensite as a function of plastic strain depends on temperature, chemical composition, strain, strain rate, and stress state [46,48,49]. The chemical composition dictates the stacking fault energy (SFE) of austenite, which in turn influences the propensity for strain-induced martensitic transformation kinetics [66]. As discussed in Chapters 3 and 4, the austenite in walls made from 100 vol.% SS304L powder that was gas atomized in nitrogen was stabilized; thus, the nitrogen introduced during powder processing precluded strain-induced martensitic transformation in these builds. By mixing pre-alloyed SS304L powder with iron powder, the weight fraction of elements that increase the stacking fault energy of austenite, decreased, resulting in the activation of strain-induced martensitic transformation.

During additive manufacturing of stainless steel, columnar austenite grains grow along the maximum thermal gradient during deposition, or the build direction, resulting in texture in the additively manufactured components [44,78]. Texture in austenitic stainless steels may impact strain-induced martensitic transformation by influencing the

---

Reproduced from: Z. Wang and A. M. Beese, "Effect of stress state and texture on martensitic phase transformation kinetics of additively manufactured stainelss steel," *Submitted for publication* [149].

mechanical driving force for phase transformation [79–82]. Creuziger et al. [79] predicted the driving force for textured TRIP steels under a number of loading conditions, concluding that steels with brass and copper textures had lower driving forces and therefore required higher applied stresses for phase transformation, than steels with cube texture, under all the stress states studied. Similarly, Knijf et al. [82] predicted the driving force for martensitic transformation in a low carbon steel subjected to uniaxial tension, and showed that materials with cube and rotated Goss textures had higher driving forces for phase transformation than those with brass and copper textures. Hilkhuijsen et al.[80,81] investigated martensitic transformation in untextured and highly textured stainless steels loaded under uniaxial tension. Their results showed the evolution of martensite content with respect to plastic strain was independent of orientation in untextured specimens, but varied significantly between textured specimens with loading axes along the rolling direction versus the transverse direction.

Stress state also impacts strain-induced martensitic transformation in steels with retained austenite, but the experimental results reported in the literature are inconsistent. Cina [150] found that more martensite was formed under uniaxial tension than uniaxial compression at the same plastic strain in steels containing 18-25% chromium and 8-12% nickel. Powell et al. [69] found that for the same equivalent plastic strain, more martensite was formed under tension than torsion or compression in 301 and 304 stainless steels. Hecker et al. [72] and Murr et al. [73] observed that more than twice as much martensite was formed under equi-biaxial tension than uniaxial tension at the same maximum principal strain in annealed 304 stainless steel. Conversely, Kosarchuk et al. [151] found that a higher amount of martensite was formed under uniaxial tension than equi-biaxial

tension at the same equivalent plastic strain in steels containing 16% chromium and 10% nickel. Okutani et al. [152] reported that the amount of martensite was higher under uniaxial compression than that under uniaxial tension at the same plastic strain in 304 stainless steel. Conversely, Iwamoto et al. [70] found that more martensite was formed under uniaxial compression than uniaxial tension at low plastic strains, but that this trend was reversed at higher plastic strains (i.e., above 20-40%) in annealed 304 stainless steel. Yu et al. [153] observed that the rate of martensitic transformation with respect to equivalent plastic strain was highest under plane strain tension, followed by equi-biaxial tension, and lowest under uniaxial tension in cold rolled TRIP 600 steel. Beese and Mohr [50] reported that in temper-rolled 301LN stainless steel, the rate of martensitic transformation with respect to equivalent plastic strain from high to low was: uniaxial tension, plane strain tension, equi-biaxial tension, and uniaxial compression.

As experimental investigations on the effect of stress state on martensitic transformation are contradictory, the proposed equations to describe the transformation kinetics are also diverse. Olson and Cohen [49] proposed a transformation kinetics equation that captured the effect of plastic strain and temperature on annealed 304 stainless steel under uniaxial tension [46]. Stringfellow et al. [48] expanded this equation by adding the effect of stress triaxiality, proposing that the rate of martensitic transformation increases with stress triaxiality. Their equation was based on the experimental uniaxial tension and compression data measured by Young [154]. Kosarchuk and Lebedev [151,155] studied martensitic transformation kinetics in austenitic stainless steel 18-10 subjected to uniaxial tension, uniaxial compression, torsion, and equi-biaxial tension. They concluded from the experimental results that martensitic transformation was not only affected by stress

triaxiality, and suggested the phase transformation also depended on the Lode angle parameter. Their results qualitatively showed that martensite content at a fixed equivalent plastic strain increased with stress triaxiality and decreased with Lode angle parameter. Beese and Mohr [50] proposed a martensitic transformation equation for austenitic stainless steel that fully incorporated the effect of stress state, by including the dependence on stress triaxiality and Lode angle parameter. Their calibrated equation showed that the rate of transformation with respect to plastic strain increased with stress triaxiality and Lode angle parameter.

The strain-induced martensitic phase transformation kinetics in conventionally processed austenitic stainless steels with nearly equiaxed grains under various stress states have been investigated extensively [50,69,70,72,73,150–156]. However, only one paper has reported the transformation kinetics in additively manufactured austenitic stainless steels, with the study limited to uniaxial tension [124]. The aim of the present study was to investigate the effect of stress state on strain-induced martensitic phase transformation in SS304L, with two different chemistries, deposited by DED AM. The evolution of martensite volume fraction with plastic deformation was quantified using *in situ* magnetic permeability and neutron diffraction measurements during mechanical tests under uniaxial tension, pure shear, and uniaxial compression. A chemistry-, stress state-, and texture-dependent martensitic phase transformation kinetics equation describing martensite volume fraction as a function of equivalent plastic strain, is proposed and calibrated for SS304L made by AM. This transformation kinetics equation can be used to describe the stress state-dependent martensitic transformation in textured austenitic stainless steels.

5.2. Experimental procedures

5.2.1. Uniaxial tension

Longitudinal and transverse uniaxial tension specimens, as described in Chapter 4, were extracted from the 80% and 90% SS304L walls using EDM. As the spatial chemical variation, due to preferential elemental vaporization, resulted in location-dependent martensitic transformation and mechanical properties. Therefore, to eliminate the impact of spatial chemical variation in this study, samples were extracted such that the gauge centers of all specimens were at the same height, about 40 mm away from the bottom of each wall.

Monotonic and periodic loading/unloading uniaxial tension tests with *in situ* feritescope measurements were performed and analyzed, as described in Chapter 4. The feritescope reading was converted to the volume fraction of martensite using Eqn. (4.1). The conversion factor, *k*, which was found to be 1.8 in Chapter 4, was validated in Section 5.3.

5.2.2. Plane strain tension and pure shear

Plasticity specimens with a reduced thickness gauge section as shown in Figure 5.1 [157] were used to measure the mechanical behavior under plane strain tension and pure shear. The gauge length along the transverse (T) direction in the specimen was 10 times larger than that in the longitudinal (L) direction, resulting in a nearly zero strain along the longitudinal direction, or a plane strain condition. Longitudinal and transverse plasticity

specimens were extracted using wire EDM from the 80% and 90% SS304L walls such that the gauge centers were 40 mm from the bottom of the walls.

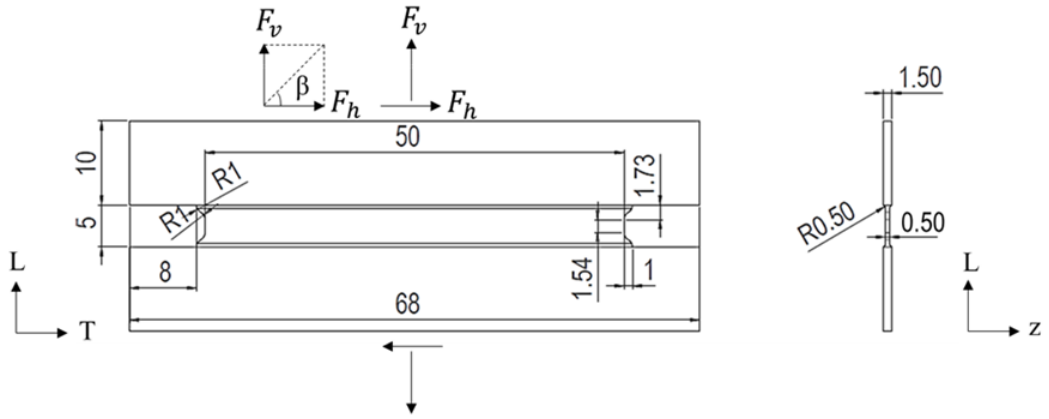

Figure 5.1. Geometry of a multiaxial plasticity specimen (unit: mm) adapted from [157], where F_v and F_h represent the applied force in vertical and horizontal directions, and β, the biaxial loading angle, is used to determine the ratio of the vertical to horizontal forces.

Multiaxial loading tests were performed using a custom-built hydraulic test frame with two actuators (MTS Systems Corp.) shown schematically in Figure 5.2. In this system, the vertical force is measured by two 100 kN load cells and the horizontal force by a 50 kN load cell. In plane strain tension tests, which were used only for feritescope calibration, displacement control was used to apply a vertical strain rate of 3.3 x 10^{-4} /s, with no horizontal displacement. In pure shear tests, displacement control was used to apply a horizontal strain rate of 1.3 x 10^{-3} /s, while the vertical force was set to zero. The evolution of martensite content with respect to plastic strain in the plasticity specimens was measured using a feritescope. In periodic loading/unloading tests with *in situ* measurements, the samples under pure shear tests were loaded to 6% horizontal engineering strain, unloaded

to zero force for magnetic permeability measurements, and reloaded to an additional 6% horizontal engineering strain before repeating the unloading and measurement steps. A 25 pixels subset and a 6 pixel step size were used, resulting in a 67 pixels or 0.8 mm virtual strain gauge size [101]. The vertical and horizontal strains were measured using 3 mm long virtual vertical and horizontal extensometers.

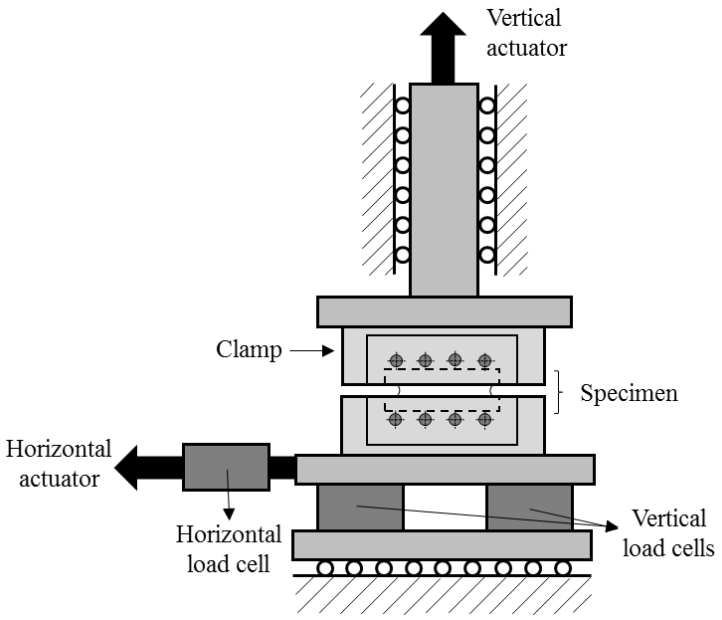

Figure 5.2. Schematic of the dual actuator hydraulic test frame for multiaxial testing.

5.2.3. Uniaxial compression

Cylindrical specimens measuring 8 mm in diameter and 16 mm long were used to characterize the compressive behavior of the additively manufactured walls. Both longitudinal and transverse specimens were extracted, using wire EDM, from a height of 40 mm from the bottom of the wall. Monotonic uniaxial compression tests were conducted at a strain rate of 1.5×10^{-5}/s with *in situ* neutron diffraction on the VULCAN instrument

at Oak Ridge National Laboratory's Spallation Neutron Source [129–131]. The VULCAN instrument has two detector banks that collected diffraction patterns from grains whose *hkl*-specific lattice planes were perpendicular to the axial and normal directions, as schematically shown in Figure 5.3. The d-spacings and integrated intensities of *hkl*-specific lattice planes from austenite (γ, fcc) and strain-induced martensite (α', bcc) were measured to computed the volume fractions of austenite and martensite using the internal standard method introduced in Chapter 4.

The collected diffraction patterns from a transverse compression specimen from the 90% SS304L wall were also analyzed with Rietveld refinement using the General Structural Analysis Software (GSAS) to determine the evolution of phase fractions [158,159]. The volume fraction of martensite computed by Rietveld refinement was used to validate the phase fraction determined by the internal standard method.

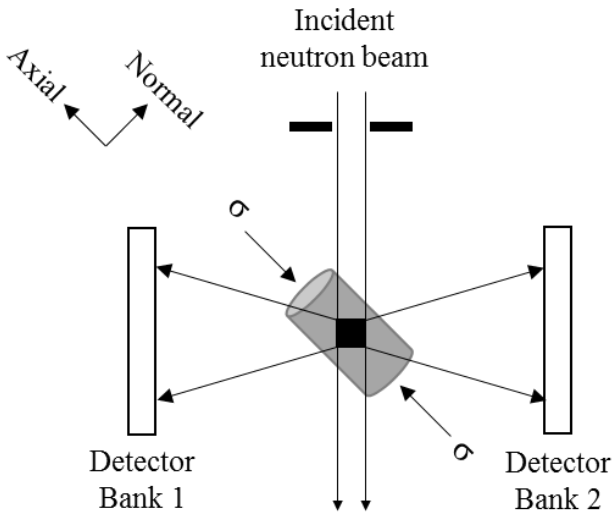

Figure 5.3. Schematic of compression test with *in situ* neutron diffraction, in which diffraction signals from axial and normal directions were collected.

5.2.4. Magnetic saturation

The most accurate method for quantifying the volume fraction of a ferromagnetic phase in a sample is magnetic saturation measurements, as this technique is not affected by the size, texture, surface preparation, or elastic strains within the sample [96]. In this method, a ferromagnetic specimen is placed in a magnetic field and the magnetic dipoles align parallel to the applied field, resulting in the sample becoming magnetized. The magnetic induction of the specimen increases with the strength of the applied magnetic field until it reaches a saturation value. As the magnetic saturation induction of α' martensite is 154 emu/g [160], the volume fraction of ferromagnetic material in the samples equals the magnetic saturation induction of the sample, normalized by the weight of the sample, and divided by 154 emu/g. In order to verify the martensite content determined by magnetic permeability measurements, magnetic saturation measurements were made using a sigmameter (SETARAM Sigmameter D6025) on two plasticity specimens, one that was plastically deformed under plane strain tension, and the other under pure shear. Martensite content was obtained by subtracting the volume fraction of ferrite, which was under 2% in each specimen, from the computed volume fraction of the ferromagnetic material.

5.3. Results

In order to verify the magnetic permeability measurements using the feritescope, the martensite volume fraction measured by the feritescope was compared to that measured by the sigmameter as shown in Figure 5.4. The 1:1 ratio of these measurements indicates that the thickness-corrected magnetic permeability measurements, and $k = 1.8$ in Eqn. (4.1) are accurate.

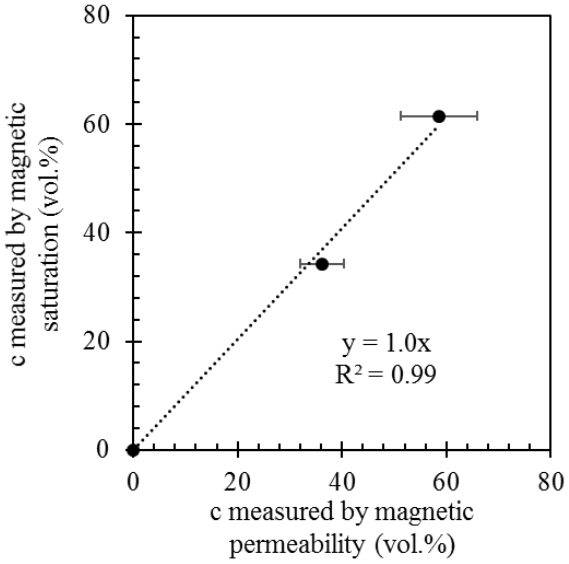

Figure 5.4. Martensite volume fraction, *c*, measured by magnetic saturation versus *c* measured by magnetic permeability.

In uniaxial compression tests, the evolution of martensite content with respect to plastic strain was computed using the internal standard method from neutron diffraction (Eqns. (4.2) - (4.4)). Figure 5.5 shows neutron diffraction patterns from a transverse cylindrical specimen from the 90% SS304L wall before and after 27% plastic deformation. The volume fraction of ferromagnetic material in the as-built sample was measured to be under below 2%, as demonstrated by the low intensities of bcc peaks in the diffraction pattern before plastic deformation in Figure 5.5. The increase in bcc peak intensities after plastic deformation is the result of newly formed strain-induced martensite. The intensities of the fcc austenite peaks decreased and the intensities of the bcc martensite peaks increased, which is indicative of phase transformation. To quantify the amount of martensite formed, the (220) and (200) peaks from fcc austenite, and (211) and (200) peaks from bcc martensite were used, per ASTM E975 [161]. As a validation of this approach, the

martensite content evolution in a 90% SS304L transverse compression specimen computed by Rietveld refinement and the internal standard method are compared in Figure 5.6. The good agreement between the two curves indicates that the volume fraction of martensite computed using the internal standard methods is accurate.

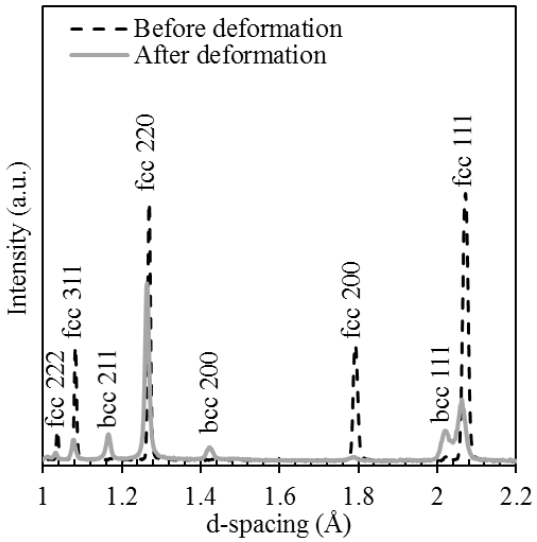

Figure 5.5. Neutron diffraction patterns, along the loading direction, of a transverse specimen from the 90% SS304L wall before and after uniaxial compression to 27% engineering strain.

Figure 5.7 shows the volume fraction of martensite as a function of plastic strain in longitudinal and transverse specimens from the 90% SS304L wall under uniaxial tension and uniaxial compression, indicating that there is no notable anisotropy in the martensitic transformation kinetics in this material.

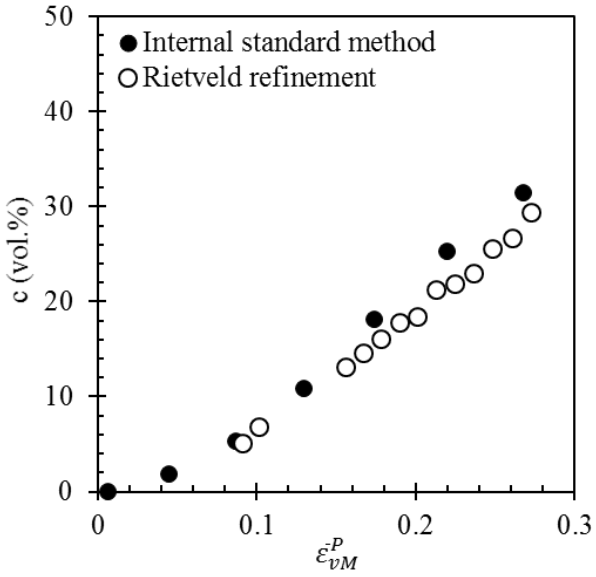

Figure 5.6. Martensite volume fraction, *c*, as a function of von Mises equivalent plastic strain, $\bar{\varepsilon}^P_{vM}$, determined by the internal standard method and Rietveld refinement in a transverse compression specimen from the 90% SS304L.

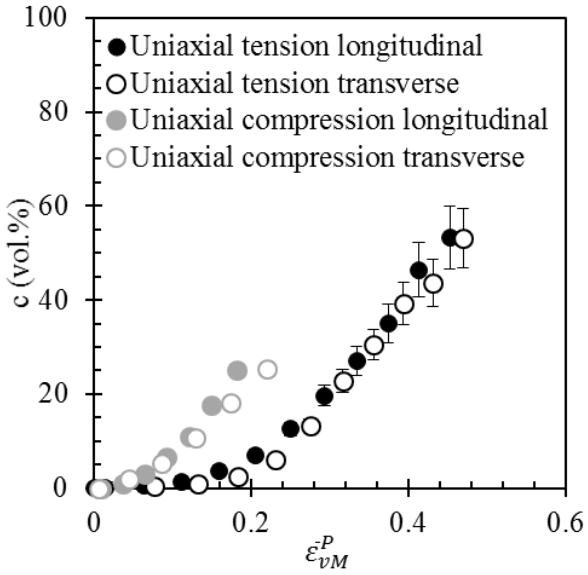

Figure 5.7. Martensite volume fraction, *c*, as a function of von Mises equivalent plastic strain, $\bar{\varepsilon}^P_{vM}$, in longitudinal and transverse specimens from the 90% SS304L wall under uniaxial tension and uniaxial compression.

Martensite evolution curves of representative longitudinal specimens from the two walls under uniaxial tension, pure shear, and uniaxial compression are given in Figure 5.8. Due to the isotropic martensitic transformation kinetics, the compression data from transverse specimens are reported and assumed to be the same as those in the longitudinal specimens. Plasticity data for plane strain tension tests are not included in the study, because their data were polluted by lack-of-fusion pores (about 0.2 vol.% from X-ray CT results), whose long axes were oriented perpendicular to the build direction. Therefore, tension in the build direction was not performed as these pores would limit ductility in that direction, as discussed in Chapter 4. Additionally, in tests in which tension was applied in the longitudinal direction, the accompanying tension in the build direction that results from the plane strain constraint, led to the lack of fusion pores opening up and relieving the plane stress condition during testing.

As shown in Figure 5.8, in a single wall, the slope of the martensitic transformation kinetics curve, or the rate of martensitic transformation with respect to plastic strain, is the highest under uniaxial compression, followed by uniaxial tension, and lowest under pure shear. The finding of a higher rate of transformation under compression than tension contradicts most of the data on phase transformation in texture-free materials, and the reasons for this deviation are described in Section 5.4.

Under the same stress state, the slopes and saturation values of the transformation kinetics curves are higher in specimens from the 80% SS304L wall than those from the 90% SS304L wall, as the 80% SS304L wall with higher iron content had lower austenite stability, as discussed in Chapter 4.

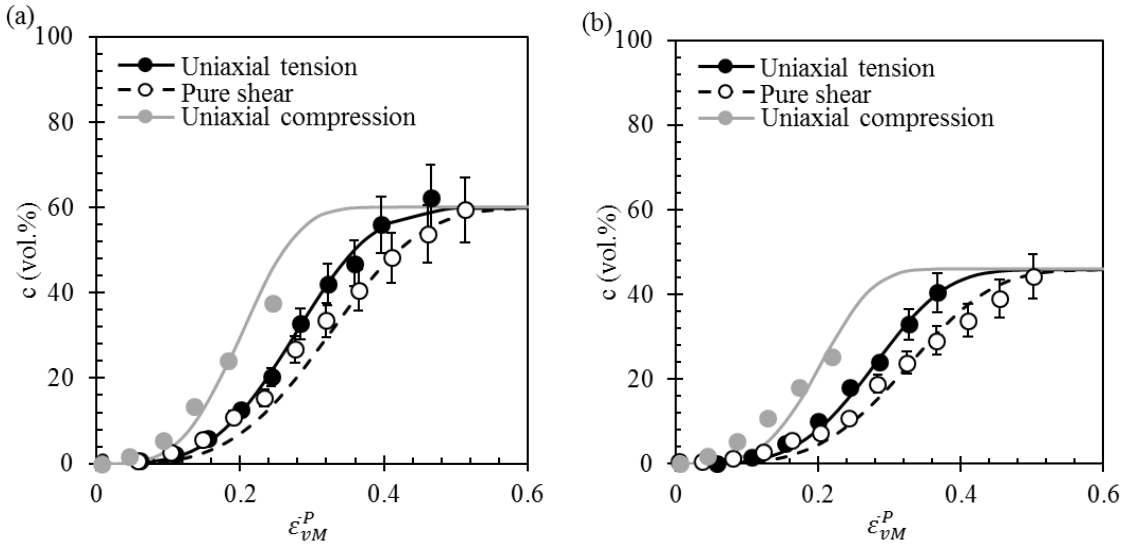

Figure 5.8. Martensite volume fraction, *c*, as a function of von Mises equivalent plastic strain, $\bar{\varepsilon}^P_{vM}$, in specimens from the (a) 80 % SS304L wall and (b) 90% SS304L wall under uniaxial tension, pure shear, and uniaxial compression. Symbols correspond to experimental data and lines correspond to calibrated transformation kinetics equations.

5.4. Discussion

5.4.1. Effect of stress state on martensitic transformation kinetics

In additive manufacturing, due to thermal gradients in the build direction, columnar grains tend to grow along the vertical build direction, which may result in a textured component [44,78]. As shown in the inverse pole figures of a transverse compression specimen in the present study in Figure 5.9, the predominant texture of the walls studied here was {111} <1$\bar{1}$0>, in which <1$\bar{1}$0> was parallel to the transverse (build) direction

within the wall, and <111> was parallel to the longitudinal direction within the wall. It has been shown previously that texture in austenitic stainless steels has a significant effect on the austenite-to-martensite transformation [79–81].

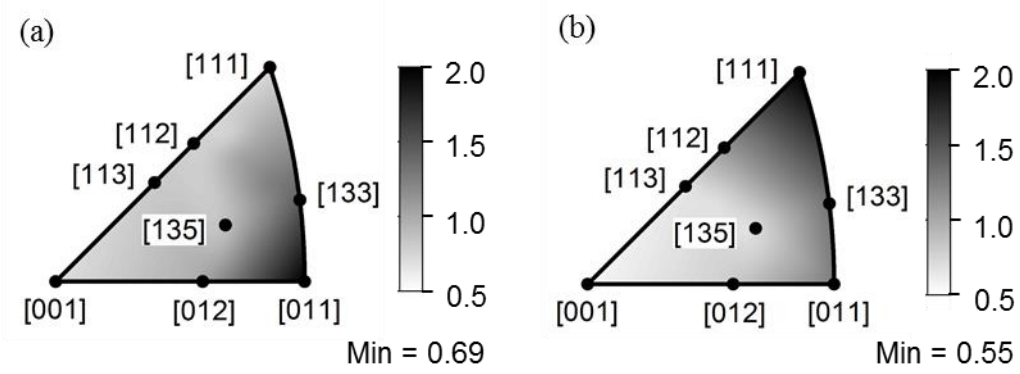

Figure 5.9. Inverse pole figures, determined by neutron diffraction, of a transverse compression specimen from the 90% SS304L wall with plane normals parallel to the (a) loading, or transverse, direction, and (b) normal, or longitudinal, direction.

During the austenite-to-martensite transformation, there are 24 variants of martensite that can be formed [162]. The driving force of strain-induced martensitic transformation for the i^{th} variant, w_i, can be calculated by [79–81]:

$$w_i = \boldsymbol{\sigma_{cl}} : \left[\frac{\mathbf{1}}{\mathbf{2}}(\boldsymbol{s_i} \otimes \boldsymbol{n_i} + \boldsymbol{n_i} \otimes \boldsymbol{s_i})\right] \tag{5.1}$$

where $\boldsymbol{\sigma_{cl}}$ is the applied stress tensor in the coordinate system of an austenite unit cell, $\boldsymbol{n_i}$ is the habit plane normal, and $\boldsymbol{s_i}$ is the shear direction of the i^{th} variant. The vectors, $\boldsymbol{n_i}$ and $\boldsymbol{s_i}$, correspond to each variant, and depend on the lattice parameters of austenite and martensite [162]. Through neutron diffraction, the lattice parameter for fcc austenite was determined to be 0.287 nm, and that for bcc martensite, 0.358 nm. In order to transform

the applied stress tensor into the austenite coordinate system (or that of the textured component), the following equation is used:

$$\boldsymbol{\sigma_{cl}} = \boldsymbol{R}\,\boldsymbol{\sigma}\,\boldsymbol{R^T} \tag{5.2}$$

where $\boldsymbol{\sigma}$ is the stress tensor with respect to the coordinate system of specimen; and $\boldsymbol{R}$ is the rotation matrix given as:

$$\boldsymbol{R} = \begin{bmatrix} \cos\varphi_1 & sin\varphi_1 & 0 \\ -sin\varphi_1 & cos\varphi_1 & 0 \\ 0 & 0 & 1 \end{bmatrix} \begin{bmatrix} 1 & 1 & 0 \\ 0 & cos\Phi & sin\Phi \\ 0 & -sin\Phi & cos\Phi \end{bmatrix} \begin{bmatrix} \cos\varphi_2 & sin\varphi_2 & 0 \\ -sin\varphi_2 & cos\varphi_2 & 0 \\ 0 & 0 & 1 \end{bmatrix} \tag{5.3}$$

where φ_1, Φ, and φ_2 are Euler angles.

For a given stress state, the variant with the highest driving force has the highest probability of transformation [79–81]. Therefore, the driving force for phase transformation in austenite grains, *W*, as a function of the three Euler angles, is:

$$W(\varphi_1,\Phi,\varphi_2) = \max(w_i(\boldsymbol{\sigma},\varphi_1,\Phi,\varphi_2)) \tag{5.4}$$

To compare the driving forces under uniaxial tension, pure shear, and uniaxial compression, normalized stress states were defined such that the unitless von Mises equivalent stress of each stress state was 1. The resulting stress tensors for uniaxial tension, $\boldsymbol{\sigma_{UT}}$, pure shear, $\boldsymbol{\sigma_{shear}}$, and uniaxial compression, $\boldsymbol{\sigma_{UC}}$, are:

$$\boldsymbol{\sigma_{UT}} = \begin{bmatrix} 1 & 0 & 0 \\ 0 & 0 & 0 \\ 0 & 0 & 0 \end{bmatrix};\ \boldsymbol{\sigma_{shear}} = \begin{bmatrix} 0 & \frac{1}{\sqrt{3}} & 0 \\ \frac{1}{\sqrt{3}} & 0 & 0 \\ 0 & 0 & 0 \end{bmatrix};\ \boldsymbol{\sigma_{UC}} = \begin{bmatrix} -1 & 0 & 0 \\ 0 & 0 & 0 \\ 0 & 0 & 0 \end{bmatrix} \tag{5.5}$$

Using Eqns. (5.1) – (5.5), the unitless driving forces for martensitic transformation under the three stress states are plotted as a function of Euler angle (with φ_2 =45°) in Figure 5.10. The initial texture for transverse specimens, using the notation of {normal direction} <loading direction>, was {111} <1$\bar{1}$0>, corresponding to (0°, 55°, 45°). The initial texture for longitudinal specimens was {1$\bar{1}$0} <111>, corresponding to (35°, 90°, 45°). The driving

forces for specimens with initial textures of (0°, 55°, 45°) and (35°, 90°, 45°) under uniaxial tension, pure shear, and uniaxial compression are given in Table 5.1. As shown in Table 5.1, under the same stress state, the driving forces for martensitic transformation are close for longitudinal and transverse specimens. In the same orientation, the driving force for martensitic transformation from high to low is: uniaxial compression, uniaxial tension, and pure shear. For the specimens included in Figure 5.8, the unitless driving forces for uniaxial compression, uniaxial tension, and pure shear are 0.11, 0.06, and 0.01, respectively. Therefore, in the specimens studied here, the transformation under uniaxial compression was aided by texture, resulting in a higher rate of transformation in compression than tension as shown in Figure 5.8.

Table 5.1. Driving force for martensitic transformation for the stress states studied.

		Driving force
Uniaxial tension	Longitudinal	0.06
	Transverse	0.01
Pure shear	-	0.01
Uniaxial compression	Longitudinal	0.13
	Transverse	0.11

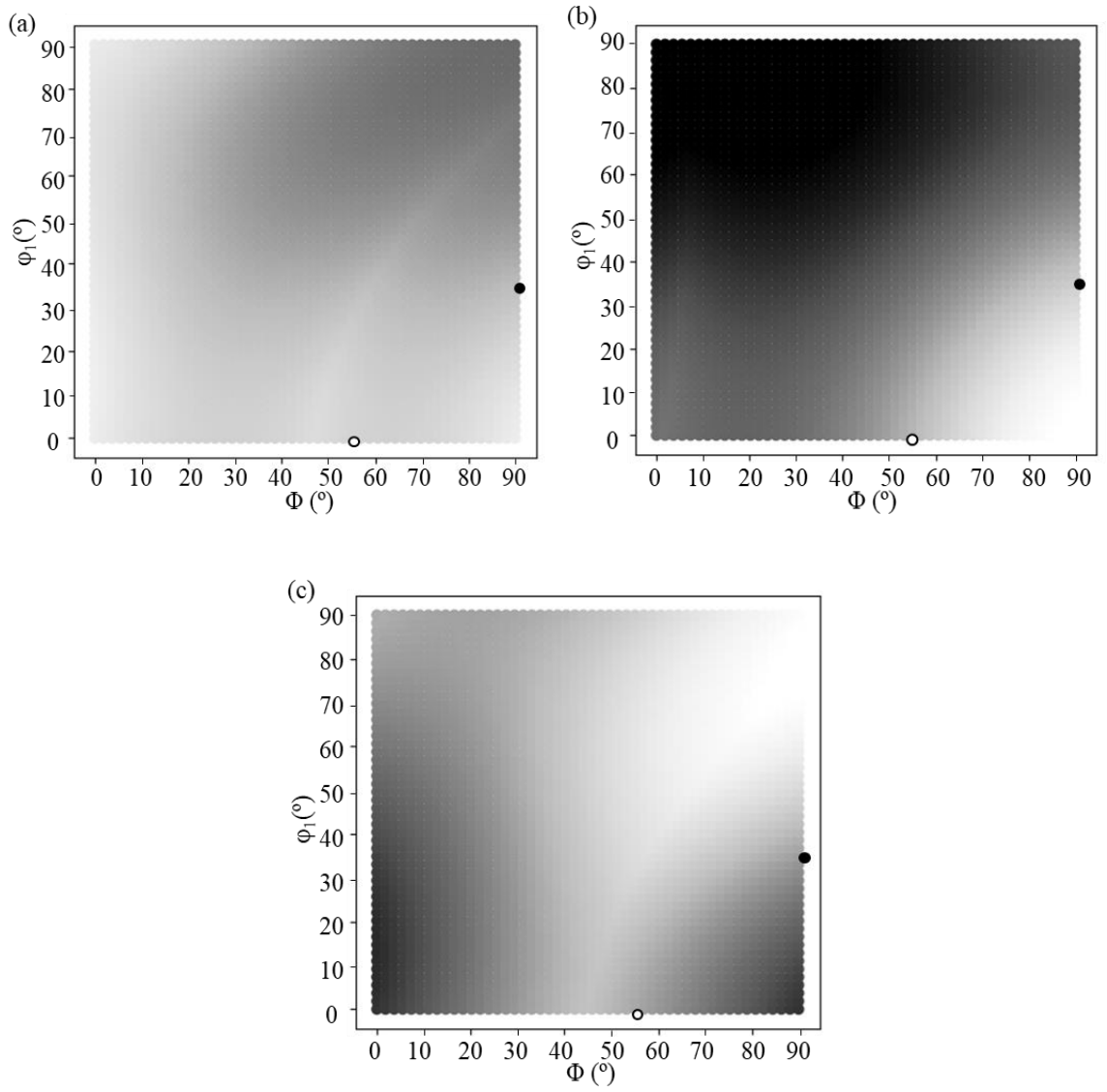

Figure 5.10. Unitless driving force for martensitic transformation as a function of orientation with φ_2 = 45° for (a) uniaxial tension, (b) pure shear, and (c) uniaxial compression. The orientations of longitudinal specimens are marked as solid symbols at (35°, 90°, 45°). The orientations of transverse specimens are marked as open symbols at (0°, 55°, 45°).

5.4.2. Effect of chemistry on martensitic phase transformation kinetics

The elemental compositions of the two SS304L walls, given in Table 2.1, affect the rate, with respect to plastic strain, and saturation values of martensitic transformation kinetics in the materials, as shown in Figure 5.8. With an increase in the volume fraction of iron powder, the relative content of elements that increase the SFE of austenite (silicon, manganese, chromium, and nickel) decreases. Therefore, compared to the 90% SS304L wall, austenite is less stable, resulting in a higher rate of transformation to, and a higher saturation value of, martensite in the 80% SS304L wall (Figure 5.8).

5.4.3. Stress state-dependent martensitic phase transformation kinetics

Santacreu et al. [148] proposed a stress state independent phase transformation kinetics equation to describe the evolution of martensite content as a function of plastic strain in conventionally processed austenitic 301LN stainless steel, as given in Eqn. (4.9).

The martensitic transformation kinetics curves in the 80% and 90% SS304L walls are stress state dependent, as shown in Figure 5.8. Therefore, a stress state dependent martensitic transformation kinetics equation is required. Beese and Mohr [50] expanded the transformation kinetics equation in Eqn. (4.9) by incorporating the effect of stress rate, where the stress state can be described by the stress triaxiality, η, and Lode angle parameter, $\bar{\theta}$. Stress triaxiality, η, is defined as:

$$\eta = \frac{\sigma_m}{\sigma_{vM}} \tag{5.6}$$

where σ_m is the hydrostatic stress, which is proportional to the first invariant, I_1, of stress tensor, $\boldsymbol{\sigma}$; and σ_{vM} is the von Mises equivalent stress, which is a function of the second invariant, J_2, of the deviatoric stress tensor, $\boldsymbol{s}$, given as:

$$\sigma_m = \frac{1}{3} I_1 = \frac{1}{3}\mathrm{tr}(\boldsymbol{\sigma}) \text{ and } \sigma_{vM} = \sqrt{3J_2} = \sqrt{\frac{3}{2}\boldsymbol{s}\cdot\boldsymbol{s}} \tag{5.7}$$

The Lode angle parameter is expressed as:

$$\bar{\theta} = 1 - \frac{2}{\pi}\arccos\left(\frac{3\sqrt{3}}{2}\frac{J_3}{\sqrt{J_2{}^3}}\right) \tag{5.8}$$

where J_3 is the third invariant of $\underline{\mathbf{s}}$, as $J_3 = det\ (\underline{\mathbf{s}})$.

The material parameter D in Eqn. (4.9) may be expressed as a function of stress triaxiality and Lode angle parameter as [50]:

$$D = D_0 + a_\eta \eta + a_\theta \bar{\theta} \tag{5.9}$$

where D_0, a_η, and a_θ are material parameters; and a_η, and a_θ describe the contributions of stress triaxiality and Lode angle parameter.

The stress state dependent transformation kinetics equation proposed by Beese and Mohr [50] is chosen as a starting point for additively manufactured SS304L. The effect of chemistry on transformation kinetics may be taken into account through c_{max} and n [124]. The equation proposed by Beese and Mohr [50] describes the transformation rate in terms of stress triaxiality and Lode angle parameter. The calibrated equation captured the fact that material loaded under uniaxial tension had the highest transformation rate, followed by that loaded under pure shear and uniaxial compression in untextured austenitic stainless steel. These data and calibrated equation were explained by the fact that the tensile normal stress acting on the maximum shear plane, which aids martensitic transformation [55], increases with stress triaxiality and Lode angle parameter in an untextured material [50].

The present study investigates materials with elongated textured grains, in contrast to the nearly isotropic material with equiaxed grains studied in [50]. As shown in Figure 5.8, the rate of martensitic transformation with respect to plastic strain in the present study from high to low is: uniaxial compression, uniaxial tension, and pure shear. The anomaly in the present data compared to data for isotropic stainless steel can be explained by the effect of texture. In order to capture the effect of texture, Eqn. (5.9) is modified to give:

$$D = D_0 + a_\eta \eta + a_\theta \bar{\theta} + a_W W \tag{5.10}$$

where W is the unitless driving force for martensitic transformation, which depends on texture and applied stress, and the constant a_W describes the effect of W on the rate of phase transformation.

The initial values of stress triaxiality, η, and Lode angle parameter, $\bar{\theta}$, for the tests performed in the present study are given in Table 5.2. The parameters, D_0, a_η, a_θ, and a_W were calibrated using experimentally measured curves under uniaxial tension, pure shear, and uniaxial compression stress states from the 80% and 90% SS304L walls, with the calibrated values given in Table 5.3. As shown in Figure 5.8, the calibrated transformation kinetics equation is able to capture the experimental curves under all the three studied states.

Table 5.2. Initial stress triaxiality, η, and Lode angle parameter, $\bar{\theta}$, for the stress states studied.

	Combined loading with β = 60°	**Uniaxial tension**	**Combined loading with β = 30°**	**Pure shear**	**Uniaxial compression**
η	0.38	0.33	0.16	0	-0.33
$\bar{\theta}$	0.85	1	0.46	0	-1

Table 5.3. Parameters for the transformation kinetics equation for the 80% and 90% SS304L walls.

	D_0	a_η	$a_{\bar{\theta}1}$	a_W	D
Uniaxial tension	2.8	10.5	-3.6	14.2	3.4
Pure shear					2.8
Uniaxial compression					4.4

5.5. Summary and conclusions

Two 304L stainless steel walls with different initial powder compositions were fabricated using DED AM and loaded under multiaxial stress states to investigate the effects of stress state and chemistry on strain-induced martensitic phase transformation in textured samples. The primary results of this work are:

- In additively manufactured SS304L, there was no clear anisotropy in the martensitic transformation kinetics; however, the transformation kinetics did depend on stress state. In both walls, the rate of martensitic transformation with respect to plastic strain was highest under uniaxial compression, followed by uniaxial tension, and lowest under pure shear. This result contradicts most of the reported findings of stress state-dependent martensitic transformation in isotropic materials, as martensitic transformation under uniaxial compression was aided by the initial texture in the current materials.
- A stress state- and texture-dependent strain-induced martensitic transformation kinetics equation was proposed for additively manufactured SS304L using data from uniaxial tension, pure shear, and uniaxial compression. In a single wall, the rate of martensitic transformation with respect to plastic strain depended on stress triaxiality, Lode angle

parameter, and driving force for martensitic transformation, which is dependent on texture and applied stress state.

- The martensitic transformation kinetics also depend strongly on chemistry. Under the same stress state, the wall with a lower austenite stability (higher volume fraction of iron) had a higher rate of martensite transformation (with respect to plastic strain), and a higher saturation value of strain-induced martensite volume fraction.

Acknowledgments

The authors gratefully acknowledge the financial support provided by the National Science Foundation through award number CMMI-1402978 and CMMI-1652575. Any opinions, findings, and conclusions or recommendations in the materials are those of the authors and do not necessarily reflect the views of the Nation Science Foundation. We acknowledge Mr. Jay Tressler for component fabrication and Mr. Griffin Jones for the X-ray CT scans at the Center for Innovation Materials Processing through Direct Digital Deposition (CIMP-3D). We thank Dr. Dong Ma and Mr. Matthew Frost of ORNL for neutron diffraction data collection and technical support at the VULCAN beamline, Dr. Alexandru D. Stoica of ORNL for Rietveld refinement analysis, and Dr. Pierre-Olivier Santacreu for magnetic saturation measurements.

Chapter 6

Plasticity model coupled with strain-induced martensitic transformation kinetics

6.1. Introduction

Constitutive plasticity models have been developed extensively for conventionally processed steels undergoing strain-induced martensitic phase transformation, and they can be grouped as micromechanical and phenomenological models [52,53,163–175]. Micromechanical models involve the modeling of the phase evolution due to martensitic transformation, and the prediction of the macroscopic constitutive behavior using homogenization methods varying from a simple rule of mixtures [163,164,168,173] to more advanced methods [52,165,174,175]. Hallberg et al. [163] proposed a micromechanical constitutive model for austenitic stainless steels, consisting of a von Mises yield surface and a stress state-dependent phase transformation potential function. In their model, the yield surface is determined by using a nonlinear mixture rule to combine the yield stresses of austenite and martensite, and the transformation potential depends on the second and third invariants of the deviatoric stress tensor. Post et al. [164] proposed a model to describe the constitutive behavior of stainless steel with stress-assisted martensitic transformation, in which austenite-to-martensite phase transformation occurs under elastic

---

Reproduced from: Z. Wang and A. M. Beese, "Plasticity model coupled with strain-induced martensitic transformation kinetics for austenitic stainelss steel deposited by additive manufactutring," *Submitted for publication* [176].

deformation [47], and strain-induced martensitic transformation. In their model, the flow stresses of austenite and martensite are determined by dislocation density, phase fraction, and plastic strain. The macroscopic flow stress is computed by incorporating the flow stresses of the two phases using a nonlinear rule of mixtures.

Stringfellow and Parks [48,52] proposed a self-consistent homogenization model to predict the plasticity behavior of alloys with strain-induced martensitic transformation. The model assumes an isotropic distribution of spherical martensite inclusions in homogeneous austenite matrix. The macroscopic stress is described by the volume fraction, plastic strain, and time-dependent mechanical properties of austenite and martensite. Bhattacharyya and Weng [165] predicted the stress-strain behavior of metals with an austenite-to-martensite phase transformation using an energy approach. In their model, the effective stress is estimated based on the potential energy and change in the Gibbs free energy due to phase transformation while the effective strain is computed using the lattice parameters of austenite and martensite. Zaera et al. [175] developed a temperature-dependent constitutive model for TRIP steels. The effect of temperature on phase transformation kinetics and yield strength of each phase is incorporated and the macroscopic mechanical behavior is determined through a homogenization method for an isotropic composite. Msolli et al. [174] modeled the mechanical behavior of 304L stainless steel by assuming spherical martensite inclusions were isotropically embedded in the austenite matrix. In their model, a mean field homogenization approach is applied to compute macroscopic constitutive behavior from the constitutive behavior of austenite and martensite.

Unlike micromechanics-based models, phenomenological models directly define the macroscopic constitutive equations. Miller and McDowell [171] proposed a phenomenological constitutive model for face-centered cubic metals with strain-induced martensitic transformation, in which the yield and hardening functions are stress state-dependent. The effect of martensitic transformation on mechanical behavior was incorporated in the hardening function. Hänsel et al. [166] proposed a temperature-dependent plasticity model for TRIP steels, which includes a von Mises yield surface and an isotropic hardening law, in which the flow stress is a function of martensite content, temperature, and plastic strain. Mohr and Jacquemin [167] developed a macroscopic constitutive model for anisotropic austenitic stainless steels. The plasticity behavior was described by a Hill'48 yield surface [177], an associated flow rule, and a non-associated anisotropic hardening law. Beese and Mohr [53] proposed a stress state-dependent plasticity model for austenitic stainless steels, which is composed of a Hill'48 yield surface [177] with a nonlinear kinematic hardening law, an associated flow rule, and an isotropic hardening law coupled with a stress state-dependent martensitic transformation kinetics equation to account for strain hardening due to phase transformation. Yu et al. [170] described the constitutive behavior of TRIP steels using a von Mises yield surface, an associated flow rule, and a mixed isotropic and kinematic hardening law, which is a function of plastic strain and volume fraction of martensite. Hazar et al. [169] developed a macroscopic constitutive model for martensitic steels, which is described by a Drucker Prager yield surface coupled with nonlinear kinematic hardening law, a non-associated flow rule, and isotropic hardening law coupled with stress-assisted and strain-induced martensitic phase transformation kinetics equations.

While models for conventionally processed austenitic stainless steels experiencing strain-induced martensitic transformation have been developed [52,53,163–175], thus far, no work has examined the multiaxial behavior of additively manufactured stainless steels. The objectives of this work were to investigate the multiaxial plasticity behavior of, and propose a macroscopic plasticity model for, additively manufactured SS304L. The proposed model consists of a von Mises yield surface, an associated flow rule, and an isotropic hardening law coupled with a stress state-, texture-, and chemistry-dependent, martensitic transformation kinetics equation. The plasticity model was implemented into a finite element software, and calibrated and validated using experimental data under uniaxial tension, uniaxial compression, pure shear, and combined tension and shear.

6.2. Experimental procedures

6.2.1. Uniaxial tension and uniaxial compression

Longitudinal and transverse uniaxial tension specimens and cylindrical compression were extracted from the 80% and 90% SS304L walls. They were used to perform uniaxial tension and uniaxial compression tests, as described in Chapter 5.

6.2.2. Multiaxial loading

Longitudinal plasticity specimens, as described in Chapter 5, were also extracted from the 80% and 90% SS304L walls for multiaxial loading tests. A biaxial loading angle, β, is defined as:

$$\tan\beta = \frac{F_v}{F_h} \tag{6.1}$$

where F_v is the applied vertical force and F_h is the applied horizontal force. Therefore, β = 0° corresponds to pure shear, β = 90° corresponds to plane strain tension, and 0° < β < 90° corresponds to combined tension and shear. In this study, β values of 0°, 30°, and 60° were examined and the loading conditions for all the tests are given in Table 6.1.

Table 6.1. Loading conditions of plane strain tension, pure shear, and combined loading.

	Strain/stress rate in vertical direction	**Strain/stress rate in horizontal direction**
Pure shear	0 /s	1.3 x 10^{-4} /s
Combined loading with β = 30°	2.1 MPa/s	3.6 MPa/s
Combined loading with β = 60°	3.6 MPa/s	2.1 MPa/s

6.3. Plasticity model

A macroscopic constitutive model was developed to describe the multiaxial plasticity behavior of additively manufactured SS304L under quasi-static loading at room temperature. The model includes a yield surface, an associated flow rule, and an isotropic hardening law. The hardening law incorporates the effect of stress state, texture, and chemistry on strain-induced martensitic transformation, and the effect of martensite content on multiaxial plasticity behavior through the implementation of a transformation kinetics equation. The model was implemented into the commercial finite element software (ABAQUS/Explicit 6.14 [134]), calibrated, and validated.

6.3.1. Yield surface

The yield surface of a material is described as:

$$f = \bar{\sigma} - k = 0 \tag{6.2}$$

where $\bar{\sigma}$ is the equivalent stress and k is the flow stress.

As there was no clear anisotropy in yield strength in the additively manufactured SS304L, as discussed in Chapters 3 and 4, the isotropic von Mises yield criterion was adopted, and Eqn. (6.2) becomes:

$$\bar{\sigma}_{vM} - k = 0 \tag{6.3}$$

where $\bar{\sigma}_{vM}$ is the von Mises equivalent stress.

In the plane stress condition, there are no non-zero stresses in the z direction. The stress tensor, $\underline{\boldsymbol{\sigma}}$, can be expressed by a stress vector, $\boldsymbol{\sigma}$, as:

$$\boldsymbol{\sigma} = \{\sigma_L, \sigma_T, \tau\}^{\mathrm{T}} \tag{6.4}$$

where σ_L and σ_T are normal stresses along the longitudinal (L) and transverse (T) directions, as shown in Figure 5.1; τ is the in-plane shear stress.

Then the von Mises yield equivalent stress, $\bar{\sigma}_{vM}$, as described in Eqn. (5.7) is simplified as:

$$\bar{\sigma}_{vM} = \sqrt{\sigma_L^2 - \sigma_L\sigma_T + \sigma_T^2 + 3\tau} \tag{6.5}$$

6.3.2. Associated flow rule

An associated flow rule is used to describe the direction of plastic strain increment with respect to the von Mises yield surface, which is given as:

$$\mathrm{d}\underline{\boldsymbol{\varepsilon}}^P = d\lambda \frac{\partial \bar{\sigma}_{vM}}{\partial \underline{\boldsymbol{\sigma}}} \tag{6.6}$$

where $d\underline{\boldsymbol{\varepsilon}}^P$ is the increment of plastic strain and $d\lambda$ is the plastic multiplier.

6.3.3. Isotropic hardening law

An isotropic hardening law is selected to describe the increase in flow stress, *k*, as a function of plastic strain during deformation. In SS304L, the strain hardening is due to both dislocation interactions and strain-induced martensitic phase transformation. To account for both of these effects, an isotropic hardening law is adopted from [53], and given as:

$$dk = H_\varepsilon d\bar{\varepsilon}_{vM}^P + H_c dc \tag{6.7}$$

where H_ε and H_c are hardening moduli, $d\bar{\varepsilon}_{vM}^P$ is the increment of von Mises equivalent plastic strain, and *dc* is the increment of martensite volume fraction.

The first term in Eqn. (6.7) describes the strain hardening from dislocation pile up during plastic deformation and is assumed to follow a Swift hardening law [178], as:

$$k = A(\varepsilon_0 + \bar{\varepsilon}_{vM}^P)^n + k_0 \tag{6.8}$$

where *A*, ε_0, *m*, and k_0 are material parameters. As Eqn. (6.8) describes the strain hardening only due to dislocation interactions, *A*, ε_0, *n*, and k_0 are assumed to be the same for the two walls with different chemistries.

The second term in Eqn. (6.7) describes the strain hardening due to the increase of martensite content. As the amount of martensite transformed as a function of plastic strain is influenced by chemistry, the hardening modulus, H_c, is assumed to be chemistry dependent, and therefore, varies between the 80% and 90% SS304L walls.

6.3.4. Martensitic transformation kinetics

The chemistry-, stress state- and texture-dependent martensitic transformation kinetics equation developed in Chapter 5 is adopted here to describe the martensite volume fraction as a function of plastic strain. The stress state may be characterized by the stress triaxiality, η and Lode angle parameter, $\bar{\theta}$ [50]. The initial values of η and $\bar{\theta}$ of the stress states studied are given in Table 5.2.

The differential form of the martensitic transformation kinetics equation in Eqn. (4.9) is given as:

$$dc = (c_{max} - c)mD(D\bar{\varepsilon}_{vM}^{P})^{m-1}d\bar{\varepsilon}_{vM}^{P} \tag{6.9}$$

where the parameter *D* may be taken to be a function of η, $\bar{\theta}$, and *W*, as given in Eqn. (5.10).

6.4. Results and discussion

6.4.1. Overview

Representative stress- strain curves for longitudinal specimens from the two walls are given in Figure 6.1. Within the same wall, the strain hardening rate, defined as the slope of the stress-strain curve, was highest under uniaxial compression, followed by uniaxial tension, and lowest under pure shear, which can be explained by the stress state-dependent martensitic transformation kinetics. As discussed in Chapter 5, the rate of martensitic transformation with respect to plastic strain from high to low was uniaxial compression, uniaxial tension, and pure shear, which is in consistent with the trend in strain hardening rate with respect to stress state seen here.

Under the same stress state, and for any given plastic strain, the 80% SS304L wall had a higher flow stress than the 90% SS304L wall. As the iron content increased, the relative content of elements that increase the SFE in austenite, and therefore impede austenite-to-martensite phase transformation (silicon, manganese, chromium, and nickel), decreased, and the rate of martensitic transformation with respect to plastic strain increased. Therefore, the 80% SS304L wall had a higher martensitic transformation rate and flow stress at a given plastic strain, compared to the 90% SS304L wall.

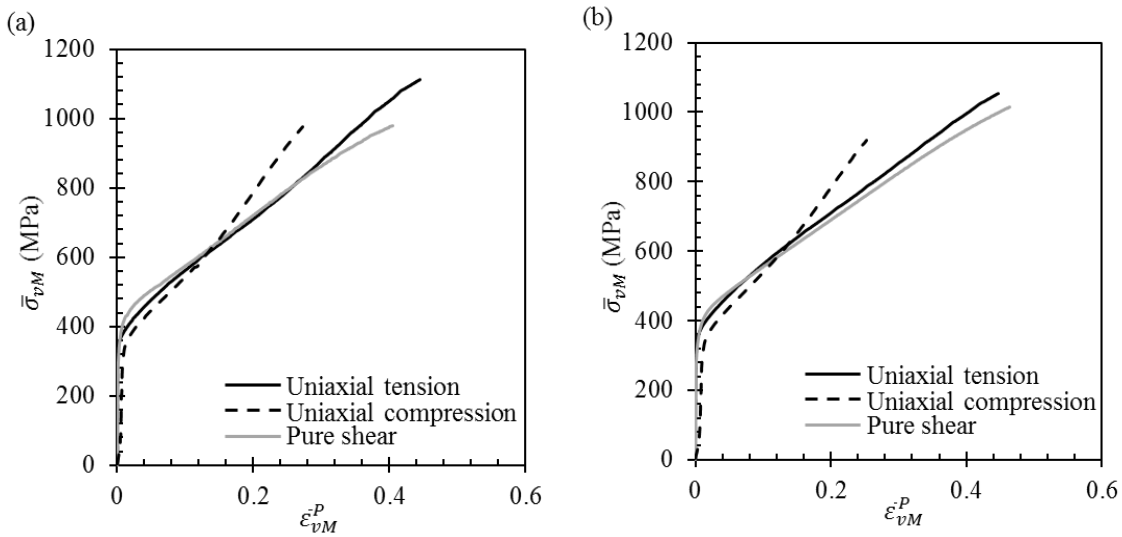

Figure 6.1. Von Mises equivalent stress, $\bar{\sigma}_{vM}$, versus von Mises equivalent plastic strain, $\bar{\varepsilon}^P_{vM}$, for representative specimens from (a) the 80% SS304L wall, and (b) the 90% SS304L wall.

6.4.2. Model calibration

The experimentally measured 0.2% offset yield strengths under different stress states are plotted on the von Mises yield surface, as shown in Figure 6.2. As all the points lie on

or close to the yield surface, the von Mises yield criterion is sufficient to describe the yielding of the walls studied.

The plasticity model was implemented into a commercial finite element code (ABAQUS/Explicit 6.14 [134]). A shell element (type S4R) with a side length of 1 mm and a thickness of 1.5 mm was used to represent the gauge center of each specimen. The martensitic transformation kinetics equation parameters (c_{max}, m, D_0, a_η, a_θ, and a_W) were calibrated for the 80% and 90% SS304L walls in Chapter 5. The remaining model parameters that required identification were the strain hardening parameters (A, ε_0, n, k_0, and H_c). These parameters were first estimated using experimentally measured true stress-plastic strain curves from uniaxial tension, and a range defined as 0.5 x estimated value to 1.5 x estimated value was assigned to each parameter. For calibration, over 1000 simulations were performed with varying model inputs. For each simulation, a set of parameters s_i = {A, ε_0, n, k_0, and H_c}, each within their prescribed range, was randomly selected based on the assumption of a uniform value distribution within each range. Using these parameters, the stress, $\sigma_{sim,j}(s_i)$, was computed for a given experimentally studied strain history, where j is the number of stress states used for model calibration. A cost function was evaluated for each set of parameters, defined as:

$$\chi(s_i) = \sum_{j=1}^{J} \left| \frac{\sigma_{sim,j}(s_i) - \sigma_{exp,j}}{\sigma_{exp,j}} \right| \tag{6.10}$$

where $\sigma_{exp,j}$ is the experimentally measured engineering stress. The optimized set of model parameters was chosen to minimize χ.

In the present study, experimental data from uniaxial tension, uniaxial compression, and pure shear from the two walls were used for model calibration, giving J = 6. The calibrated model parameters are given in Table 6.2.

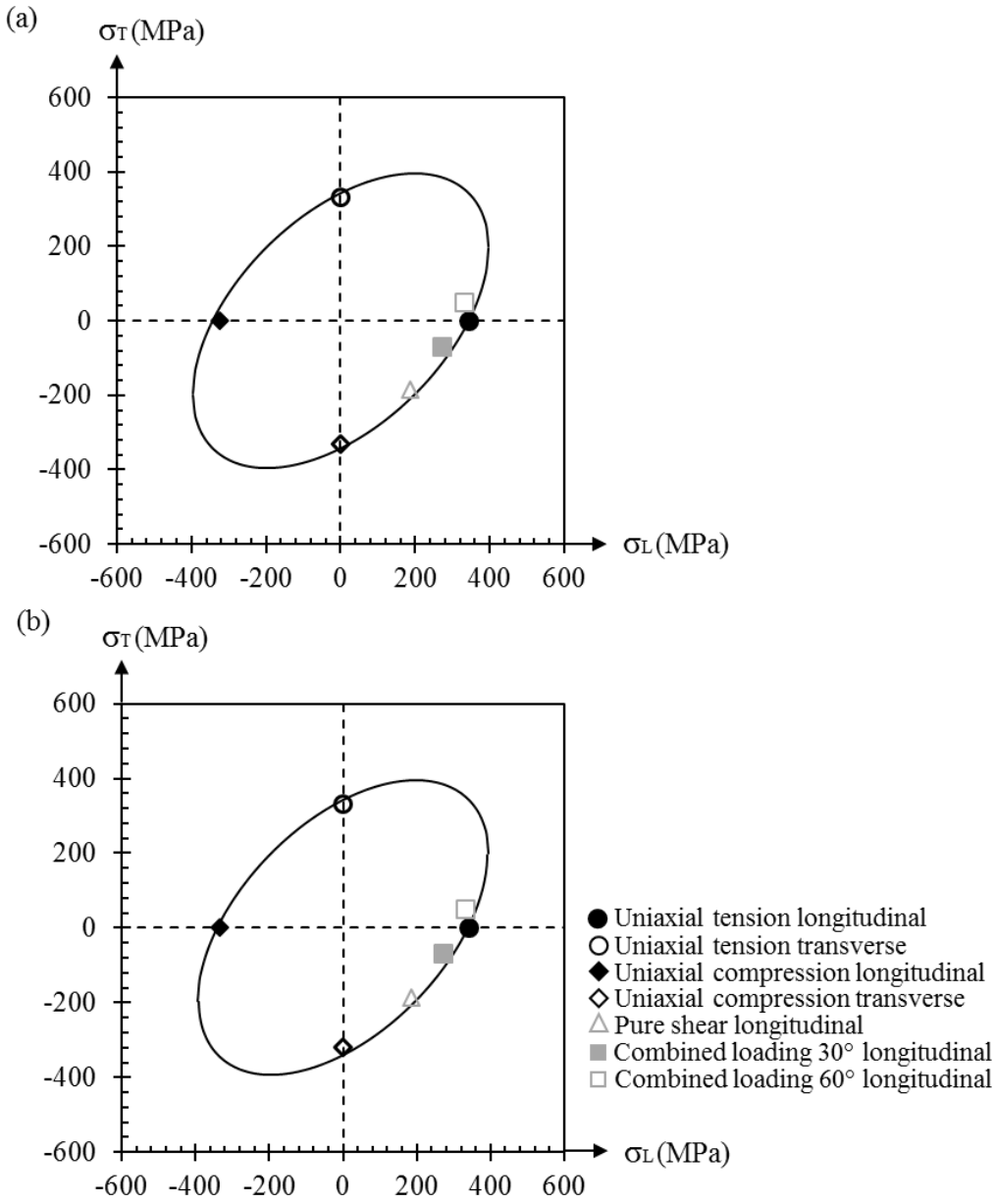

Figure 6.2. Engineering yield stress in the transverse direction, σ_T, versus engineering yield stress in the longitudinal direction, σ_L in the (a) 80% SS304L wall, and (b) 90% SS304L wall. The von Mises yield surface, based on uniaxial tension in the longitudinal direction, is also drawn. The symbols represent experimentally measured yield points under the stress states studied.

Table 6.2. Calibrated material parameters of the plasticity model for the 80% and 90% SS304L walls.

	80% SS304L	**90% SS304L**
A **(MPa)**	776.5	776.5
ε_0	0.01	0.01
n	0.55	0.55
k_0 **(MPa)**	384.2	384.2
H_c **(MPa)**	5.0	5.0
c_{max} **(vol.%)**	77	58
m	2.5	2.8
D_0	2.4	2.4
a_η	10.5	10.5
a_θ	-3.6	-3.6
a_W	14.2	14.2

6.4.3. Comparison between simulation and experimental results

The experimentally measured and predicted engineering stress–plastic strain curves under uniaxial tension, uniaxial compression, and pure shear from the two walls are plotted in Figure 6.3. Table 6.3 summarizes the maximum stress difference between simulation and experimental results for each stress state. As shown in Table 6.3, among all the stress states, the simulations have a maximum difference in flow stress of 7% from the experimental stress level in the 80% SS304L wall and 8% in the 90% SS304L wall. The good agreement between the computationally predicted and experimental results indicates that the plasticity model coupled with the underlying phase transformation equation is able to describe the multiaxial plasticity behavior of additively manufactured SS304L.

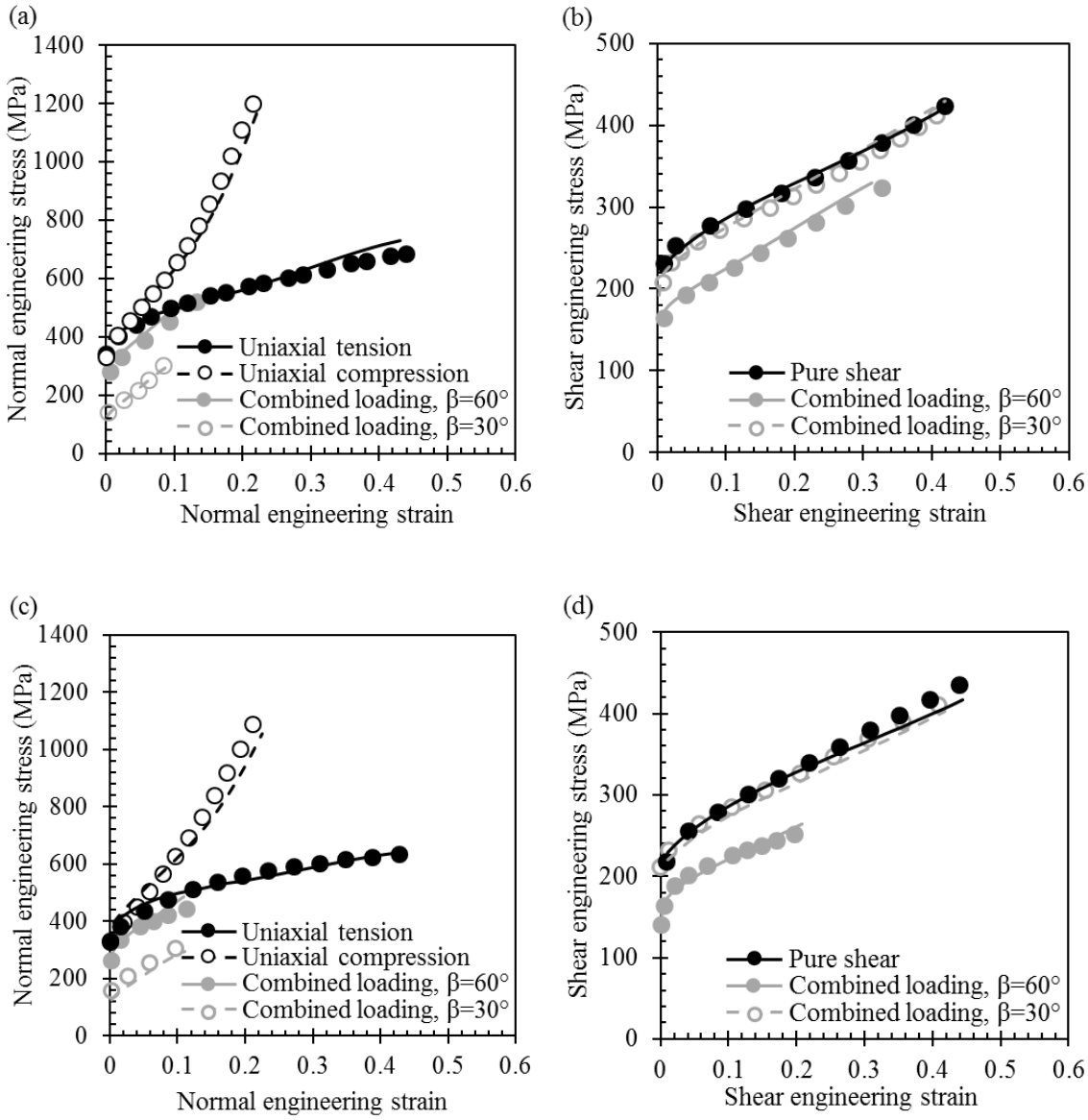

Figure 6.3. Normal engineering stress-plastic strain curves for specimens under uniaxial tension, uniaxial compression, and combined loading for the (a) 80% SS304L wall and (c) 90% wall. Shear engineering stress-plastic strain curves for specimens under pure shear and combined loading for the (b) 80% SS304L wall and (d) 90% SS304L wall. Symbols correspond to experimental results and lines correspond to results predicted by the calibrated plasticity model.

Table 6.3. Maximum stress difference between experimental and simulation results with respect to experimental results under uniaxial tension, uniaxial compression, pure shear, and combined loading.

	Stress state	Difference in normal stress (%)	Difference in shear stress (%)
80% SS304L	Uniaxial tension	6.5	-
	Uniaxial compression	6.5	-
	Pure shear	-	0.3
	Combined loading with $\beta = 30^o$	4.4	4.0
	Combined loading with $\beta = 60^o$	7.8	3.6
90% SS304L	Uniaxial tension	1.2	-
	Uniaxial compression	7.9	-
	Pure shear	-	4.5
	Combined loading with $\beta = 30^o$	7.5	2.9
	Combined loading with $\beta = 60^o$	9.1	3.9

6.4.4. Model validation

In order to validate the plasticity model, simulations of combined tension/shear loading with $\beta = 30^o$ and 60^o were performed and compared to the experimentally measured data. The finite element simulations were also conducted using a shell element (S4R) with a side length of 1 mm and a thickness of 1.5 mm. The predicted engineering stress-plastic strain curves are in good agreement with experimentally measured curves, as shown in Figure 6.3. The maximum stress difference between simulation and experimental results is also given in Table 6.3, which shows the difference between the simulation and experimental results is within 8% from the experimental stress level in the 80% SS304L wall and 9% in the 90% SS304L wall under combined loading. The small difference between computationally predicted and experimentally measured curves indicates that the proposed

plasticity model is able to predict the mechanical behavior of additively manufactured SS304L under multiaxial stress states.

6.5. Summary and conclusions

Two SS304L walls with different chemical compositions were fabricated by DED AM and subjected to a range of stress states to investigate the multiaxial plasticity behavior of these materials. Based on the experimental observations, a macroscopic plasticity model is proposed for the materials. The primary findings of this study are as follows:

- The plasticity behavior of additively manufactured SS304L walls depends on stress state and chemistry. In a single wall subjected to multiaxial stress states, the strain hardening rate (at a given plastic strain) was highest in uniaxial compression, lowest in pure shear, and intermediate in uniaxial tension. In the two walls under the same stress state, the wall with lower stacking fault energy, and therefore, austenite stability, due to higher iron content, had a higher rate of martensitic transformation and flow stress at a given plastic strain.
- A plasticity model consisting of a von Mises yield surface, an associated flow rule, and an isotropic hardening law coupled with a stress state-, texture-, and chemistry-dependent martensitic transformation kinetics equation is able to describe and predict the constitutive behavior of additively manufactured SS304L under multiaxial stress states.

Acknowledgments

The authors gratefully acknowledge the financial support provided by the National Science Foundation through award number CMMI-1402978 and CMMI-1652575. Any opinions, findings, and conclusions or recommendations in the materials are those of the authors and do not necessarily reflect the views of the Nation Science Foundation. Samples were fabricated at Penn State's Center for Innovation Materials Processing through Direct Digital Deposition (CIMP-3D). We acknowledge Dr. Dong Ma of ORNL for performing uniaxial compression tests.

Chapter 7

Summary and future work

7.1. Summary and conclusions

The objectives of this thesis were to:

- Investigate process-microstructure-multiaxial mechanical property relationships in 304L austenitic stainless steel made by directed energy deposition additive manufacturing, and
- Develop a physically-based macroscopic plasticity model that relates microstructural phase transformation to macroscopic multiaxial properties.

The effect of processing parameters on microstructure and mechanical properties was elucidated using two pure SS304L walls that were built using different linear heat inputs. Due to the high nitrogen content in the pre-alloyed SS304L powder, austenite-to-martensite phase transformation did not occur in the pure SS304L walls. In each wall, as heat was retained in the wall during AM, it was postulated that the cooling rate decreased as the distance from the substrate increased, resulting in an increase in the average austenite grain size, and therefore, decreases in the yield and ultimate tensile strengths. At the same location, the wall fabricated using lower heat input would have had a smaller melt pool, and therefore, higher thermal gradient and higher cooling rate. This presumed difference in thermal history resulted in a smaller average grain size, and therefore higher yield and ultimate tensile strengths, in the wall with made using the lower linear heat input compared to the wall using higher heat input. A grain growth model adopted from welding was used to quantitatively describe austenite grain size as a function of linear heat input and location.

A Hall-Petch relation, and a consideration of grain morphology and orientation, was used to quantitatively link austenite grain size with location-dependent yield strength.

The effect of chemistry, namely initial powder chemistry and spatial chemical variations due to elemental vaporization, on martensitic transformation and mechanical properties was investigated using two walls deposited from a mixture of SS304L powder and iron powder. The iron-SS304L walls had higher ultimate tensile strengths and ductility than the pure SS304L walls due to the presence of martensitic phase transformation. In each iron-SS304L wall, the concentration of elements that increase the stacking fault energy of austenite decreased as the distance from the substrate increased due to vaporization. Therefore, austenite stability decreased and martensitic transformation increased as the distance from the substrate increased, resulting in an increase in ultimate tensile strength. A chemistry-dependent martensitic transformation kinetics equation that describes martensite content with respect to plastic strain was proposed and calibrated. The rate of martensitic transformation with respect to plastic strain, and the saturation value of martensite content increased, as the concentration of elements that increase the stacking fault energy of austenite decreased.

The effect of stress state and texture on strain-induced martensitic phase transformation was also investigated using additively manufactured SS304L with different chemistries loaded under uniaxial tension, uniaxial compression, and pure shear. The rate of phase transformation with respect to plastic strain from high to low was: uniaxial compression, uniaxial tension, and pure shear, which contradicts the findings in texture-free austenitic stainless steels. The trend in the additively manufactured material is the initial texture in the material facilitated martensitic transformation under uniaxial compression, or

conversely, texture impeded transformation under uniaxial tension. A stress state- and texture-dependent transformation kinetics equation was developed and calibrated for additively manufactured SS304L.

Based on the understanding of process-microstructure-multiaxial mechanical property relationships, a physically-based macroscopic plasticity model is developed for additively manufactured SS304L with different chemistries under multiaxial stress states. The plasticity model makes use of a von Mises yield surface, an associated flow rule, and an isotropic hardening law. The effect of chemistry, stress state, and texture on martensitic transformation, and the effect of martensitic transformation on mechanical behavior were incorporated in the hardening law through the martensitic transformation kinetics equation. The plasticity model was implemented into a finite element code for calibration and validation. The simulated stress-strain curves were in good agreement with experimentally measured curves, indicating the plasticity model can be used to describe and predict the multiaxial mechanical behavior for additively manufactured SS304L.

7.2. Future work

The multiaxial mechanical behavior of additively manufactured SS304L is systematically investigated through experimental and computational approaches in the thesis. The proposed plasticity model is the foundation for a multiaxial fracture model, as plastic deformation is followed by fracture. In order to understand the fracture behavior of additively manufactured SS304L, further research includes performing multiaxial fracture experiments to characterize the fracture properties under multiaxial stress states,

determining strain to failure under each stress state through finite element analysis, and developing a multiaxial fracture model.

Appendix

Published papers during Ph.D. study

Z. Wang, T. A. Palmer, and A. M. Beese, "Effect of processing parameters on microstructure and tensile properties of austenitic stainless steel 304L made by directed energy deposition additive manufacturing," *Acta Mater.*, vol. 110, pp. 226–235, 2016.

Z. Wang, A. D. Stoica, D. Ma, and A. M. Beese, "Diffraction and single-crystal elastic constants of Inconel 625 at room and elevated temperatures determined by neutron diffraction," *Mater. Sci. Eng. A*, vol. 674, pp. 406–412, 2016.

Z. Wang and A. M. Beese, "Effect of chemistry on martensitic phase transformation kinetics and resulting properties of additively manufactured stainless steel," *Acta Mater.*, vol. 131, pp. 410–422, 2017.

Z. Wang, E. Denlinger, P. Michaleris, A. D. Stoica, D. Ma, and A. M. Beese, "Residual stress mapping in Inconel 625 fabricated through additive manufacturing: Method for neutron diffraction measurements to validate thermomechanical model predictions," *Mater. Des.*, vol. 113, pp. 169–177, 2017.

D. Ma, A. D. Stoica, Z. Wang, and A. M. Beese, "Crystallographic texture in an additively manufactured nickel-base superalloy," *Mater. Sci. Eng. A*, vol. 684, pp. 47–53, 2017.

A. E. Wilson-Heid, Z. Wang, B. McCornac, and A. M. Beese, "Quantitative relationship between anisotropic strain to failure and grain morphology in additively manufactured Ti-6Al-4V," *Mater. Sci. Eng. A*, vol. 706, pp. 287–294, 2017.

Z. Wang, A. D. Stoica, D. Ma, and A. M. Beese, "Stress relaxation behavior and mechanisms in Ti-6Al-4V determined via in situ neutron diffraction: Application to additive manufacturing," *Mater. Sci. Eng. A*, vol. 707, pp. 585–592, 2017.

Z. Wang, A. D. Stoica, D. Ma, and A. M. Beese, “Stress relaxation in a nickel-base superalloy at elevated temperatures via in situ neutron diffraction characterization: application to additive manufacturing,” *Mater. Sci. Eng. A*, vol. 714, pp. 75–83, 2018.

Z. Wang and A. M. Beese, “Effect of stress state and texture on martensitic phase transformation kinetics of additively manufactured austenitic stainless steel,” *Submitted for publication.*

Z. Wang and A. M. Beese, “Plasticity model coupled with strain-induced martensitic transformation kinetics for austenitic stainless steel deposited by additive manufacturing,” *Submitted for publication.*

A. M. Beese, Z. Wang, A. D. Stoica, and D. Ma, “Absence of dynamic strain aging in an additively manufactured nickel-base superalloy,” *Submitted for publication.*

Bibliography

[1] W. J. Sames, F. A. List, S. Pannala, R. R. Dehoff, and S. S. Babu, “The metallurgy and processing science of metal additive manufacturing,” *Int. Mater. Rev.*, pp. 1–46, 2016.

[2] Z. Wang, T. A. Palmer, and A. M. Beese, “Effect of processing parameters on microstructure and tensile properties of austenitic stainless steel 304L made by directed energy deposition additive manufacturing,” *Acta Mater.*, vol. 110, pp. 226–235, 2016.

[3] D. D. Gu, W. Meiners, K. Wissenbach, and R. Poprawe, “Laser additive manufacturing of metallic components: materials, processes and mechanisms,” *Int. Mater. Rev.*, vol. 57, no. 3, pp. 133–164, 2012.

[4] J. Yu, M. Rombouts, and G. Maes, “Cracking behavior and mechanical properties of austenitic stainless steel parts produced by laser metal deposition,” *Mater. Des.*, vol. 45, pp. 228–235, 2013.

[5] S. Das, J. J. Beama, M. Wohlert, and D. L. Bourell, “Direct laser freeform fabrication of high performance metal components,” *Rapid Prototyp. J.*, vol. 4, no. 3, pp. 112–117, 1998.

[6] D. D. Gu, W. Meiners, K. Wissenbach, and R. Poprawe, “Laser additive manufacturing of metallic components: materials, processes and mechanisms,” *Int. Mater. Rev.*, vol. 57, no. 3, pp. 133–164, 2012.

[7] W. Gao, Y. Zhang, D. Ramanujan, K. Ramani, Y. Chen, C. B. Williams, C. C. L. Wang, Y. C. Shin, S. Zhang, and P. D. Zavattieri, “The status, challenges, and future of additive manufacturing in engineering,” *Comput. Des.*, vol. 69, pp. 65–89, 2015.

[8] B. E. Carroll, T. A. Palmer, and A. M. Beese, “Anisotropic tensile behavior of Ti–6Al–4V components fabricated with directed energy deposition additive manufacturing,” *Acta Mater.*, vol. 87, pp. 309–320, 2015.

[9] P. Edwards and M. Ramulu, “Fatigue performance evaluation of selective laser melted Ti-6Al-4V,” *Mater. Sci. Eng. A*, vol. 598, pp. 327–337, 2014.

[10] L. Thijs, F. Verhaeghe, T. Craeghs, J. Van Humbeeck, and J.-P. Kruth, “A study of the microstructural evolution during selective laser melting of Ti–6Al–4V,” *Acta Mater.*, vol. 58, no. 9, pp. 3303–3312, 2010.

[11] A. M. Beese and B. E. Carroll, “Review of Mechanical Properties of Ti-6Al-4V Made by Laser- Based Additive Manufacturing Using Powder Feedstock,” *JOM*, vol. 68, no. 3, pp. 724–734, 2016.

[12] A. Mertens, S. Reginster, H. Paydas, Q. Contrepois, T. Dormal, O. Lemaire, and J. Lecomte-Beckers, “Mechanical properties of alloy Ti–6Al–4V and of stainless steel 316L processed by selective laser melting: influence of out-of-equilibrium microstructures,” *Powder Metall.*, vol. 57, no. 3, pp. 184–189, Jul. 2014.

[13] P. a. Kobryn and S. L. Semiatin, “Mechanical Properties of Laser-Deposited Ti-6Al-4V,” *Solid Free. Fabr. Proc.*, pp. 6–8, 2001.

[14] H. Gong, K. Rafi, H. Gu, T. Starr, and B. Stucker, “Analysis of defect generation in Ti–6Al–4V parts made using powder bed fusion additive manufacturing processes,” *Addit. Manuf.*, vol. 1–4, pp. 87–98, Oct. 2014.

[15] Z. Wang, A. D. Stoica, D. Ma, and A. M. Beese, “Stress relaxation behavior and mechanisms in Ti-6Al-4V determined via in situ neutron diffraction: Application to additive manufacturing,” *Mater. Sci. Eng. A*, vol. 707, pp. 585–592, 2017.

[16] A. E. Wilson-Heid, Z. Wang, B. McCornac, and A. M. Beese, “Quantitative relationship between anisotropic strain to failure and grain morphology in additively manufactured Ti-6Al-4V,” *Mater. Sci. Eng. A*, vol. 706, pp. 287–294, 2017.

[17] M. L. Griffith, D. M. Keicher, C. L. Atwood, J. A. Romero, E. Smugeresky, L. D. Harwell, and D. L. Greene, “Free Form Fabrication of Metallic Components Using Laser Engineered Net Shaping (LENS),” *Proc. Solid Free. Fabr. Symp.*, pp. 125–132, 1996.

[18] Y. Xue, A. Pascu, M. F. Horstemeyer, L. Wang, and P. T. Wang, “Microporosity effects on cyclic plasticity and fatigue of LENS^{TM}-processed steel,” *Acta Mater.*, vol. 58, pp. 4029–4038, 2010.

[19] K. Zhang, S. Wang, W. Liu, and X. Shang, “Characterization of stainless steel parts by Laser Metal Deposition Shaping,” *Mater. Des.*, vol. 55, pp. 104–119, 2014.

[20] J. Li, D. Deng, X. Hou, X. Wang, and G. Ma, “Microstructure and performance optimisation of stainless steel formed by laser additive manufacturing,” *Mater. Sci. Technol.*, pp. 1–8, 2016.

[21] M. Ziętala, T. Durejko, M. Polański, I. Kunce, T. Płociński, W. Zieliński, M. Łazińska, W. Stępniowski, T. Czujko, K. J. Kurzydłowski, and Z. Bojar, “The microstructure, mechanical properties and corrosion resistance of 316L stainless steel fabricated using laser engineered net shaping,” *Mater. Sci. Eng. A*, vol. 677, pp. 1–10, 2016.

[22] K. Guan, Z. Wang, M. Gao, X. Li, and X. Zeng, “Effects of processing parameters on tensile properties of selective laser melted 304 stainless steel,” *Mater. Des.*, vol. 50, pp. 581–586, 2013.

[23] B. Zhang, L. Dembinski, and C. Coddet, “The study of the laser parameters and environment variables effect on mechanical properties of high compact parts elaborated by selective laser melting 316L powder,” *Mater. Sci. Eng. A*, vol. 584, pp. 21–31, 2013.

[24] F. Ning and W. Cong, “Microstructures and mechanical properties of Fe-Cr stainless steel parts fabricated by ultrasonic vibration-assisted laser engineered net shaping process,” *Mater. Lett.*, vol. 179, pp. 61–64, 2016.

[25] T. LeBrun, T. Nakamoto, K. Horikawa, and H. Kobayashi, “Effect of Retained Austenite on Subsequent Thermal Processing and Resultant Mechanical Properties of Selective Laser Melted 17-4 PH Stainless Steel,” *Mater. Des.*, vol. 81, pp. 44–53, 2015.

[26] A. Yadollahi, N. Shamsaei, S. M. Thompson, A. Elwany, and L. Bian, “Mechanical and Microstructural Properties of Selective Laser Melted 17-4 PH Stainless Steel,” *Proc. ASME 2015 Int. Mech. Eng. Congr. Expo.*, pp. 1–7, 2015.

[27] E. Brandl, U. Heckenberger, V. Holzinger, and D. Buchbinder, “Additive manufactured AlSi10Mg samples using Selective Laser Melting (SLM): Microstructure, high cycle fatigue, and fracture behavior,” *Mater. Des.*, vol. 34, pp. 159–169, 2012.

[28] K. Kempen, L. Thijs, J. Van Humbeeck, and J.-P. Kruth, “Processing AlSi10Mg by selective laser melting: parameter optimisation and material characterisation,” *Mater. Sci. Technol.*, vol. 31, no. 8, pp. 917–923, 2015.

[29] K. Kempen, L. Thijs, J. Van Humbeeck, and J. P. Kruth, “Mechanical Properties of AlSi10Mg Produced by Selective Laser Melting,” *Phys. Procedia*, vol. 39, pp. 439–

446, 2012.

[30] M. Javidani, J. Arreguin-Zavala, J. Danovitch, Y. Tian, and M. Brochu, “Additive Manufacturing of AlSi10Mg Alloy Using Direct Energy Deposition: Microstructure and Hardness Characterization,” *J. Therm. Spray Technol.*, vol. 26, no. 4, pp. 587–597, 2017.

[31] N. T. Aboulkhair, N. M. Everitt, I. Ashcroft, and C. Tuck, “Reducing porosity in AlSi10Mg parts processed by selective laser melting,” *Addit. Manuf.*, vol. 1, pp. 77–86, 2014.

[32] B. Vandenbroucke and J.-P. Kruth, “Selective laser melting of biocompatible metals for rapid manufacturing of medical parts,” *Rapid Prototyp. J.*, vol. 13, no. 4, pp. 196–203, 2007.

[33] X.-Z. Xin, N. Xiang, J. Chen, D. Xu, and B. Wei, “Corrosion Characteristics of a Selective Laser Melted Co–Cr Dental Alloy under Physiological Conditions,” *J. Mater. Sci.*, vol. 47, pp. 4813–4820, 2012.

[34] F. Xu, Y. Lv, Y. Liu, B. Xu, and P. He, “Effect of heat treatment on microstructure and mechanical properties of inconel 625 alloy fabricated by pulsed plasma arc deposition,” *Phys. Procedia*, vol. 50, pp. 48–54, 2013.

[35] K. N. Amato, S. M. Gaytan, L. E. Murr, E. Martinez, P. W. Shindo, J. Hernandez, S. Collins, and F. Medina, “Microstructures and mechanical behavior of Inconel 718 fabricated by selective laser melting,” *Acta Mater.*, vol. 60, no. 5, pp. 2229–2239, 2012.

[36] Z. Wang, K. Guan, M. Gao, X. Li, X. Chen, and X. Zeng, “The microstructure and mechanical properties of deposited-IN718 by selective laser melting,” *J. Alloys*

Compd., vol. 513, pp. 518–523, 2012.

[37] L. L. Parimi, G. Ravi, D. Clark, and M. M. Attallah, "Microstructural and texture development in direct laser fabricated IN718," *Mater. Charact.*, vol. 89, pp. 102–111, 2014.

[38] N. A. Kistler, A. R. Nassar, E. W. Reutzel, D. J. Corbin, and A. M. Beese, "Effect of directed energy deposition processing parameters on laser deposited Inconel® 718: Microstructure, fusion zone morphology, and hardness," *J. Laser Appl.*, vol. 29, no. 2, p. 22005, 2017.

[39] J. F. Wang, Q. J. Sun, H. Wang, J. P. Liu, and J. C. Feng, "Effect of location on microstructure and mechanical properties of additive layer manufactured Inconel 625 using gas tungsten arc welding," *Mater. Sci. Eng. A*, vol. 676, pp. 395–405, 2016.

[40] X. Gong, X. Wang, V. Cole, Z. Jones, K. Cooper, and K. Chou, "Characterization of microstructure and mechanical property of Inconel 718 from selective laser melting," in *ASME 2015 International Manufacturing Science and Engineering Conference*, 2015, p. V001T02A061-V001T02A061.

[41] Z. Wang, E. Denlinger, P. Michaleris, A. D. Stoica, D. Ma, and A. M. Beese, "Residual stress mapping in Inconel 625 fabricated through additive manufacturing: Method for neutron diffraction measurements to validate thermomechanical model predictions," *Mater. Des.*, vol. 113, pp. 169–177, 2017.

[42] Z. Wang, A. D. Stoica, D. Ma, and A. M. Beese, "Diffraction and single-crystal elastic constants of Inconel 625 at room and elevated temperatures determined by neutron diffraction," *Mater. Sci. Eng. A*, vol. 674, pp. 406–412, 2016.

[43] Z. Wang, A. D. Stoica, D. Ma, and A. M. Beese, “Stress relaxation in a nickel-base superalloy at elevated temperatures via in situ neutron diffraction characterization: application to additive manufacturing,” *Mater. Sci. Eng. A*, vol. 714, pp. 75–83, 2018.

[44] D. Ma, A. D. Stoica, Z. Wang, and A. M. Beese, “Crystallographic texture in an additively manufactured nickel-base superalloy,” *Mater. Sci. Eng. A*, vol. 684, pp. 47–53, 2017.

[45] F. Lecroise and A. Pineau, “Martensitic Transformations Induced By Plastic-Deformation in Fe-Ni-Cr-C System,” *Metall. Trans.*, vol. 3, pp. 387–396, 1972.

[46] T. Angel, “Formation of Martensite in Austenitic Stainless Steels, effect of deformation, temperature and composition,” *J. Iron Steel Inst.*, pp. 165–174, 1954.

[47] G. B. Olson and M. Cohen, “A mechanism for the strain-induced nucleation of martensitic transformations,” *J. Less- Common Met.*, vol. 28, pp. 107–118, 1972.

[48] R. G. Stringfellow, D. M. Parks, and G. B. Olson, “A constitutive model for transformation plasticity accompanying strain-induced martensitic transformations in metastable austenitic steels,” *Acta Metall. Mater.*, vol. 40, no. 7, pp. 1703–1716, 1992.

[49] G. B. Olson and M. Cohen, “Kinetics of strain-induced martensitic nucleation,” *Metall. Trans. A*, vol. 6, no. 3, pp. 791–795, 1975.

[50] A. M. Beese and D. Mohr, “Effect of stress triaxiality and Lode angle on the kinetics of strain-induced austenite-to-martensite transformation,” *Acta Mater.*, vol. 59, pp. 2589–2600, 2011.

[51] J. B. Leblond, “Mathematical modelling of transformation plasticity in steels II:

Coupling with strain hardening phenomena," *International Journal of Plasticity*, vol. 5, no. 6. pp. 573–591, 1989.

[52] R. G. Stringfellow and D. M. Parks, "A self-consistent model of isotropic viscoplastic behavior in multiphase materials," *Int. J. Plast.*, vol. 7, pp. 529–547, 1991.

[53] A. M. Beese and D. Mohr, "Anisotropic plasticity model coupled with Lode angle dependent strain-induced transformation kinetics law," *J. Mech. Phys. Solids*, vol. 60, pp. 1922–1940, 2012.

[54] G. W. Greenwood and R. H. John, "The deformation of metals under small stresses during phase transformations," *Proc. R. Soc. Lond. A. Math. Phys. Sci.*, vol. 283, pp. 403–422, 1965.

[55] J. R. Patel and M. Cohen, "Criterion for the action of applied stress in the martensitic transformation," *Acta Metall.*, vol. 1, pp. 531–538, 1953.

[56] M. F. McGuire, *Stainless Steels for Design Engineers*. Materials Park: ASM International, 2008.

[57] T. DebRoy, H. L. Wei, J. S. Zuback, T. Mukherjee, J. W. Elmer, J. O. Milewski, A. M. Beese, A. Wilson-Heid, A. De, and W. Zhang, "Additive manufacturing of metallic components – Process, structure and properties," *Prog. Mater. Sci.*, vol. 92, pp. 112–224, 2018.

[58] B. AlMangour and J. M. Yang, "Understanding the deformation behavior of 17-4 precipitate hardenable stainless steel produced by direct metal laser sintering using micropillar compression and TEM," *Int. J. Adv. Manuf. Technol.*, vol. 90, pp. 119–126, 2017.

[59] I. Tolosa, F. Garciandía, F. Zubiri, F. Zapirain, and A. Esnaola, "Study of mechanical properties of AISI 316 stainless steel processed by 'selective laser melting', following different manufacturing strategies," *Int. J. Adv. Manuf. Technol.*, vol. 51, pp. 639–647, Apr. 2010.

[60] M. L. Griffith, M. T. Ensz, J. D. Puskar, C. V. Robino, J. A. Brooks, J. A. Philliber, E. Smugeresky, J. E. Smugeresky, and W. H. Hofmeister, "Understanding the Microstructure and Properties of Components Fabricated by Laser Engineered Net Shaping (LENS)," in *Materials Research Society Symposium*, 2000, vol. 625, pp. 9–20.

[61] M. Ma, Z. Wang, D. Wang, and X. Zeng, "Control of shape and performance for direct laser fabrication of precision large-scale metal parts with 316L Stainless Steel," *Opt. Laser Technol.*, vol. 45, pp. 209–216, 2013.

[62] "ISO/ASTM 52900: Standard Terminology for Additive Manufacturing – General Principles – Part 1: Terminology," in *ASTM International*, West Conshohocken, PA, 2015, pp. 1–9.

[63] X. Wu, "A review of laser fabrication of metallic engineering components and of materials," *Mater. Sci. Technol.*, vol. 23, no. 6, pp. 631–640, 2007.

[64] D. Bourell, J. P. Kruth, M. Leu, G. Levy, D. Rosen, A. M. Beese, and A. Clare, "Materials for additive manufacturing," *CIRP Ann. - Manuf. Technol.*, vol. 66, pp. 659–681, 2017.

[65] J. W. Elmer, S. M. Allen, and T. W. Eagar, "Microstructural Development during Solidification of Stainless Steel Alloys," *Metall. Trans. A*, vol. 20A, no. 2117–2131, 1989.

[66] J. Talonen, “Effect of strain-induced α’-martensite transformation on mechanical properties of metastable austenitic stainless steels,” Helsinki University of Technology, 2007.

[67] L. Facchini, N. Vicente, I. Lonardelli, E. Magalini, P. Robotti, and M. Alberto, “Metastable austenite in 17-4 precipitation-hardening stainless steel produced by selective laser melting,” *Adv. Eng. Mater.*, vol. 12, no. 3, pp. 184–188, 2010.

[68] K. Otsuka and C. M. Wayman, “Mechanism of shape memory effect and superelasticity,” in *Shape memory materials*, 1st editio., K. Otsuka and C. M. Wayman, Eds. 1999, pp. 36–44.

[69] G. W. Powell, E. R. Marshall, and W. A. Backofen, “Strain Hardening of Austenitic Stainless Steel,” *Trans. ASM*, vol. 50, no. 1, pp. 478–497, 1958.

[70] T. Iwamoto, T. Tsuta, and Y. Tomita, “Investigation on deformation mode dependence of strain-induced martensitic transformation in trip steels and modelling of transformation kinetics,” *Int. J. Mech. Sci.*, vol. 40, pp. 173–182, 1998.

[71] C. P. Livitsanos and P. F. Thomson, “The effect of temperature and deformation rate on transformation-dependent ductility of a metastable austenitic stainless steel,” *Mater. Sci. Eng.*, vol. 30, pp. 93–98, 1977.

[72] S. S. Hecker, M. G. Stout, K. P. Staudhammer, and J. L. Smith, “Effects of Strain State and Strain Rate on Deformation- Induced Transformation in 304 Stainless Steel Part I . Magnetic Measurements and Mechanical Behavior,” *Metall. Trans.*, vol. 13A, pp. 619–626, 1982.

[73] L. E. Murr, K. P. Staudhammer, and S. S. Hecker, “Effects of Strain State and Strain Rate on Deformation-Induced Transformation in 304 Stainless Steel: Part I1.

Microstructural Study," *Metall. Trans. A*, vol. 13A, pp. 627–635, 1982.

[74] J. Talonen, P. Nenonen, G. Pape, and H. Hänninen, "Effect of Strain Rate on the Strain-Induced Austenite-Martensite Transformation and Mechanical Properties of Austenitic Stainless Steels," *Metall. Mater. Trans. A*, vol. 36, no. February, pp. 421–432, 2005.

[75] K. P. Staudhammer, C. E. Frantz, S. S. Hecker, and L. E. Murr, "Effects of strain rate on deformation-induced martensite in 304 stainless steel," in *Shock Waves and high-strain-rate phenomena in metals*, M. A. Meyers and L. E. Murr, Eds. Boston, MA: Springer, 1981, pp. 91–112.

[76] W.-S. Lee and C.-F. Lin, "Comparative study of the impact response and microstructure of 304L stainless steel with and without prestrain," *Metall. Mater. Transations A*, vol. 33, no. 9, pp. 2801–2810, 2002.

[77] W.-S. Lee and C.-F. Lin, "Impact properties and microstructure evolution of 304L stainless steel," *Mater. Sci. Eng. A*, vol. 308, no. 1–2, pp. 124–135, 2001.

[78] H. L. Wei, J. Mazumder, and T. DebRoy, "Evolution of solidification texture during additive manufacturing," *Sci. Rep.*, vol. 5, pp. 1–7, 2015.

[79] A. Creuziger and T. Foecke, "Transformation potential predictions for the stress-induced austenite to martensite transformation in steel," *Acta Mater.*, vol. 58, pp. 85–91, 2010.

[80] P. Hilkhuijsen, H. J. M. Geijselaers, T. C. Bor, E. S. Perdahcioğlu, A. H. vd Boogaard, and R. Akkerman, "Strain direction dependency of martensitic transformation in austenitic stainless steels: The effect of γ-texture," *Mater. Sci. Eng. A*, vol. 573, pp. 100–105, 2013.

[81] P. Hilkhuijsen, H. J. M. Geijselaers, and T. C. Bor, “The influence of austenite texture on the martensitic transformation of an austenitic stainless steel,” *J. Alloys Compd.*, vol. 577, pp. 609–613, 2013.

[82] D. De Knijf, T. Nguyen-Minh, R. H. Petrov, L. A. I. Kestens, and J. J. Jonas, “Orientation dependence of the martensite transformation in a quenched and partitioned steel subjected to uniaxial tension,” *J. Appl. Crystallogr.*, vol. 47, pp. 1261–1266, 2014.

[83] K. Nohara, Y. Ono, and N. Ohashi, “Composition and Grain Size Dependencies of Strain-induced Martensitic Transformation in Metastable Austenitic Stainless Steels,” *J. Iron Steel Inst. Japan*, vol. 63, no. 5, pp. 212–222, 1977.

[84] S. K. Varma, J. Kalyanam, L. Murr, and V. Srinivas, “Effect of Grain Size on Deformation-Induced Martensite Formation in 304 and 316 Stainless Steels During Room Temperature Tensile Testing,” *J. Mater. Sci. Lett.*, vol. 13, no. 2, pp. 107–111, 1994.

[85] J. L. Gonzales, R. Aranda, and M. Jonapa, “The influence of grain size on the kinetics of strain induced martensite in type 304 stainless steel,” in *Applications of Stainless Steel ’92*, H. Nordberg and J. Bjorklund, Eds. Stockholm, Sweden, 1992, pp. 1009–1016.

[86] “ASTM E112-13: Standard Test Methods for Determining Average Grain Size,” in *ASTM Standard*, West Conshohocken, PA, 2013.

[87] V. Shrinivas, S. K. Varma, and L. E. Murr, “Deformation-induced martensitic characteristics in 304 and 316 stainless steels during room-temperature rolling,” *Metall. Mater. Trans. A*, vol. 26, no. 3, pp. 661–671, 1995.

[88] ASTM, “ASTM A479/A479M: Standard Specification for Stainless Steel Bars and Shapes for Use in Boilers and Other Pressure Vessels,” in *ASTM International*, West Conshohocken, PA, 2018.

[89] “ASTM E1019: Standard Test Methods for Determination of Carbon , Sulfur , Nitrogen , and Oxygen in Steel and in Iron , Nickel , and Cobalt Alloys by Various Combusition and Fusion Techniques,” in *ASTM International*, West Conshohocken, PA, 2015, pp. 1–28.

[90] “ASTM E1086: Standard Test Method for Analysis of austenitic Stainless Steel by Spark Atomic Emission Spectrometry,” in *ASTM International*, West Conshohocken, PA, 2015, pp. 1–5.

[91] ASTM, “ASTM Standard E8/E8M-16a: Standard Test Methods for Tension Test of Metallic Materials,” in *ASTM International*, West Conshohocken, PA, 2016.

[92] M. S. F. de Lima and S. Sankaré, “Microstructure and mechanical behavior of laser additive manufactured AISI 316 stainless steel stringers,” *Mater. Des.*, vol. 55, pp. 526–532, 2014.

[93] G. Ziółkowski, E. Chlebus, P. Szymczyk, and J. Kurzac, “Application of X-ray CT method for discontinuity and porosity detection in 316L stainless steel parts produced with SLM technology,” *Arch. Civ. Mech. Eng.*, pp. 1–7, 2014.

[94] J. A. Slotwinski, E. J. Garboczi, and K. M. Hebenstreit, “Porosity Measurements and Analysis for Metal Additive Manufacturing Process Control,” *J. Res. Natl. Inst. Stand. Technol.*, vol. 119, p. 494, 2014.

[95] W. Staib and D. I. H. Kunzel, “In-situ Ferrite Content Measurement of Duplex Steel Structures in the Chemical Industry. Practical Applications of the Alternating Field,

Magnetoinductive Method," *Nondestruct. Charact. Mater.*, pp. 614–621, 1989.

[96] A. M. Beese and D. Mohr, "Identification of the Direction-Dependency of the Martensitic Transformation in Stainless Steel Using In Situ Magnetic Permeability Measurements," *Exp. Mech.*, vol. 51, pp. 667–676, 2011.

[97] M. Shimotomai, K. Maruta, K. Mine, and M. Matsui, "Formation of aligned two-phase microstructures by applying a magnetic field during the austenite to ferrite transformation in steels," *Acta Mater.*, vol. 51, no. 10, pp. 2921–2932, 2003.

[98] J. Talonen, P. Aspegren, and H. Hänninen, "Comparison of different methods for measuring strain induced α-martensite content in austenitic steels," *Mater. Sci. Technol.*, vol. 20, no. 12, pp. 1506–1512, 2004.

[99] S. S. M. Tavares, D. Gunderov, V. Stolyarov, and J. M. Neto, "Phase transformation induced by severe plastic deformation in the AISI 304L stainless steel," *Mater. Sci. Eng. A*, vol. 358, no. 1–2, pp. 32–36, 2003.

[100] R. D. K. Misra, B. R. Kumar, M. Somani, and P. Karjalainen, "Deformation processes during tensile straining of ultrafine/nanograined structures formed by reversion in metastable austenitic steels," *Scr. Mater.*, vol. 59, no. 1, pp. 79–82, 2008.

[101] P. Reu, "Virtual Strain Gage Size Study," *Exp. Tech.*, vol. 39, pp. 1–3, 2015.

[102] J. R. Davis, *ASM Specialty Handbook-Stainless Steels*. 1994.

[103] W. J. Sames, K. A. Unocic, R. R. Dehoff, T. Lolla, and S. S. Babu, "Thermal effects on microstructural heterogeneity of Inconel 718 materials fabricated by electron beam melting," *J. Mater. Res.*, vol. 29, no. 17, pp. 1920–1930, 2014.

[104] R. Rai, J. W. Elmer, T. a Palmer, and T. DebRoy, "Heat transfer and fluid flow during keyhole mode laser welding of tantalum, Ti–6Al–4V, 304L stainless steel

and vanadium," *J. Phys. D. Appl. Phys.*, vol. 40, pp. 5753–5766, 2007.

[105] M. F. Ashby and K. E. Easterling, "The transformation hardening of steel surfaces by laser beams—I. Hypo-eutectoid steels," *Acta Metall.*, vol. 32, no. Il, pp. 1935–1948, 1984.

[106] L. W.B., K. E. Easterling, and M. F. Ashby, "Laser Transformation Hardening of Steel - II. Hypereutectoid Steels," *Acta Metall.*, vol. 34, no. 8, pp. 1533–1543, 1986.

[107] J. C. Ion, H. R. Shercliff, and M. F. Ashby, "Diagrams for laser materials processing," *Acta Metall.*, vol. 40, no. 7, pp. 1539–1551, 1992.

[108] M. F. Ashby and K. E. Easterling, "A first report on diagrams for grain growth in welds," *Acta Metall.*, vol. 30, pp. 1969–1978, 1982.

[109] J. C. Ion, K. E. Easterling, and M. F. Ashby, "A second report on diagrams of microstructure and hardness for heat-affected zones in welds," *Acta Metall.*, vol. 32, no. 11, pp. 1949–1962, 1984.

[110] V. Manvatkar, A. De, and T. Debroy, "Heat transfer and material flow during laser assisted multi-layer additive manufacturing," *J. Appl. Phys.*, vol. 116, no. 12, 2014.

[111] S. A. David, T. DebRoy, J. C. Lippold, H. B. Smartt, and J. M. Vitek, Eds., "Trends in Welding Research: Proceedings of the 7th International Conference," 2005, p. 996.

[112] E. R. Denlinger, J. C. Heigel, P. Michaleris, and T. A. Palmer, "Effect of Inter-Layer Dwell Time on Distortion and Residual Stress in Additive Manufacturing of Titanium and Nickel Alloys," *J. Mater. Process. Technol.*, vol. 215, pp. 123–131, 2015.

[113] V. Manvatkar, A. De, and T. DebRoy, "Spatial variation of melt pool geometry,

peak temperature and solidification parameters during laser assisted additive manufacturing process," *Mater. Sci. Technol.*, vol. 31, no. 8, pp. 924–930, 2015.

[114] E. O. Hall, "The Deformation and Ageing of Mild Steel: III Discussion of Results," *Proc. Phys. Soc. Sect. B*, vol. 64, pp. 747–753, 1951.

[115] N. J. Petch, "The cleavage strength of polycrystals," *J. Iron Steel Inst.*, vol. 173, pp. 25–27, 1953.

[116] K. K. Singh, S. Sangal, and G. S. Murty, "Hall–Petch behaviour of 316L austenitic stainless steel at room temperature," *Mater. Sci. Technol.*, vol. 18, pp. 165–172, 2002.

[117] H. Khalid Rafi, N. V Karthik, T. L. Starr, and B. E. Stucker, "Mechanical property evaluation of Ti-6Al-4V parts made using Electron Beam Melting," *Solid Free. Fabr. Proc.*, pp. 526–535, 2012.

[118] J. B. Leblond, G. Mottet, and J. C. Devaux, "A theoretical and numerical approach to the plastic behaviour of steels during phase transformations—I. Derivation of general relations," *J. Mech. Phys. Solids*, vol. 34, no. 4, pp. 395–409, 1986.

[119] *ISO 8249:2000 (en): Welding — Determination of Ferrite Number (FN) in austenitic and duplex ferritic-austenitic Cr-Ni stainless steel weld metals*. 2000.

[120] P. K. Palani and N. Murugan, "Prediction of Delta Ferrite Content and Effect of Welding Process Parameters in Claddings by FCAW," *Mater. Manuf. Process.*, vol. 21, no. 5, pp. 431–438, 2006.

[121] Fischer, "Operator's Manual for Feritescope FMP30 Manual," 2008.

[122] J. Talonen and H. Hänninen, "Formation of shear bands and strain-induced martensite during plastic deformation of metastable austenitic stainless steels," *Acta*

Mater., vol. 55, pp. 6108–6118, 2007.

[123] K. Tomimura, S. Takaki, S. Tanimoto, and Y. Tokunaga, "Optimal Refining Chemical Composition in Fe-Cr-Ni Alloys for Ultra Grain by Reversion from Deformation Induced Martensite," *ISIJ Int.*, vol. 31, pp. 721–727, 1991.

[124] Z. Wang and A. M. Beese, "Effect of chemistry on martensitic phase transformation kinetics and resulting properties of additively manufactured stainless steel," *Acta Mater.*, vol. 131, pp. 410–422, 2017.

[125] T. Mukherjee, J. S. Zuback, A. De, and T. DebRoy, "Printability of alloys for additive manufacturing," *Sci. Rep.*, vol. 6, pp. 1–8, 2016.

[126] H. K. Rafi, D. Pal, N. Patil, T. L. Starr, and B. E. Stucker, "Microstructure and Mechanical Behavior of 17-4 Precipitation Hardenable Steel Processed by Selective Laser Melting," *J. Mater. Eng. Perform.*, vol. 23, no. 12, pp. 4421–4428, 2014.

[127] X. He, T. DebRoy, and P. W. Fuerschbach, "Composition change of stainless steel during microjoining with short laser pulse," *J. Appl. Phys.*, vol. 96, pp. 4547–4555, 2004.

[128] A. Bienkowski, "The magneto-elastic villari effect in ferrites," *J. Magn. Magn. Mater.*, vol. 19, pp. 120–122, 1980.

[129] K. An, H. D. Skorpenske, A. D. Stoica, D. Ma, X. L. Wang, and E. Cakmak, "First in situ lattice strains measurements under load at VULCAN," *Metall. Mater. Trans. A Phys. Metall. Mater. Sci.*, vol. 42, no. 1, pp. 95–99, 2011.

[130] T. Ungar, A. D. Stoica, G. Tichy, and X.-L. Wang, "Orientation-dependent evolution of the dislocation density in grain populations with different crystallographic orientations relative to the tensile axis in a polycrystalline aggregate

of stainless steel," *Acta Mater.*, vol. 66, pp. 251–261, 2014.

[131] G. M. Stoica, A. D. Stoica, M. K. Miller, and D. Ma, "Temperature-dependent elastic anisotropy and mesoscale deformation in a nanostructured ferritic alloy.," *Nat. Commun.*, vol. 5, pp. 1–8, 2014.

[132] K. An, "VDRIVE-Data Reduction and Interactive Visulaization Softwarew for Event Mode Neutron Diffraction," ORNL Report, Oak Ridge National Laboratory, ORNL-TM-2012-621, 2012.

[133] R. L. Snyder, "The Use of Reference Intensity Ratios in X-Ray Quantitative Analysis," *Powder Diffr.*, vol. 7, no. 4, pp. 186–193, 1992.

[134] ABAQUS, *Version 6.14 User's Manual*. 2014.

[135] D. Chung, "Materials for thermal conduction," *Appl. Therm. Eng.*, vol. 21, pp. 1593–1605, 2001.

[136] "Man-systems Integration Standards," *National Aeronautics and Space Administration*, 1995. [Online]. Available: https://msis.jsc.nasa.gov/sections/section04.htm. [Accessed: 01-Jan-2017].

[137] H. Yüncü, "Thermal contact conductance of nominaly flat surfaces," *Heat Mass Transf.*, vol. 43, pp. 1–5, 2006.

[138] S. Murugan, S. K. Rai, P. V. Kumar, T. Jayakumar, B. Raj, and M. S. C. Bose, "Temperature distribution and residual stresses due to multipass welding in type 304 stainless steel and low carbon steel weld pads," *Int. J. Press. Vessel. Pip.*, vol. 78, no. 4, pp. 307–317, 2001.

[139] K. Spencer, J. D. Embury, K. T. Conlon, M. Véron, and Y. Bréchet, "Strengthening via the formation of strain-induced martensite in stainless steels," *Mater. Sci. Eng.*

A, vol. 387–389, pp. 873–881, 2004.

[140] M. Moallemi, A. Kermanpur, A. Najafizadeh, A. Rezaee, H. S. Baghbadorani, and P. D. Nezhadfar, "Deformation-induced martensitic transformation in a 201 austenitic steel: The synergy of stacking fault energy and chemical driving force," *Mater. Sci. Eng. A*, vol. 653, pp. 147–152, 2016.

[141] S. Curtze and V. T. Kuokkala, "Dependence of tensile deformation behavior of TWIP steels on stacking fault energy, temperature and strain rate," *Acta Mater.*, vol. 58, pp. 5129–5141, 2010.

[142] G. B. Olson and M. Cohen, "A General Mechanism of Martensitic Nucleation: Part I. General Concepts and the FCC - HCP Transformation," *Metall. Trans. A*, vol. 7A, pp. 1897–1904, 1976.

[143] S. Curtze, V. T. Kuokkala, A. Oikari, J. Talonen, and H. Hänninen, "Thermodynamic modeling of the stacking fault energy of austenitic steels," *Acta Mater.*, vol. 59, pp. 1068–1076, 2011.

[144] I. A. Yakubtsov, A. Ariapour, and D. D. Perovic, "Effect of nitrogen on stacking fault energy of f.c.c. iron-based alloys," *Acta Mater.*, vol. 47, no. 4, pp. 1271–1279, 1999.

[145] P. J. Ferreira and P. Müllner, "A thermodynamic model for the stacking-fault energy," *Acta Mater.*, vol. 46, no. 13, pp. 4479–4484, 1998.

[146] M. Olsson, "Thermodynamic Modeling of the Stacking Fault Energy in Austenitic Stainless Steels," KTH Royal Institute of Technology, 2014.

[147] A. H. Cottrell, "Tensile Properties of Unstable Austenite and Its Low-Teperature Decomposition Products," *J. Iron Steel Inst.*, vol. 151, no. 1, pp. 93–104, 1945.

[148] P. O. Santacreu, J. C. Glez, G. Chinouilh, and T. Frohlich, “Behaviour model of austenitic stainless steels for automotive structural parts,” *Steel Res. Int.*, vol. 77, pp. 686–691, 2006.

[149] Z. Wang and A. M. Beese, “Effect of stress state and texture on martensitic phase transformation kinetics of additively manufactured austenitic stainless steel,” *Submitted for publication.*

[150] B. Cina, “Effect of cold work on the γ → α transformation in some Fe-Ni-Cr alloys,” *J. Iron Steel Inst.*, vol. 177, no. 4, p. 406, 1954.

[151] V. V. Kosarchuk, L. V. Zaitseva, A. A. Lebedev, and B. I. Koval’chuk, “Effect of stressed state parameters on phase transformation kinetics in austenitic steels with plastic deformation,” *Strength of Matlerials*, vol. 21, pp. 60–64, 1989.

[152] T. Okutani, N. Yukawa, K. Ishikawa, and T. Jinma, “The strain-induced martensitic transformation of SU304 under various stress states,” *Proc. Japanese Soc. Tech. Plast. ’95 Spring*, pp. 331–332, 1995.

[153] H. Y. Yu, Y. K. Gao, and D. J. Meng, “Transformation behavior of retained austenite under different deformation modes for low alloyed TRIP-assisted steels,” *Mater. Sci. Eng. A*, vol. 441, pp. 331–335, 2006.

[154] C.-C. Young, “Transformation toughening of phosphocarbide-strengthened austenitic steels,” Massachusetts Institute of Technology, 1988.

[155] A. A. Lebedev and V. V. Kosarchuk, “Influence of phase transformations on the mechanical properties of austenitic stainless steels,” *Int. J. Plast.*, vol. 16, pp. 749–767, 2000.

[156] Y. Tomita and T. Iwamoto, “Constitutive modeling of trip steel and its application

to the improvement of mechanical properties," *Int. J. Mech. Sci.*, vol. 37, no. 12, pp. 1295–1305, 1995.

[157] D. Mohr and M. Oswald, "A new experimental technique for the multi-axial testing of advanced high strength steel sheets," *Exp. Mech.*, vol. 48, pp. 65–77, 2008.

[158] H. M. Rietveld, "A profile refinement method for nuclear and magnetic structures," *J. Appl. Crystallogr.*, vol. 2, pp. 65–71, 1969.

[159] A. C. Larson and R. B. Von Dreele, "General Structure Analysis System (GSAS)," 2004.

[160] K. Mumtaz, S. Takahashi, J. Echigoya, Y. Kamada, L. F. Zhang, H. Kikuchi, K. Ara, and M. Sato, "Magnetic measurements of martensitic transformation in austenitic stainless steel after room temperature rolling," *J. Mater. Sci.*, vol. 39, pp. 85–97, 2004.

[161] "ASTM Standard E975-13: Standard Practice for X-Ray Determination of Retained Austenite in Steel with Near Random Crystallographic Orientation," in *ASTM International*, 2013, pp. 1–7.

[162] M. S. Wechsler, D. S. Lieberman, and T. A. Read, "On the Theory of the Formation of Martensite," *Trans. AIME*, pp. 1503–1515, 1953.

[163] H. Hallberg, P. Håkansson, and M. Ristinmaa, "A constitutive model for the formation of martensite in austenitic steels under large strain plasticity," *Int. J. Plast.*, vol. 23, pp. 1213–1239, 2007.

[164] J. Post, K. Datta, and J. Beyer, "A macroscopic constitutive model for a metastable austenitic stainless steel," *Mater. Sci. Eng. A*, vol. 485, pp. 290–298, 2008.

[165] A. Bhattacharyya and G. J. Weng, "An energy criterion for the stress-induced

martensitic transformation in a ductile system," *J. Mech. Phys. Solids*, vol. 42, no. 11, pp. 1699–1724, 1994.

[166] A. H. C. Hänsel, P. Hora, and J. Reissner, "Model for the kinetics of strain-induced martensitic phase transformation at non-isothermal conditions for the simulation of sheet metal forming processes with metastable austenitic steels," in *Simulation of Materials Processing: Theory, Methods, and Applications*, J. Huétink and F. P. T. Baaijens, Eds. Balkema, Rotterdam, 1998, pp. 373–378.

[167] D. Mohr and J. Jacquemin, "Large deformation of anisotropic austenitic stainless steel sheets at room temperature: Multi-axial experiments and phenomenological modeling," *J. Mech. Phys. Solids*, vol. 56, no. 10, pp. 2935–2956, 2008.

[168] C. P. Kohar, M. Cherkaoui, H. El Kadiri, and K. Inal, "Numerical modeling of TRIP steel in axial crashworthiness," *Int. J. Plast.*, vol. 84, pp. 224–254, 2016.

[169] S. Hazar, B. Alfredsson, and J. Lai, "Mechanical modeling of coupled plasticity and phase transformation effects in a martensitic high strength bearing steel," *Mech. Mater.*, vol. 117, pp. 41–57, 2018.

[170] H. Y. Yu and S. J. Chen, "A mixed hardening model combined with the transformation-induced plasticity effect," *J. Manuf. Process.*, vol. 28, pp. 390–398, 2017.

[171] M. P. Miller and D. L. McDowell, "Modeling large strain multiaxial effects in FCC polycrystals," *Int. J. Plast.*, vol. 12, no. 7, pp. 875–902, 1996.

[172] J. Y. Lee, F. Barlat, and M. G. Lee, "Constitutive and friction modeling for accurate springback analysis of advanced high strength steel sheets," *Int. J. Plast.*, vol. 71, pp. 113–135, 2015.

[173] M. I. Latypov, S. Shin, B. C. De Cooman, and H. S. Kim, “Micromechanical finite element analysis of strain partitioning in multiphase medium manganese TWIP+TRIP steel,” *Acta Mater.*, vol. 108, pp. 219–228, 2016.

[174] S. Msolli, M. Martiny, M. C. Cardoso, L. P. Moreira, S. Mercier, and A. Molinari, “Numerical modeling of the deformation of AISI 304L using a tangent additive Mori-Tanaka homogenization scheme: Application to sheet metal forming,” *J. Mater. Process. Technol.*, vol. 235, pp. 187–205, 2016.

[175] R. Zaera, J. A. Rodríguez-Martínez, A. Casado, J. Fernández-Sáez, A. Rusinek, and R. Pesci, “A constitutive model for analyzing martensite formation in austenitic steels deforming at high strain rates,” *Int. J. Plast.*, vol. 29, pp. 77–101, 2012.

[176] Z. Wang and A. M. Beese, “Plasticity model coupled with strain-induced martensitic transformation kinetics for austenitic stainless steel deposited by additive manufacturing,” *Submitted for publication.*

[177] R. Hill, “A theory of the yielding and plastic flow of anisotropic metals,” *Proc. R. Soc. Lond. A. Math. Phys. Sci.*, vol. 193, no. 1033, pp. 281–297, 1948.

[178] H. W. Swift, “Plastic instability under plane stress,” *J. Mech. Phys. Solids*, vol. 1, pp. 1–18, 1952.

VITA

Zhuqing Wang was born in Daqing, China, in 1990. She graduated with a B.S. degree in Materials Science and Engineering from University of Science and Technology Beijing in June 2012. She graduated with a M.S. degree in Materials Science and Engineering from University of Pennsylvania in May 2014. She continued her Ph.D. study in Materials Science and Engineering at Pennsylvania State University from August 2014. Her research interests including metallurgy, mechanics, and additive manufacturing process.